BremHLR

Kompetenzzentrum für Höchstleistungsrechnen Bremen

Statusbericht 2018

des

Kompetenzzentrums

für

Höchstleistungsrechnen Bremen

–BremHLR–

Bremen, Juli 2019

Universität Bremen

JACOBS UNIVERSITY

ALFRED-WEGENER-INSTITUT HELMHOLTZ-ZENTRUM FÜR POLAR- UND MEERESFORSCHUNG

Hochschule Bremerhaven

HLRN

Norddeutscher Verbund für Hoch- und Höchstleistungsrechnen

www.bremhlr.uni-bremen.de

Das Berichtsjahr 2018 in Stichpunkten

- Stabile Bremer Nutzung der Ressourcen des Norddeutschen Verbunds für Hoch- und Höchstleistungsrechnen (HLRN)
- Erfolgreicher 13. BremHLR Workshop zur Einführung in die parallele Programmierung
- Ende des HLRN-III Betriebs an der Leibnitz-Universität Hannover
- Inbetriebnahme der ersten Ausbaustufe des neuen Rechnersystems HLRN-IV

Inhaltsverzeichnis

1 BremHLR: Aufgaben und organisatorische Struktur

1.1 Aufgaben

Das Land Bremen beteiligt sich am Norddeutschen Verbund für Hoch- und Höchstleistungsrechnen – HLRN – um an dem rasanten Fortschritt der Computer- und Softwaretechnologie Teil zu haben. Das Kompetenzzentrum für Höchstleistungsrechnen Bremen – BremHLR – unterstützt dazu Wissenschaftler im wissenschaftlichen Rechnen insbesondere im Land Bremen. Die Fachberater des BremHLR leisten Unterstützung für Projekte sowohl in der Konzeption, der Antragstellung als auch der Durchführung. Der Schwerpunkt der Unterstützung liegt hierbei auf Projekten auf dem HLRN-System. Seit 2005 wurde die Betreuung aber auch auf Rechenprojekte an den nationalen Höchstleistungsrechenzentren wie z. B. dem Jülich Supercomputing Centre (JSC) ausgeweitet.

Als Bestandteil im Kompetenznetzwerk des HLRN beteiligt sich BremHLR unter anderem an der fachspezifischen Nutzerberatung, der Pflege von Software-Paketen und der Veranstaltung überregionaler Nutzerworkshops. Die Geschäftsstelle des BremHLR ist an der Universität Bremen im Zentrum für Technomathematik angesiedelt.

Das BremHLR wurde am 1. Juli 2003 als Kooperation zwischen der Universität Bremen (UB), der Jacobs University Bremen (JUB) und dem Alfred-Wegener-Institut Helmholtz-Zentrum für Polar- und Meeresforschung (AWI) gegründet. Seit April 2008 ist auch die Hochschule Bremerhaven (HBHV) Kooperationspartner des BremHLR. Das Kompetenzzentrum wird von den beteiligten Kooperationspartnern sowie der Bremer Senatorin für Wissenschaft, Gesundheit und Verbraucherschutz (SfWGV) anteilig finanziell getragen. Seit Januar 2014 ist die JUB als ideelles Mitglied beitragsfrei gestellt.

1.2 Struktur

Dem Lenkungsausschuss des BremHLR als oberstes beschlussfassendes und steuerndes Gremium gehören in der Berichtsperiode folgende Vertreter der kooperierenden Einrichtungen an. Im Einzelnen sind dies:

- Prof. Dr. Alfred Schmidt (UB/Zentrum für Technomathematik ZeTeM)
- Prof. Dr.Stephan Frickenhaus(AWI/Rechenzentrum, UB/FB3)
- Prof. Dr. Ulrich Kleinekathöfer (JUB)
- Prof. Dr. Henrik Lipskoch (HBHV)
- Dr. Jörg Hofmann (SfWGV)

Die fachspezifische Betreuung der Projekte am Norddeutschen Verbund für Hoch- und Höchstleistungsrechnen (HLRN) sowie von Projekten an anderen nationalen Höchstleistungsrechenzentren wird von den Fachberatern des BremHLR geleistet, die ebenfalls den Einrichtungen der Kooperationspartner angehören. Im Berichtszeitraum waren folgende Fachberater tätig:

- Dr. Lars Nerger (AWI/Rechenzentrum, UB/ZeTeM, Leiter Geschäftsstelle)
- Thorsten Coordes (UB/ZARM)
- Dr. Achim Geleßus (JUB/CLAMV)
- Dr. Natalja Rakowsky (AWI/Rechenzentrum)

Die Geschäftsstelle ist verantwortlich für die Organisation der Workshops (siehe Abschnitt Veranstaltungen) und die Unterstützung der Nutzer, insbesondere im Antragsverfahren. Das Sekretariat der Geschäftsstelle wird betreut von

- Julitta von Deetzen.

2 Tätigkeitsprofil des BremHLR im Berichtszeitraum

2.1 Unterstützung der HLRN-Nutzung im Land Bremen

Ein Schwerpunkt der Aktivitäten des BremHLR lag auch in diesem Berichtszeitraum in der Unterstützung der HLRN-Nutzung. Neben den Tätigkeiten von Prof. Dr. Wolfgang Hiller als Mitglied der Technischen Kommission sowie Prof. Dr. Alfred Schmidt als Mitglied des Wissenschaftlichen Ausschusses bestand die Unterstützung des HLRN durch das BremHLR hauptsächlich in der Fachberatung für Bremer Projekte am HLRN von der Antragstellung bis zur Begleitung rechenintensiver Projekte während der gesamten Projektlaufzeit.

Eine wesentliche Aufgabe im Berichtsjahr war die weitere Unterstützung der Bremer Nutzer des HLRN bei der effizienten Nutzung des HLRN-III Hochleistungsrechnersystems. Des Weiteren haben die Fachberater des BremHLR Nutzer bei der Portierung ihrer Modelle auf das neue Rechnersystem HLRN-IV unterstützt. Ab dem 19.9.2018 konnten zunächst Fachberater das System testen und Software installieren. Ab dem 29.10. haben dann erfahrere „Powernutzer“ Zugang auf das System erhalten um Anwendungen zu portieren und das System zu testen. Am 11.12. wurde das System dann für alle Nutzer geöffnet. Die Portierungsunterstützung wird auch im Jahr 2019 weiter ein wichtiges Aufgabengebiet sein.

2.2 Weitere Aktivitäten des BremHLR

Im Veranstaltungsjahr 2018 wurde vom BremHLR der *13. Workshop zur Einführung in die parallele Programmierung mit MPI und OpenMP* organisiert und durchgeführt. Mit 39 Teilnehmern war dieser Workshop wieder sehr gut besucht.

Der Workshop wurde in der Zeit vom 22. bis zum 26. Januar 2018 an der JUB abgehalten. Als Referent konnte wie bereits bei bisherigen Workshops Dr. Hinnerk Stüben vom Regionalen Rechenzentrum der Universität Hamburg gewonnen werden, der den Workshop gemeinsam mit dem BremHLR-Fachberater Dr. Lars Nerger leitete. Für die Studenten der JUB wurde der Workshop auch wieder als offizielle Lehrveranstaltung angeboten. Durch die Bearbeitung eines abschließend bewerteten Programmierprojekts konnten die Studenten Kreditpunkte für ihr Bachelor- und Masterstudium erlangen.

Der sehr gute Zuspruch und der große Erfolg der Veranstaltungen zeigt deutlich den dringenden Bedarf zur Ausbildung im Hoch- und Höchstleistungsrechnen und gibt Anlass dazu solche Workshops auch weiterhin als regelmäßige Ausbildungs- und Schulungsmaßnahme anzubieten.

Neben dem Workshop zur Einführung in die parallele Programmierung beteiligten sich Fachberater des BremHLR an Fachberaterworkshops des HLRN-Kompetenznetzwerks in Göttingen und Hamburg. Bei diesen Workshops wurden unterschiedliche Themen des HLRN-Betriebs und der Nutzerbetreuung besprochen. Eine Übersicht über die Veranstaltungen ist in Abschnitt 4 zu finden.

3 Statistische Angaben zu den Bremer Höchstleistungsprojekten

Auch im Jahr 2018 wurde der HLRN intensiv durch Bremer Projekte genutzt. Im Jahresdurchschnitt wurde auf dem HLRN-III System ein prozentualer Anteil von 16,7 % an der gesamten am HLRN-III abgenommenen Rechenleistung erreicht. Dieses liegt deutlich über dem investiven Anteil von etwa 3,5% des Landes Bremen am HLRN. Über die gesamte Laufzeit seit Einrichtung des HLRN-Verbunds wurde durch Bremer Projekte ein Anteil von 8,4% der verfügbaren Rechenzeit abgenommen.

Zum September 2018 ist im Rahmen der Umstellung auf das neue HLRN-IV System das HLRN-III System in Hannover abgeschaltet wurden. Das HLRN-IV System am neuen Standort Göttingen ist am 11. Dezember 2018 für alle Nutzer geöffnet worden.

Insgesamt wurden im Jahr 2018 etwa 6.900.000 NPL[1] durch Bremer Projekte am HLRN-III System abgenommen. Abbildung 3.1 zeigt den monatlichen Verbrauch der Bremer Projekte am HLRN-III System. Ab September 2018 gelten die Verbrauchszahlen nur für den Berliner HLRN-Komplex, der bis zur Installation der zweiten Ausbaustufe des HLRN-IV noch weiter betrieben wird, wobei dieses System besonders stark genutzt wurde.

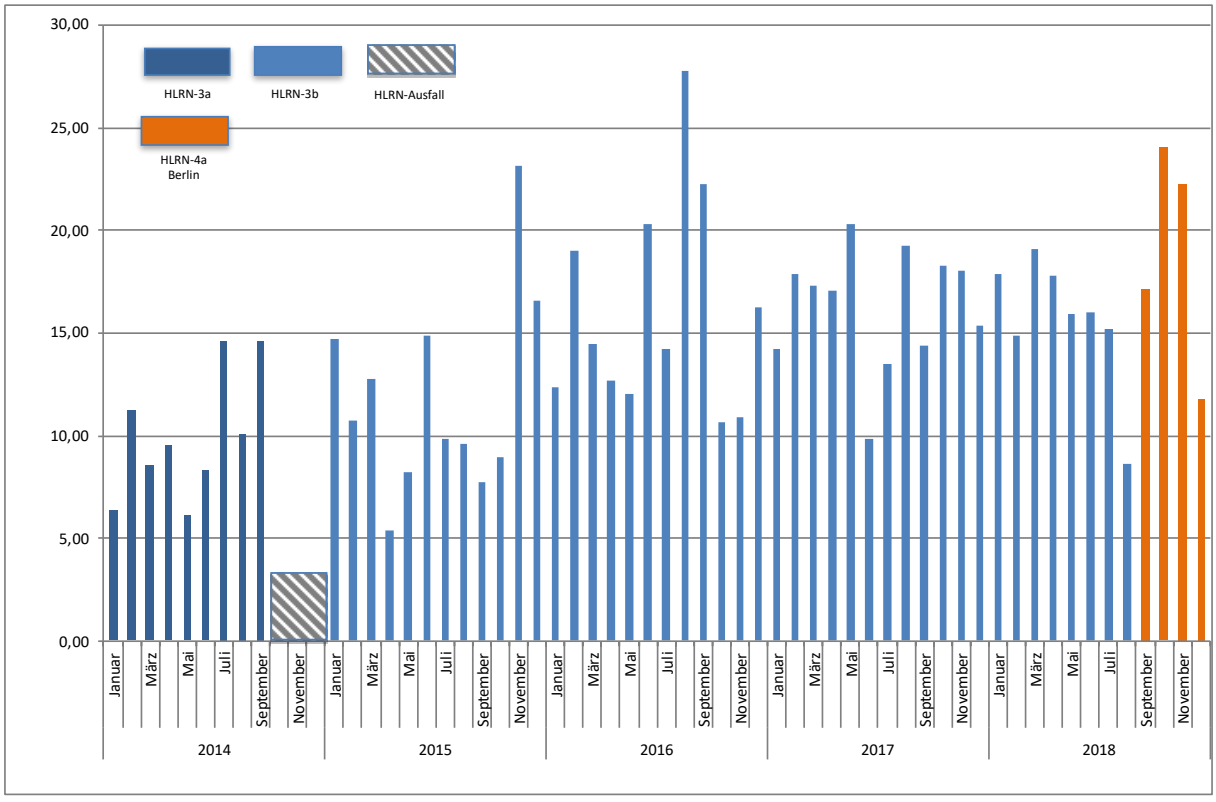

Abbildung 3.1: Monatliche Rechenzeitnutzung der Bremer HLRN-Großprojekte seit Januar 2014 auf dem HLRN-III System in der HLRN-Leistungseinheit NPL. Die Farben zeigen die Verfügbarkeit der unterschiedlichen Ausbaustufen des HLRN-Systems. Von Oktober bis Dezember 2014 waren die HLRN-Systeme nicht bzw. nur teilweise nutzbar. Ab September 2018 wurden die NPL wegen der Umstellung auf HLRN-IV nur in Berlin erfasst.

[1]Norddeutsche Parallelrechner-Leistungseinheit: Auf den Systemen der ersten Ausbaustufe des HLRN-III entspricht 1 NPL einer halben CPU-h auf einem Knoten mit je 24 Prozessorkernen. Auf den Systemen der zweiten Ausbaustufe entspricht die Nutzung eines Knotens über eine Stunde 2,4 NPL.

Eine Übersicht zu allen vom BremHLR betreuten Projekten gibt Tabelle 3.1. Im Jahr 2018 wurden vom BremHLR 37 Projekte am HLRN betreut. Die Projekte werden von über 100 akkreditierten Nutzern durchgeführt. 10 neue Projekte mit teilweise sehr großem Rechenzeitbedarf wurden im Jahr 2017 beantragt und vom Wissenschaftlichen Ausschuss des HLRN bewilligt. 13 Projekte wurden im Berichtsjahr beendet.

4 Veranstaltungen mit Beteiligung des BremHLR

13. BremHLR-Workshop *Einführung in die Programmierung mit MPI und OpenMP*

Veranstalter: BremHLR

Datum: 22. – 26. Januar 2018

Ort: Jacobs University Bremen

Beschreibung: In dem Workshop wurden die Grundlagen der parallelen Programmierung vermittelt. Der Schwerpunkt lag auf den Programmiermodellen MPI und OpenMP. Praktische Übungen bildeten einen wesentlichen Teil des Workshops.

Referenten: Dr. Hinnerk Stüben (Regionales Rechenzentrum der Universität Hamburg) und Dr. Lars Nerger (BremHLR).

Teilnehmerzahl: 39

Teilnehmende Institutionen: AWI, Jacobs University, Leibnitz-Institut für Atmosphärenphysik, MPI Hamburg, Uni Bremen, Uni Hannover, Uni Hamburg

33. HLRN-Fachberater-Workshop

Veranstalter:IT- und Medienzentrum, Uni Rostock

Datum: 25. – 26. April 2018

Ort: Uni Rostock

Teilnehmerzahl: 26

Teilnehmende Institutionen: BremHLR (AWI, ZARM), BTU Cottbus-Senftenberg, HU Berlin, GWDG/Uni Göttingen, IOW, LUIS/Uni Hannover, Uni Hamburg (RRZ, Sternwarte), Uni Kiel, Uni Potsdam, Uni Rostock, ZIB

HLRN-IV/Atos User Workshop – Einführung in das HLRN-IV System

Veranstalter: GWDG/Uni Göttingen

Datum: 8. – 11. Oktober 2018

Ort: Uni Göttingen

Teilnehmerzahl: 30

Teilnehmende Institutionen: Atos, BremHLR (AWI), BTU Cottbus-Senftenberg, GEOMAR, Helmholtz-Zentrum Berlin, IOW, TiHo Hannover, TU Braunschweig, TU Clausthal, Uni Göttingen, Uni Hamburg, Uni Hannover, Uni Potsdam, Uni Kiel

Tabelle 3.1: Übersicht der Bremer HPC-Projekte, die innerhalb des Berichtszeitraums vom BremHLR betreut wurden. Status: F = Fortsetzung, E = Erstantrag; kNPL: Kontingent in tausend NPL im Jahr 2018

Kennung	Projektleiter	Institut	Laufzeit	kNPL	Status
hbc00023	Dr. M. Delle Piane	UB/BCCMS	III/17 – II/18	80	E
hbc00025	Prof. Dr. L. Colombi-Ciacchi	UB/BCCMS	III/17 – III/18	116	E
hbc00027	Prof. Dr. P. Deak	UB/BCCMS	I/18 – I/19	160	E
hbc00028	Dr. M. DellePiane	UB/BCCMS	I/18 – I/19	140	E
hbc00029	Dr. L. Moskaleva	UB/Chemie	I/18 – IV/18	214	E
hbc00030	Dr. M. Fischer	UB/Geo	II/18-I/19	75	E
hbc00031	Prof. Dr. L. Mädler	UB/FB4	III/18 – II/19	80	E
hbi00026	Dr.-Ing. R. Groll	UB/ZARM	II/15 – I/19	128	F
hbi00027	Dr.-Ing. R. Groll	UB/ZARM	IV/15 – IV/18	120	F
hbi00030	Dr.-Ing. R. Groll	UB/ZARM	II/16 – I/18	25	E
hbi00033	Prof.Dr. M. Avila	UB/ZARM	I/17 – I/19	310	F
hbi00035	Prof.Dr. M. Avila	UB/ZARM	I/17 – I/18	66	E
hbi00036	Prof.Dr. U. Fritsching	UB/FB4	II/17 – I/19	110	F
hbi00037	Prof.Dr. U. Fritsching	UB/FB4	II/17 – I/19	132	F
hbk00032	Prof. Dr. T. Jung	AWI & UB	II/12 – II/19	950	F
hbk00034	Prof. Dr. T.Kanzow	AWI & UB	III/13 – III/19	660	F
hbk00038	Prof. Dr. T. Kanzow	AWI & UB	III/14 – II/19	675	F
hbk00044	Prof. Dr. T. Jung	AWI & UB	II/15 – III/18	210	F
hbk00045	Dr. A. Rozanov	UB/IUP	IV/15 – IV/18	183	F
hbk00055	Prof. Dr. A. Bracher	AWI & UB	III/16 – III/19	216	F
hbk00057	Dr. A. Rozanov	UB/IUP	I/17 – II/19	298	F
hbk00058	Prof. Dr. M. Schulz	UB/MARUM	III/17 – II/18	1	E
hbk00059	Prof. Dr. M. Schulz	UB/MARUM	III/17 – III/19	310	F
hbk00060	Prof. Dr. G. Lohmann	AWI & UB	III/17 – IV/18	446	E
hbk00061	Prof Dr. M. Schulz	UB/MARUM	IV/17 – III/19	90	F
hbk00062	Dr. A. Rozanov	UB/IUP	IV/17 – III/19	600	F
hbk00064	Prof. Dr. T. Jung	AWI & UB	I/18 – III/19	350	F
hbk00066	Prof. Dr. G. Lohmann	AWI & UB	I/18 – IV/18	480	E
hbk00067	Prof. Dr. M. Schulz	UB/MARUM	I/18 – I/19	350	E
hbk00069	Prof. Dr. D. Wolf-Gladrow	AWI & UB	II/18 – IV/18	261	E
hbk00070	Prof. Dr. M. Schulz	UB/MARUM	III/18 – II/19	100	E
hbp00035	Prof. Dr. C. Lämmerzahl	UB/ZARM	I/16 – I/18	20	F
hbp00038	Dr. M. Lorke	UB/Physik	II/16 – III/18	89	F
hbp00041	Prof. Dr. C. Lämmerzahl, Prof. Dr. S. Rosswog	UB/ZARM	I/17 – I/19	90	F
hbp00045	Prof. Dr. T. Wehling	UB/Physik	II/17 – I/19	98	F
hbp00046	Prof. Dr. T. Wehling	UB/Physik	IV/17 – III/19	101	F

Gedenken an Helmuth Wolf

* 30.12.1950 + 24.03.2018

Das BremHLR trauert um sein langjähriges Lenkungsausschuss-Mitglied Helmuth Wolf. Es war ihm stets ein wichtiges Anliegen, der Spitzenforschung in Norddeutschland die notwendige Forschungsinfrastruktur, insbesondere Hochleistungsrechentechnik, bereitzustellen. Helmuth Wolf gehörte zu den Gründungsvätern des BremHLR und des HLRN-Verbunds. Er hat beides entscheidend mitgeprägt und für die Anerkennung ihres überregionalen Wirkens gekämpft. Unsere Gedanken sind bei seinen Angehörigen.

Die Mitglieder des BremHLR - Bremer Kompetenzzentrums für Höchstleistungsrechnen.

5 Informationen zur Infrastruktur: Die erste Ausbaustufe des HLRN-IV Systems

Im September 2019 wurde an der Universität Göttingen die erste Ausbaustufe des neuen HLRN-IV Rechnersystems in Betrieb genommen. Der Standort in Göttingen löst den bisherigen Betreiberstandort an der Universität Hannover ab. Dort ist das bisherige HLRN-III System am 31. August abgeschaltet wurden. Während der ersten Ausbaustufe des HLRN-IV wird das bisherige HLRN-III System in Berlin noch weiter betrieben. Der Zugang zum HLRN-IV System wurde zunächst nur für die Fachberater geöffnet, damit diese erste Tests ausführen und notwendige Anwendungssoftware und Programmbibliotheken installieren konnten. Da in den ersten Betriebmonaten noch mit Systeminstabilitäten zu rechnen ist, wurde Ende Oktober das System zunächst nur für erfahrene Nutzer, sog. Powernutzer, geöffnet und am 11. Dezember dann für alle Nutzer.

Das HLRN-IV System wurde von der Firma Atos geliefert und in Göttingen installiert. Es besteht aus

- 432 Dual-Socket Knoten mit einer standard Speicheraustattung von 192 GB
- 16 Dual-Socket Knoten mit einer großen Speicherausstattung von 768 GB
- Jeder Knoten ist ausgestattet mit
  - 2 Intel XEON Skylake Gold (6148) mit 2,4 GHz Taktung und jeweils 20 Prozessorkernen
  - 480 GB Solid-State Disk
- Netzwerk: Intel Omni-Path
- 8,1 PB paralleles LustreDateisystem (“WORK” zur Speicherung von Simulationsdaten) über Omni-Path Netzwerk
- 340 TB Heimat-Dateisystem

6 Projektberichte[2]

6.1 hbc00027: High-level calculations on defects and surfaces of semiconductors

HLRN Project ID:	hbc00027
Run time:	I/2018 – I/2019
Project Leader:	Professor Dr. Peter Deák
Project Scientists:	Dr. Bálint Aradi, Dr. Michael Lorke
Affiliation:	University Bremen, BCCMS

Overview

The functionality of semiconductors is closely connected to their defects, which control the electronic and optical behavior of the bulk material and the chemical behavior of the surface. While the standard local (LDA) and semi-local (GGA) approximations of density functional theory (DFT) have played an important role in understanding the properties of defects in traditional semiconductors, they often fail completely in wide band gap materials. In recent years, screened hybrid functionals (mixing non-local and semi-local exchange), like HSE06, have emerged as a possible replacement. The present project deals with the application, refinement and possible extension of HSE-type functionals for defects and surfaces of wide band gap semiconductors. We have found earlier that semi-empirical, material-specific tuning of the two parameters of HSE (i.e., the fraction of non-local exchange, α, and the inverse screening length, μ) can lead to a good approximation of the exact functional, and allows the calculation of defect levels in the gap with an accuracy of ~0.1 eV. While the optimized parameters work well for all defects within the given host, the transferability of the parameters to other materials is very limited. Therefore, in the past project year we have mapped the optimal parameter field for a series of Ga-based semiconductors, spanning a gap range between 1.4 and 4.7 eV. We will use the result to design an improved semi-empirical hybrid functional (with a better description of screening), having parameters transferable across the chosen set.

Our goal in the project is also to use the optimized HSE(α,μ) functionals to solve application-relevant defect problems in wide band gap semiconductors. In the past project year we have published new results on defects of GaN and β-Ga2O3, two materials with high importance for power electronics and optoelectronics. In the following year we would like to extend our study to the layer/compound GaSe.

The most important property of electronically or optically active defects is the position of their charge transition levels in the gap. To obtain that, calculations for the charged case are also needed. Calculation of charged defects in a periodic layer require corrections to eliminate the interaction of the artificially repeated charges. In the past project year we have continued our work toward a self-consistent and general charge correction scheme. We have completed a stand-alone, parallelized code for calculating the correction of the total energy even for

[2] Für den Inhalt der Projektberichte sind ausschließlich die genannten Projektleiter bzw. die Projektbearbeiter verantwortlich.

complicated charge distributions. We have tested the program by investigating the photocatalytic oxidation of CO. The results obtained by this code can now be used to test self-consistent versions built into standard electronic structure packages, like Quantum Espresso or VASP.

Results

In order to mimic the exact density functional, the parameters of the hybrid functional have to be tuned to provide a total energy which shows the correct piecewise linear behavior as a function of the occupation numbers. This translates to the simultaneous reproduction of the quasiparticle (QP) gap and the fulfillment of the generalized Koopman's theorem (gKT), i.e., the equality of the Kohn-Sham one-electron energy of the defect level with the ionization energy. We have optimized (α,μ) parameters for several Ga-based semiconductors as shown in Table 1. The values of the optimal parameters show little variation for typical bulk crystals and no clear trend with respect to the gap width. (It must be noted, though that the small differences in the screening parameter are significant for the fulfillment of the gKT and for obtaining accurate defect levels.) In contrast, the optimal parameters for the layered semiconductor GaSe are very different. This must reflect the fundamentally different screening behavior of a system, where thin layers are connected by weak Van der Waals forcesonly. In preparation for a more general hybrid functional with transferable parameters, we have modified the VASP code to allow for testing various screening functions in HSE type hybrids.

Table I. Optimized HSE parameters for (eV).

Semiconductor	QP gap (eV)	α	μ
Ga_2O_3	4.9	0.26	0.00
GaN	3.6	0.26	0.10
$CuGaS_2$ / $CuGaSe_2$	2.6 / 1.8	0.26	0.08
GaAs	1.5	0.25	0.15
GaSe	2.2	0.40	0.25

In the project year ending now, we have used the optimized parameters in Ga_2O_3 and GaN for practical defect studies. In the former, we have succeeded to identify the origin of the blue, green and red photoluminescence [1]. We have also started the identification of defect-related signatures observed in electron paramagnetic resonance [2-4]. In GaN we have investigated carbon complexes and could, for the first time, provide a complete interpretation of the rich carbon related deep level spectrum of GaN [5].

Our work on the extended and parallelized code, SLABCC, for carrying out total energy correction by means of the Komsa-Pasquarello method has been completed and published [6]. The method is based on fitting a model distribution to the excess charge, and calculating its energy assuming an isolated defect (no periodicity). The SLABCC program allows to fit complicated and highly asymmetric charge distributions using multiple Gaussians. Automatic optimization of the input parameters is possible.

Outlook

We will use the knowledge obtained in Table I to design an improved semi-empirical hybrid functional (with a better description of screening), having parameters transferable across the chosen set. We have modified the VASP electronic structure package, making it possible to utilize more general screening functions, and in the coming project year we would like to test various possibilities.

As mentioned above, the crucial point in the success of the screened hybrid functionals is the description of screening. From this point of view, surfaces and, especially, two-dimensional materials represent a challenge because of the highly anisotropic screening behavior. Therefore in the next year of our present HLRN project, we would like to extend our investigations to such systems. On the one hand, we intend to use a single-atom sheet of the wide band gap hexagonal boron nitride (h-BN), as a test case for 2D materials and, on the other hand, we will study the layered semiconductor GaSe, which is relevant for non-linear optics application. Using an HSE(α,μ) functional, optimized for bulk GaSe, we will carry out practical defect calculations, and will check, how the performance of the optimized hybrid, and the defect properties change, when going from the layered bulk material to a single layer. We will also try to optimize the HSE paraemeters for a single-layer hexganonal boron nitride (h-BN), which is a 2D semiconductor. Preliminary results show that a tuned HSE functional can reproduce the entire band structure of 2D h-BN, as obtained from a first-principle many-body (GW) calculation (see Figure 1).

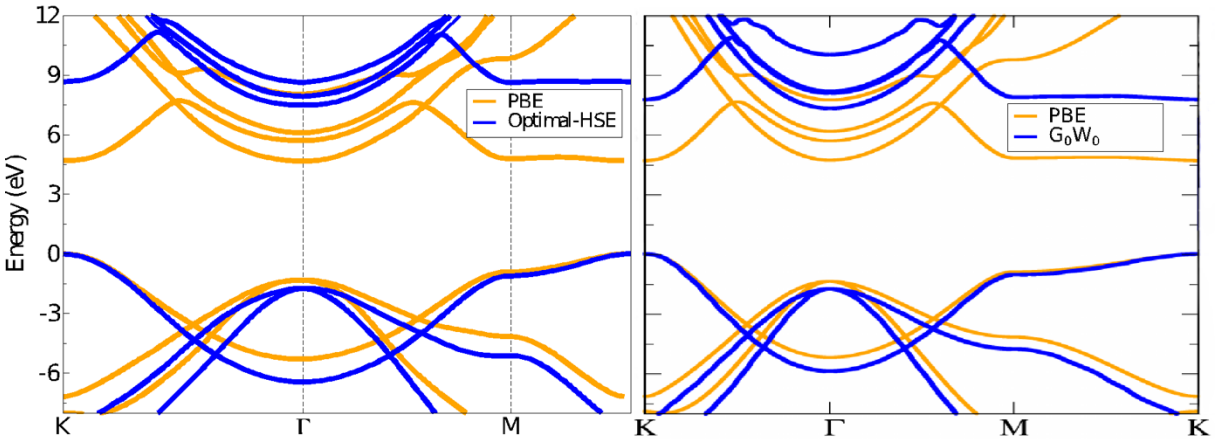

Fig.1: The band gap of h-BN between special points of the Brillouin zone. The yellow lines are the result of a GGA calculation (using the PBE functional). The blue lines come from the optimized hybrid on the left and from a first-principles G0W0 calculation on the right.

To be able to calculate charge transition levels, we will implement a self-consistent charge correction procedure into standard electronic structure packages (Quantum Espresso and VASP). We will be experimenting with two possible strategies and expect the better one to be available in the second half of the second project year.

Publications

1. Quoc Duy Ho, T. Frauenheim, and P. Deák, *Origin of photoluminescence in β-Ga_2O_3,* Phys. Rev. B *97, 115163(2018)*
2. Quoc Duy Ho, T. Frauenheim, and P. Deák, *Theoretical confirmation of the polaron model for the Mg acceptor in β-Ga_2O_3*, J. Appl. Phys. *124, 145702 (2018)*

3. H. J. von Bardeleben, S. Zhou, U. Gerstmann, D. Skachkov, W. R. L. Lambrecht, Quoc Duy Ho and P. Deák, *Proton Irradiation Induced Defects in β-Ga_2O_3 : a combined EPR and Theory Study*, Appl. Mater.*7, 022521 (2019)*
4. D. Skachkov, W. R. L. Lambrecht, H. J. von Bardeleben, U. Gerstmann, Quoc Duy Ho and P. Deák, *Computationsl identification of Ga-vacancy related electron paramagnetic resonance centers in β-Ga_2O_3,* J. Appl. Phys. *Submitted*
5. P. Deák, M. Lorke, B. Aradi, and T. Frauenheim, „*Carbon in GaN revisited with an optimized hybrid functional",* Phys. Rev. B *Submitted*
6. M. Farzalipour Tabriz, B. Aradi, T. Frauenheim, and P. Deák, *SLABCC: Total energy correction code for charged periodic slab models*, Comp. Phys. Commun. *Accepted*

Presentations

1. P. Deák: *Intrinsic carrier trapping and luminescence in β-Ga_2O_3,* CECAM-Workshop "Reliable and quantitative prediction of defect properties in Ga-based semiconductors", **invited talk,** Bremen, Oct. 8-12, 2018.
2. Michael Lorke: *Carbon in GaN revisited*, CECAM-Workshop "Reliable and quantitative prediction of defect properties in Ga-based semiconductors", **invited talk,** Bremen, Oct. 8-12, 2018.
3. Michael Lorke: *Intrinsic carrier trapping and luminescence in β-Ga_2O_3*, **invited talk***,* SPIE PHOTONICS WEST, San Francisco, Febr. 2-7, 2019

6.2 *hbc00029:* Understanding the catalytic performance of rare-earth oxides: Toward a knowledge-driven design of catalysts from first-principles calculations

HLRNProject ID:	hbc00029
Run time:	01/2018 – 12/2018
Project Leader:	Dr. Lyudmila Moskaleva
ProjectScientists:	Shikun Li; Yong Li
Affiliation:	Universität Bremen, Institut für Angewandte und Physikalische Chemie, Leobener Str. UFT, 28359, Bremen

Overview

Rare earth oxides (REOs) have shown promising performance in a set of catalytic reactions, such as oxidative elimination and dehydrogenation reactions, as well as oxidative coupling of methane (OCM), which has a tremendous economic potential because of the conversion of methane to C2 hydrocarbons. The theoretical research on the structure-property relationship of REOs can assist experimentallists in optimizing the REO-based catalysts to enhance their performance in OCM. In view of the difficult-handling of f-electrons of rare earth elements, PBE+U approach has been chosen and systematically compared to the results achieved with a hybrid functional HSE.

Results

1.1 PBE+U and HSE calculations of lanthanide sesquioxides for the evaluation of optimal U values.

Considering the rather expensive and time-consuming characteristics of the HSE method, PBE+U method is selected as the main calculation method in the whole project, in which the optimal U values are determined by comparison to the HSE calculation results. To evaluate the performance of PBE+U and systematically screen different U values, we selected animaginary reference reaction, which is the conversion reaction from lanthanide fluorides (LnF_3) to lanthanide sesquioxides, $2LnF_3 + 3H_2O \rightarrow Ln_2O_3 + 6HF$.

We have computed the structure and energies of most lanthanide sesquioxides (except for terbium, dysprosium and ytterbium) to obtain the optimal U values. The optimized lattice parameters of several lanthanide sesquioxides are listed in Table 1, the rest are not shown to save space. The equilibrium lattice parameters obtained by the HSE method are consistent with the results of the previous work.[1,2] The lighter REOs (La_2O_3, Ce_2O_3, Pr_2O_3, Nd_2O_3 and Pm_2O_3, Sm_2O_3) show the tendency of increasing lattice parameters with increasing the U values, while the lattice parameters obtained from HSE calculations are consistent with those obtained using smaller U values. On the contrary, the heavier REOs (Eu_2O_3, Gd_2O_3, Ho_2O_3, Er_2O_3) show the reverse tendency that the larger U values lead to smaller lattice parameters, the ones obtained with the larger U values being much closer to those of HSE calculations.

Table 1. The equilibrium lattice parameters of Ln_2O_3 (Ln = La, Ce, Pr, Nd, Pm, Sm, Eu, Gd, Ho, Er, Tm, Lu) calculated by PBE+U (U = 1-8) and HSE methods.

REOs	Lattice-parameter	PBE+U								HSE
		U=1	U=2	U=3	U=4	U=5	U=6	U=7	U=8	
La_2O_3	a	3.95	3.95	3.96	3.97	3.97	3.98	3.99	3.99	3.91
	c	6.18	6.20	6.21	6.22	6.22	6.23	6.24	6.25	6.14
	volume	83.36	83.86	84.28	84.82	85.16	85.57	85.93	86.30	81.38
Ce_2O_3	a	3.89	3.90	3.91	3.92	3.92	3.93	3.94	3.94	3.86
	c	6.12	6.15	6.16	6.17	6.18	6.19	6.19	6.23	6.09
	volume	80.05	80.85	81.46	81.96	82.39	82.81	83.24	83.74	78.49
Pr_2O_3	a	3.84	3.86	3.86	3.87	3.88	3.89	3.89	3.90	3.82
	c	6.02	6.04	6.06	6.08	6.09	6.11	6.12	6.13	6.00
	volume	77.52	78.34	78.85	79.48	79.87	80.27	80.61	80.94	76.26
Nd_2O_3	a	3.83	3.84	3.84	3.85	3.86	3.86	3.87	3.87	3.80
	c	6.05	6.07	6.08	6.10	6.09	6.11	6.11	6.12	6.02
	volume	76.72	77.29	77.80	78.25	78.49	78.83	79.21	79.49	75.30
Pm_2O_3	a	3.82	3.83	3.83	3.84	3.84	3.84	3.85	3.85	3.79
	c	6.01	6.00	6.01	6.03	6.05	6.05	6.05	6.07	5.97
	volume	75.94	76.11	76.45	76.81	77.34	77.40	77.56	77.87	74.23
Sm_2O_3	a	3.78	3.79	3.79	3.80	3.80	3.81	3.81	3.80	
	c	5.96	5.98	5.97	5.99	6.01	6.01	6.02	6.01	
	volume	74.30	74.73	74.85	75.15	75.28	75.46	75.74	75.50	
Eu_2O_3	a	3.81	3.81	3.81	3.81	3.80	3.80	3.79	3.78	3.78
	c	5.93	5.93	5.92	5.95	5.94	5.98	6.03	6.02	5.90
	volume	74.58	74.69	74.46	74.73	74.51	74.69	75.08	74.18	73.03
Gd_2O_3	a	3.75	3.75	3.75	3.74	3.74	3.74	3.73	3.72	3.72
	c	5.96	5.96	5.96	5.96	5.96	5.96	5.94	5.93	5.93
	volume	72.51	72.51	72.46	72.17	72.17	72.17	71.64	71.13	71.20
Ho_2O_3	a	3.70	3.69	3.68	3.68	3.64	3.60	3.57		3.67
	c	5.86	5.85	5.84	5.84	5.82	5.79	5.76		5.86
	volume	68.51	68.06	67.54	67.54	66.22	64.84	63.04		67.66
Er_2O_3	a	3.66	3.66	3.66	3.65	3.65	3.65	3.64	3.63	3.63
	c	5.82	5.83	5.84	5.86	5.83	5.91	5.87	5.85	5.80
	volume	67.62	67.73	67.61	67.71	67.20	68.23	67.47	66.89	66.43
Tm_2O_3	a	3.65	3.65	3.62	3.61	3.60	3.58	3.57	3.53	3.62
	c	5.82	5.83	5.78	5.82	5.81	5.86	5.83	5.75	5.82
	volume	66.70	66.88	65.84	65.55	64.88	65.45	64.40	62.48	65.75
Lu_2O_3	a	3.57	3.56	3.54	3.52	3.50	3.48	3.44	3.40	3.59
	c	5.61	5.59	5.59	5.57	5.55	5.53	5.45	5.38	5.75
	volume	62.13	61.39	60.80	59.98	58.99	58.11	55.91	54.04	64.16
CeO_2	a	5.48	5.49	5.49	5.50	5.50	5.51	5.51	5.52	5.39
	volume	164.26	165.30	165.75	166.23	166.50	167.16	167.65	168.05	156.97

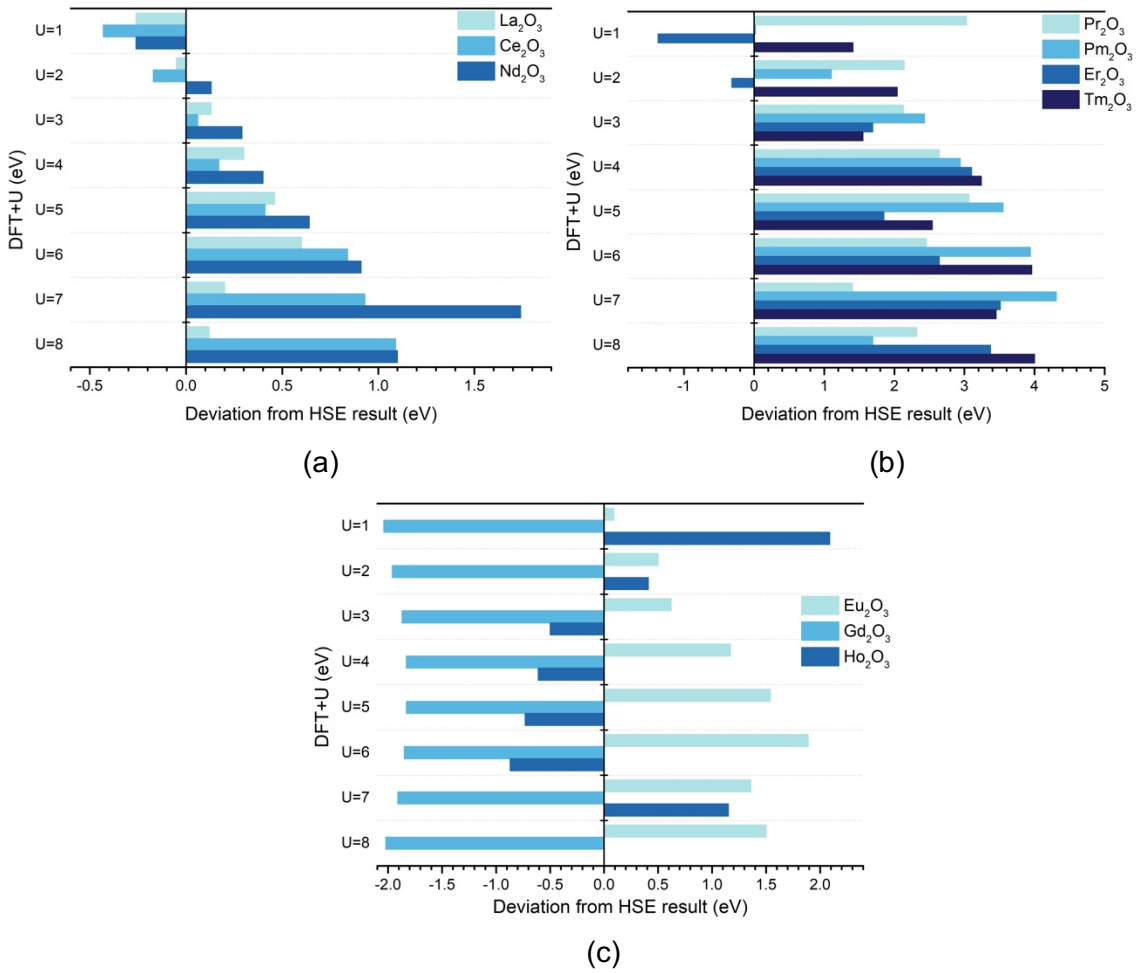

Figure 1. The difference of the reaction energies of the conversion from LnF_3 to Ln_2O_3 between the PBE+U (U=1-8) and HSE methods, (a) Ln=La, Ce, Nd (b) Ln=Pr, Pm, Er, Tm (c) Ln=Eu, Gd, Ho.

The above-mentioned reaction energies of the conversion from LnF_3 to Ln_2O_3 calculated by PBE+U and HSE methods are compared in Figure 1. All of the reaction energies get larger with increasing the U values, the smaller U values providing the best agreement with the HSE results. For lighter lanthanides this tendency is similar to that of lattice parameters. However, for the heavier REOs (Eu_2O_3, Ho_2O_3 and Er_2O_3) there are differences between the optimal U values for lattice parameters and for reaction energies. In view of the importance of the reaction energies for modeling catalytic mechanisms, we propose to take the smaller U values resulting in the best fit for energies as the optimal ones, which lie in the range of 2-3 eV for almost all of the listed lanthanides sesquioxides. Therefore, taking a smaller U value should be a relatively reasonable and safe choice when treating the systems related to lanthanides oxides.

1.2 O_2 adsorption and CO oxidation mechanism on gold-supported ceria nanoparticle

In addition to the calculation of the lanthanide bulk oxides, we also focus on lanthanide nanoparticles to illustrate the application of PBE+U method in the nanoparticles. Herein the gold-supported ceria nanoparticles have been chosen because ceria has been most commonly used to functionalize bulk gold and nanoporous gold, to enable O_2 activation and aerobic oxidation reactions. Plenty of oxygen defects were observed in such supported oxide particles.[3] In this work, we constructed computational models to address the structural and

adsorption properties of supported CeO_2 nanoparticle and to theoretically explore the oxygen adsorption and carbon monoxide oxidation mechanism on Au-supported ceria.

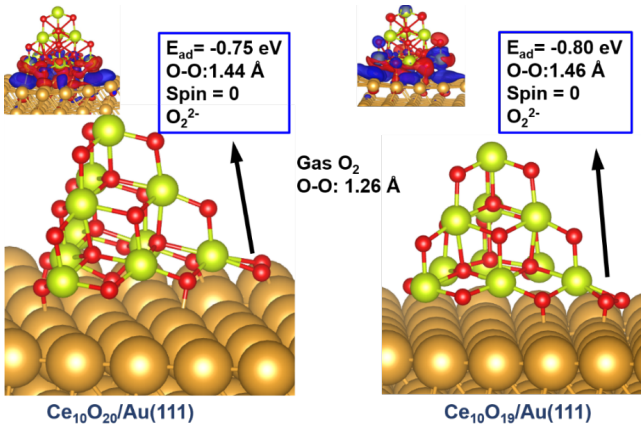

Figure 2. The most energetically favored O_2 adsorption sites for the Au-supported $Ce_{10}O_{19}$/$Ce_{10}O_{20}$ cluster.

Previous studies found that oxygen molecule can adsorb and can be activated at the oxygen vacancy site of ceria-supported gold nanoparticle system (an inverse system to the one considered in our work). It is also well known that dioxygen does not adsorb on a perfect ceria surface.[4] Therefore, it will be important and necessary to determine whether oxygen adsorption and activation on gold-supported ceria and on ceria-supported gold nanoparticles share the same mechanism. We considered two types of gold-supported ceria nanoparticles, $Ce_{10}O_{19}$ with oxygen vacancy and $Ce_{10}O_{20}$ without oxygen vacancy. In the non-defected stoichiometric $Ce_{10}O_{20}$ cluster all Ce atoms have a formal oxidation state (IV). In the $Ce_{10}O_{19}$ system with one oxygen vacancy site, two of the Ce ions become Ce(III) , which amounts to 20% Ce(III). The adsorption energies of O_2, the O-O bond lengths, the spin population of adsorbed O_2 molecules at the most favorable adsorption sites are given in Figure 2. Other possible adsorption sites and geometric configurations for O_2 adsorbed at gold-supported ceria nanoparticles are not shown in view of the limited space. The most energetically favorable adsorption site for both cases is a bottom corner of the pyramidal ceria cluster, interfacing with the Au(111) surface. The spin population of adsorbed O_2 molecules in both gold-supported $Ce_{10}O_{19}$ and $Ce_{10}O_{20}$ clusters is 0, implying a change from a triplet O_2 to a singlet O_2^{2-} with the bond lengths of 1.46 and 1.44 Å, as well as adsorption energies of -0.80 and -0.75 eV, respectively. The O_2 adsorption is just slightly more energetically favorable on the defected model than on the perfect model by 0.05 eV, which shows that the oxygen vacancy in the gold-supported system is not the decisive factor for oxygen adsorption and activation. As shown in Figure2, the electron density accumulates on the interface of ceria and gold. Such an increase of electron density can promote the adsorption and activation of O_2. Therefore, we conclude that the charge polarization between the two phases of ceria and gold is likely a decisive factor for O_2 adsorption and activation.

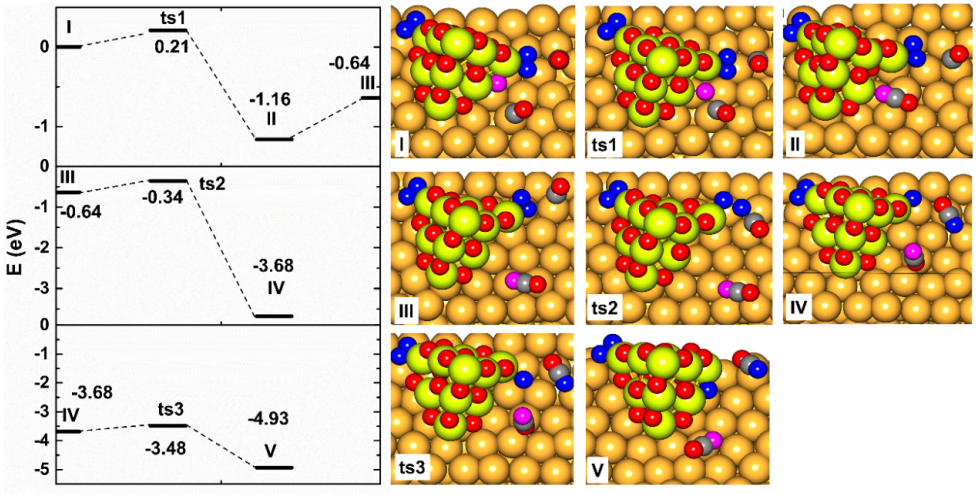

Figure 3. Theoretically predicted mechanism of CO oxidation catalyzed by Au-supported ceria cluster. The left panel shows the energy profile of the reaction path, the right panel gives the geometries of the reactant, intermediates, transition states and products. The whole reaction mechanism includes three main steps: first, CO oxidation with the edged O atom of ceria nanoparticle and CO_2 desorption (I-ts1-II-III,); second, CO oxidation by activated O_2^{2-} (III-ts2-IV); and third, the O migration to fill the O vacancy (IV-ts3-V). Color coding: Au, orange; Ce, lime; O, red and magenta; adsorbed O_2, blue; C, gray.

The catalytic reaction mechanism and the related geometries of CO oxidation on ceria-supported gold nanoparticle are given in Figure 3. Several mechanisms of CO oxidation have been theoretically proposed for ceria-supported Au nanoparticles, in which CO either directly reacts with pre-adsorbed O_2 molecules or with the lattice oxygen atom of ceria, according to a Mars-van Krevelen type of mechanism.[5-7] A recent study suggested that CO reaction with pre-adsorbed O_2 is less preferred because of a weak adsorption of O_2 on the gold cluster and its interface.[8] In the present study of the gold-supported ceria cluster, the O_2 molecule strongly binds at the interface in both defected and non-defected systems with a strongly weakened O-O bond offering it a chance to react with the CO molecule. It has been reported that the oxygen vacancy concentration in gold-supported ceria varied from 3% to 18% depending on the coverage of CeO_2 on the gold surface, 6 which is consistent with the theoretical model of gold-supported $Ce_{10}O_{19}$ cluster with 5% of oxygen atoms missing. The pre-adsorption of both CO and O_2 molecules was also considered in this system in combination with the AIMD simulation simulating the reaction processes of CO and O_2 in the gold-supported ceria system. As discussed above, the adsorption of O_2 on Au-supported $Ce_{10}O_{19}$ releases 0.80 eV energy, lengthening O-O bond distance from 1.26 to 1.46 Å, transferring 2 electrons to O_2 forming O_2^{2-} species. Two O_2 and CO molecules in the gold-supported $Ce_{10}O_{19}$ chemical model show the average adsorption energy of O_2 at -0.78 eV, which indicates no adsorption change due to higher adsorbate coverage. In the AIMD simulation of mixed CO and O_2 molecules at 700 K, CO molecules are oxidized as shown in Figure 3. The first CO molecule reacts with the lattice O atom leaving one oxygen vacancy behind rather than with the activated O_2^{2-} species, and the second CO molecule reacts with the O_2^{2-} species forming a CO_2 molecule and generating an O atom coordinated to the corner Ce atom. That oxygen atom migrates to the oxygen vacancy site regenerating the complete framework of $Ce_{10}O_{19}$. In reaction path I-ts1-II, Figure 3, CO reacts with an O atom of ceria nanoparticle at the gold/ceria interface forming a CO_2 molecule with a low of barrier only 0.21 eV and releasing 1.16 eV energy. For comparison, the activation barrier for the CO reaction with adsorbed O_2 is computed as 0.36 eV, implying that it is less preferred in than the CO

reaction with the lattice O atom of the ceria nanoparticle. The generated CO_2 adsorbs on a Ce atom in a slightly bent geometry; it can desorb into gas phase consuming the energy of 0.52 eV through II-III reaction path. The second CO molecule was oxidized by the activated O_2^{2-} species forming CO_2 and leaving an O atom coordinated to Ce atom in III-ts2-IV reaction path. The activation barrier and reaction energy were computed as 0.30 and -3.04 eV, respectively. The CO_2 molecule can directly desorb into the gas phase. The O atom coordinated to the corner Ce atom as a result of CO oxidation is thermodynamically unstable; therefore, it prefers to migrate to the oxygen vacancy site as shown in IV-ts3-V reaction path. The activation barrier for migration and the reaction energy were predicted as 0.20 and -1.25 eV, respectively.

Hence, we have identified a low-energy reaction path involving both the lattice oxygen and a direct reaction of O_2 with CO, but no O_2 dissociation without the assistance of CO.

Outlook

In the next phase of the project, we will aim at the adsorption properties of molecular oxygen and methane on pure and doped lanthanide oxides or binary reactions systems (e.g. LaCe), as well as the acidity-basicity properties of doped or undoped lanthanide oxides. The adsorption of CH_4 and the activation of the C-H bond are the first two steps of OCM on REOs surfaces. They can be respectively explored by computing the binding energy of CH_4 and CH_3·at active sites and the enthalpy and activation energy of the direct H abstraction from CH_4 that are likely important descriptors for the activity and selectivity of OCM. The adsorption of O_2 on REOs surface leads to the formation of oxygen vacancies at the surface. We will choose one or two REOs to be doped with impurities, such as alkali metal atom or another lanthanide atom, which will be compared to undoped oxides with regards to the adsorption of CH_3, the bond-breaking of C-H in methane and the O-O bond in dioxygen.

Presentations

1. Shikun Li, Yong Li, Marcus Bäumer, Lyudmila V. Moskaleva. Theoretical study on the structures and thermodynamics of A-type rare earth sesquioxides by HSE and PBE+U methods. CECAM Workshop - Correlated electron physics beyond the Hubbard-model, 2019, Bremen, Germany.

References

(1) Da Silva, J. L.; Ganduglia-Pirovano, M. V.; Sauer, J.; Bayer, V.; Kresse, G. Physical Review B 2007, 75, 045121.
(2) Andersson, D. A.; Simak, S. I.; Johansson, B.; Abrikosov, I. A.; Skorodumova, N. V. Physical Review B 2007, 75.
(3) Rodriguez, J. A.; Ma, S.; Liu, P.; Hrbek, J.; Evans, J.; Pérez, M. Science 2007, 318, 1757.
(4) Chen, H.-T.; Chang, J.-G.; Chen, H.-L.; Ju, S.-P. J. Comput. Chem. 2009, 30, 2433.
(5) Zhang, C.; Michaelides, A.; Jenkins, S. J. Phys. Chem. Chem. Phys. 2011, 13, 22.
(6) Kim, H. Y.; Lee, H. M.; Henkelman, G. J. Am. Chem. Soc. 2012, 134, 1560.
(7) Song, W.; Hensen, E. J. M. Catalysis Science & Technology 2013, 3, 3020.
(8) Wang, Y.-G.; Mei, D.; Glezakou, V.-A.; Li, J.; Rousseau, R. Nature Communications 2015, 6, 6511.

6.3 *hbc00030:* Dynamics of fluoride anions in all-silica and silico-germanate zeolites

HLRNProject ID:	hbc00030
Run time:	II/2018 – I/2019 *(extension proposal submitted)*
Project Leader:	Dr. Michael Fischer
ProjectScientists:	Dr. Michael Fischer, Prof. Dr. Reinhard X. Fischer *(research group leader)*, Ana Palacios Saura *(student assistent)*
Affiliation:	Crystallography Group, Department of Geosciences, University of Bremen, KlagenfurterStraße 2-4, 28359 Bremen

Overview

In this project, *ab-initio* molecular dynamics calculations are used to study the dynamic behaviour of fluoride anions confined to small cages in zeolite structures. One part of the calculations addresses the local environment and dynamics of fluoride anions in double four-ring cages in silicogermanates having the AST topology, covering the full range of compositions from pure SiO_2 to pure GeO_2. Furthermore, the influence of the organic cation on the fluoride dynamics in MFI-type Silicalite-1 is investigated. Calculations envisaged for the continuation period will include further studies on the AST- and MFI-type systems, as well as simulations covering a larger range of zeolite frameworks.

Scientific background

Zeolites are a class of inorganic porous materials with important applications in ion exchange, gas and liquid separation, and catalysis.[1] Zeolite structures consist of a three-dimensional framework of tetrahedrally coordinated atoms connected by oxygenatoms. A rich variety of zeolite structures has been reported: To date, more than 240 distinct framework types have been recognised by the International Zeolite Association, who assigns three-letter framework type codes like “AST” or “MFI” to each framework. Prototypical zeolites, such as zeolite minerals, possess a negatively charged aluminosilicate framework whose charge is balanced by extra-framework cations. However, the development of sophisticated synthesis routes has led to the discovery of zeolite-like materials having a neutral framework, among them all-silica zeolites (compositionSiO_2), germanates (GeO_2), silicogermanates ($Si_xGe_{1-x}O_2$), aluminophosphates ($AlPO_4$), and gallophosphates ($GaPO_4$).

The synthesis in the presence of fluoride anions ("fluoride route") is a particularly successful strategy to obtain neutral-framework zeotypes with very open frameworks and low defect concentrations. Various zeolites and zeotypes with unprecedented framework topologies can be synthesised via this route.[2,3] In the as-synthesised zeolites, the fluoride anions occupy well-defined positions in the crystal structure,balancing the charge of the cationic organic structure directing agents (OSDAs) that are used to promote the formation of a particular framework. Two different fluoride environments can be distinguished in this context: Inzeolites having double four-ring (*d4r*) cages, the fluorideanions occupy the centre of this cage. This is shown for the example of octadecasil (AST topology) in **Fig. 1**. In structures without *d4r* units, fluoride anions alsotend to occupy small cages. However, rather than being located at the cage centre, they are covalently bonded to a single silicon atom, forming

trigonal-bipyramidalSiO_4F^- units. Frequently, the fluoride anions are disordered over two or more positions, as shown for the case of MFI-type Silicalite-1 in **Fig. 1**.

In this project, the dynamics of fluoride anions confined to small cages in zeolite structures are studied using *ab-initio* molecular dynamics (AIMD) calculations. These investigations are carried out in the context of the project "*Beyond tetrahedral coordination in zeolite-type materials - A computational approach*" (project no. 389577027, Fi1800/5-1), funded by the Deutsche Forschungsgemeinschaft (DFG - German Research Foundation) since May 2018.

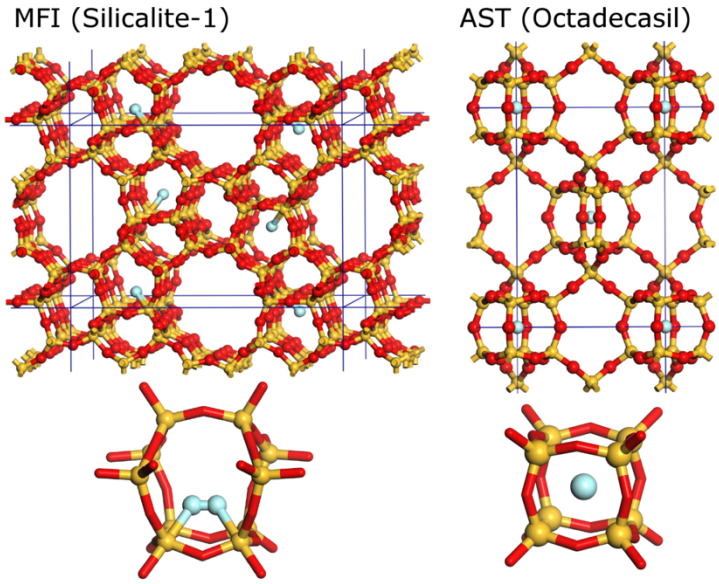

Fig. 1: Crystal structures of the all-silica zeolites Silicalite-1 (MFI topology) and octadecasil (AST topology). The OSDA molecules occupying the larger cages/channels are omitted for clarity. The lower part of the figure visualises the fluoride environment, including the disorder over two equivalent positions in Silicalite-1.

Results

1) AST-type silicogermanates: The AST framework is a prototypical zeolite with *d4r* building units that is synthetically accessible across the range of $Si_xGe_{1-x}O_2$ compositions.[4] Interestingly, some conflicting observations regarding the equilibrium position of fluoride within the cage have been reported: While crystallographic experiments locate fluoride at the cage centre, previous computational studies postulated a formation of covalent Ge-F bonds in germanium-containing *d4r* units.[5] To elucidate the equilibrium position of fluoride, structure optimisations in the framework of dispersion-corrected density functional (DFT) were performed for a variety of AST models with different Ge contents. While fluoride anions occupy the centre of the *d4r* cage in the pure end members, SiO_2-AST and GeO_2-AST, they form a partly covalent Ge-F bond in many silicogermanates, e.g. in the system containing a single Ge atom at one vertex of the cage (**Fig. 2**).

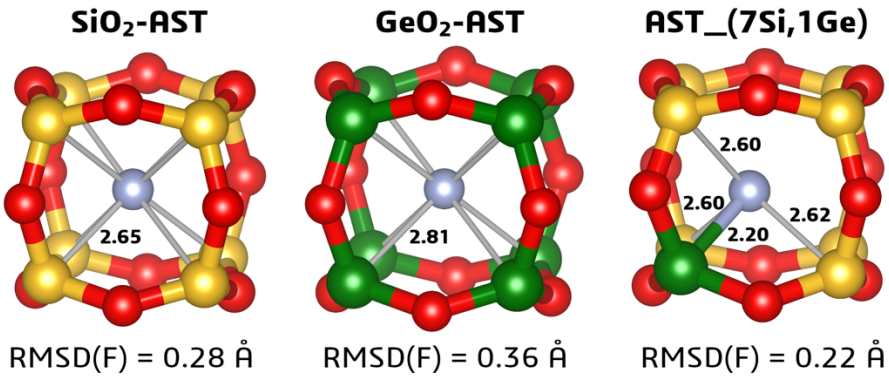

Fig. 2: Fluoride-containing *d4r* cages in AST-type zeolites as obtained from DFT optimisations. Selected T-F distances are given in Å. The RMSD is a measure of the freedom of motion, with larger RMSD values corresponding to a more dynamic behaviour.

A systematic comparison of different Si,Ge arrangements for a given composition showed that those arrangements which maximise the number of Ge-O-Gelinkages tend to be energetically favoured. AIMD simulations were then performed for selected models in order to elucidate the influence of the local environment on the dynamic behaviour of the fluoride anions. These calculations revealed that the fluoride anions exhibit a much larger freedom of motion in systems without localised Ge-F bonds, leading to significantly larger root mean square displacements (RMSDs, see values included in **Fig. 2**). The anions primarily oscillate around their equilibrium position, and there were no indications for coexistence of different local minima within one cage. The results for AST-type silicogermanates have been published recently in *The Journal of Physical ChemistryC* (see project-related publication).

2) Silicalite-1: MFI-type zeolites like ZSM-5 and Silicalite-1are of considerable relevance for applications, primarily in catalysis (e.g. xylene isomerisation) and separation. For the case of as-synthesised Silicalite-1, it has been shown that the fluoride disorder is of a dynamic nature at room temperature, i.e. the anions move back and forth between adjacent positions on a very short timescale that is accessible with nuclear magnetic resonance (NMR) experiments. Upon cooling to cryogenic temperatures, characteristic changes in the NMR spectra show that the dynamic motion is frozen out.[6] Moreover, the extent of the dynamic disorder at room temperature depends on the OSDA: If tetrapropylammonium (TPA^+), the most typical OSDA in the synthesis of Silicalite-1, is replaced by methyltributylammonium ($MTBA^+$), the dynamic disorder at room temperature disappears, presumably due to stronger interactions between the positively charged OSDA molecules and the fluoride anions.[7] Since NMR experiments can only give indirect insights into the local structure, DFT-based AIMD simulations were performed for Silicalite-1 models incorporating fluoride anions and differently sized OSDAs of the general form tetra-X-ammonium, where X = methyl/ethyl/propyl/butyl (TMA^+/TEA^+/TPA^+/TBA^+). Calculations for room temperature showed only a small number of dynamic “events” in which a fluoride anion moves from one position to another, indicating that the timescale of the fluoride anion dynamics is too long to be sampled with this method (the AIMD simulations typically sample ~20 picoseconds). However, the frequency of dynamic events increases with temperature, and an increase of the simulation temperature to 100 °C or 200 °C permitted the extraction of some statistical information, specifically the average amount of time that passes between two dynamic events (“residence time”). As is visible in **Fig. 3**, the residence time increases with increasing size of the OSDA, i.e. the presence of a larger OSDA slows down the fluoride anion dynamics. Interestingly, an analysis of the radial distribution functions between fluoride anions and the nitrogen atoms of the positively charged OSDAs contradicts the previously

published hypothesis that shorter N-F distances lead to a suppression of dynamic disorder.[7] In fact, the opposite is true: The shortest N-F distances are found in MFI_TMA, the system with the smallest OSDA.

Outlook

The calculations envisaged for the continuation phase of the project will address three different aspects:

(1) Further calculations for AST-type systems will look at other framework compositions, primarily alumino- and gallophosphates, and compare them to the SiO_2- and GeO_2-AST systems that have already been studied.

(2) Additional work on MFI-type Silicalite-1 will concentrate on OSDAs having alkyl chains of different lengths, such as the $MTBA^+$ cation, which has been found to suppress the room-temperature dynamic disorder.[7]

(3) A set of other zeolite structures that exhibit a varying degree of fluoride anion disorder will be studied. This set includes, among other systems, ITQ-4 (IFR topology) and SSZ-35 (STF topology), which show a qualitatively different behaviour (disorder in ITQ-4, no disorder in SSZ-35), despite the similar fluoride environment in both structures.[8]

Altogether, these calculations will deliver atomic-level insights into the dynamics of fluoride anions under confinement, thereby contributing to an improved understanding of the structure-directing role that fluoride anions play during zeolite synthesis.

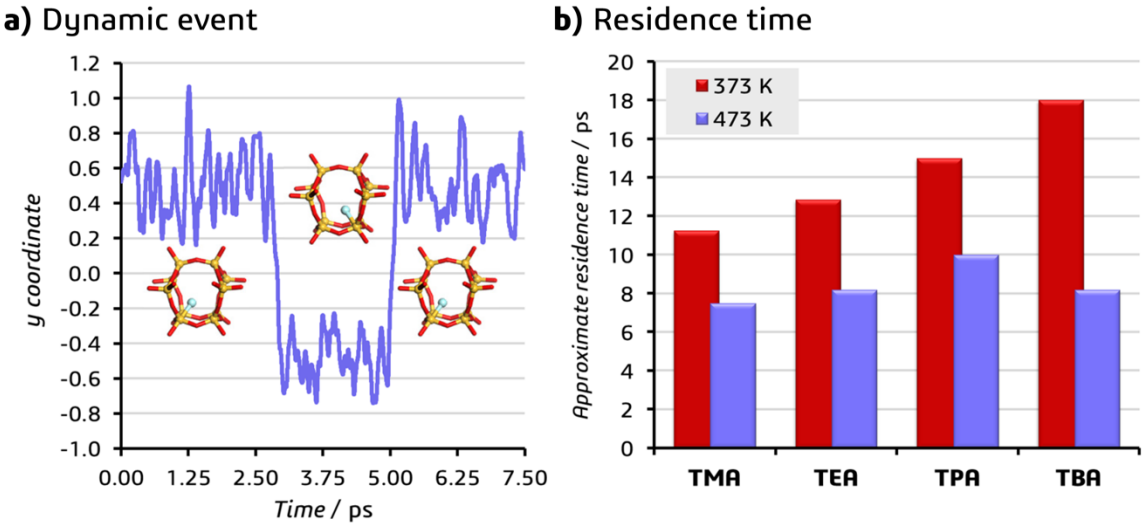

Fig. 3: a) Visualisation of dynamic "events" – in this example, the fluoride anion changes its position twice over the course of the AIMD trajectory. **b)** Fluoride residence times derived from AIMD simulations for Silicalite-1 models containing different OSDAs.

Project-related publication

P1 M. Fischer, *Local Environment and Dynamic Behavior of Fluoride Anions in Silico-germanate Zeolites: A Computational Study of the AST Framework*, J. Phys. Chem. C *123, 1852–1865, (2019)*

Project-related presentation

P2 M. Fischer, *First-principles calculations elucidate the dynamic behaviour of fluoride anions in all-silica and silicogermanate zeolites*, poster presentation at the 31st German Zeolite Meeting (DZT31), Dresden, March 2019

References

[1] A. F. Masters, T. Maschmeyer, Microporous Mesoporous Mater. *142, 423–438 (2011)*
[2] M. A. Camblor, L. A. Villaescusa, Top. Catal. *9, 59–76 (1999)*
[3] P. Caullet, J. Paillaud, A. Simon-Masseronet al., Comptes Rendus Chim. *8, 245–266 (2005)*
[4] Y. Wang, J. Song, H. Gies, Solid State Sci. *5, 1421–1433 (2003)*
[5] A. Pulido, G. Sastre, A. Corma, ChemPhysChem *7, 1092–1099 (2006)*
[6] H. Koller, A. Wölker, L. A. Villaescusa et al., J. Am. Chem. Soc. *121, 3368–3376 (1999)*
[7] S. L. Brace, P. Wormald, R. J. Darton, Phys. Chem. Chem. Phys. *17, 11950–11953 (2015)*
[8] L. A. Villaescusa, P. S. Wheatley, I. Bull et al., J. Am. Chem. Soc. *123, 8797–8805 (2001)*

6.4 *hbc00031:* Mechanical Properties of Aggregated Nanoparticle Films

HLRNProject ID:	hbc00031
Run time:	III/2018 – II/2019
Project Leader:	Prof. Dr.-Ing. Lutz Mädler
ProjectScientists:	Valentin Baric
Affiliation:	University of Bremen

Overview

Aggregated nanoparticle films are applied in a variety of different fields including catalysis, gas sensing or battery materials, because of their high specific surface area, high porosity, pore structure and high number of percolation paths. Especially the high porosity, however, often leads to mechanically unstable films, that, e.g. disintegrate in liquid environments. The compaction at low pressures has proven to increase this stability while preserving important characteristics, including high specific surface area, percolation paths and accessible pores. The exact determination of the rearrangement during the compaction and the exact film characteristics, i.e. pore geometry and number of particle-particle contacts, however, remains inaccessible to experiments. The knowledge about these characteristics can help to understand and improve conditions for fluid flows or the connectivity of particles relevant for electric conductivity.

In this project, we aim to model the films and their rearrangement during mechanical compaction. The Discrete Element Method (DEM) is capable of simulatenously compute the trajectories of millions of primary particles. These particles can interact via contact models, that correlate their distance with a contact force. At nanoscale, these forces are dominated by attractive forces including capillary forces, while body forces, such as gravity and inertia become negligible. Therefore, in previous projects (hbc00012 All-atom moleculardynamic investigations of the adhesion mechanisms at the contact interface of TiO_2 nanoparticles in films and aggregates) we have developed a contact model that describes the unbonded interactions of TiO_2 primary particles with a few nanometers in diameter. This contact model was combined with a contact model to represent sinter bridges in nanoparticle aggregates and implemented into LIGGGHTS (open-source DEM software) to compute the compaction of nanoparticle films.

Results

The contact models for non-bonded and sinter bridge particle-particle contacts were applied to ballistically deposited nanoparticles, typically for TiO_2 obtained from the gas phase. Additionally, models for rigid, inflexible aggregates and single particles were applied to study the importance of elastically deforming sinter bridges.

The procedure of the compaction of 600,000 primary particles is shown in Fig 1. The films were compacted between two compacting walls at a constant velocity. As soon as the targeted pressure acted on the compacting walls, the wall was raised to release the stress on the films. This resulted in a film relaxation, as visible from the porosity increase. The acting compaction pressure – porosity relationship clearly depends on the applied sinter bridge model (Fig. 2). While rigid aggregates and single particles resulted in the largest and lowest porosity at given compaction pressure, respectively, the elastically deforming sinter bridges gave intermediate porosity at given compaction pressure. Additionally, this relationship could

be controlled using the tensile/shear strength of the sinter bridges, that is the maximum deformation, before a sinter bridge irreversibly breaks. Therefore, the mobility of the aggregates (or primary particles) is an important characteristic during the compaction. Smaller objects (fragments of aggregates or primary particles) result in denser films at given compaction pressure.

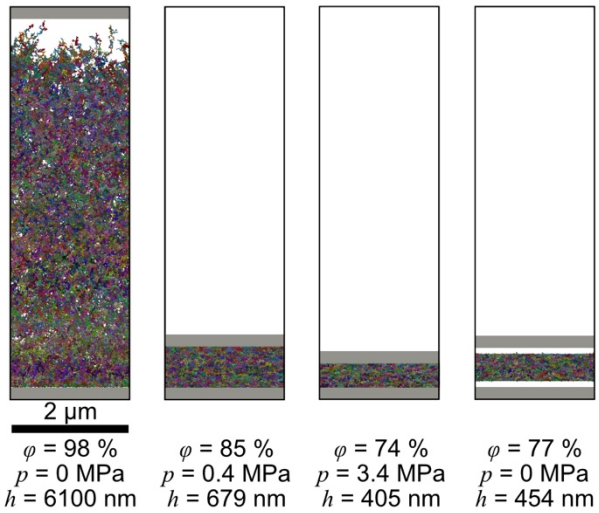

Fig. 1: Compaction procedure in DEM. The film was compacted between two walls at a constant velocity until the desired pressure acted on the walls. Then, the upper wall was raised to release any stress of the film [1].

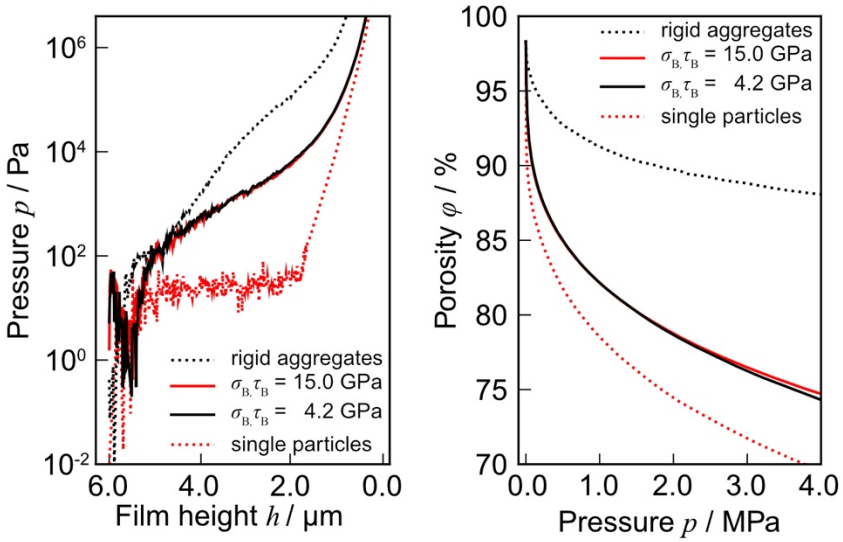

Fig. 2: The continuous pressure acting on the walls at given film height (left) and the resulting porosity (right) during film compaction. Depending on the selected sinter bridge model (rigid, unflexible aggregates, elastically deforming sinter bridge or single particles) and the sinter bridge parameters, the porosity at given compaction pressure can be obtained [1].

The porosity and pore size distribution of the relaxed films were compared to the characteristics of experimentally compacted TiO_2 films (Fig. 3). Rigid aggregates and single particles clearly over- and underestimated the porosity-compaction pressure relationship of the experiments. Elastically deforming sinter bridges, however, resulted in an almost perfect match of the porosity at given compaction pressure. The applied sinter bridges with a Young's modulus of E_b = 56.0 GPa and a tensile/shear strength σ_B,τ_B = 15.0 GPa are in striking agreement with the experiments above about 1.0 MPa compaction pressure. The discrepancy at low compaction pressures can be ascribed to different initial film structures. The experimental films experienced a film compaction during synthesis from the deposition on a filter, while the simulations start from ballistically deposited particles.

In the simulations using the elastically deforming sinter bridges none of the sinter bridges broke. Therefore, it is important to model nanoparticle aggregates with highly flexible and stable sinter bridges.

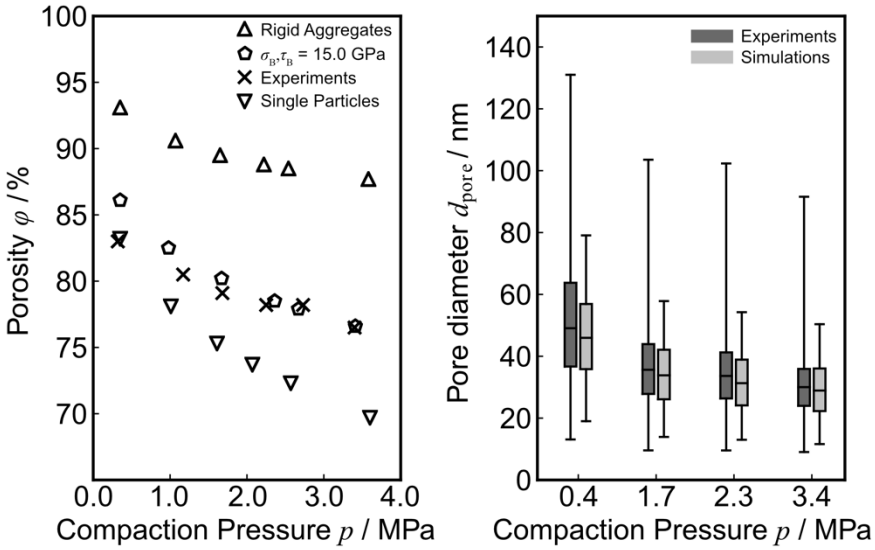

Fig. 3: The porosity (left) and the pore size distribution (right) of the films after pressure release. Using the elastic sinter bridge model, the experimentally obtained porosity and pore size distribution at given compaction pressure can perfectly be reproduced [1].

Also, the pore structure of experiments and simulations (elastic sinter bridges) are in striking agreement (Fig. 3, right). Only very large pores found in the experiments were absent in the simulations. The necessary number and hence, probability, of such large pores to provide the measured pore area, however, is very low. The simulated particle films is too small for such a pore to be likely.

Outlook

The particle film models are of great relevance for, e.g. applications involving fluid flows. The migration of the fluids through the complex pore structure can only be understood if the exact film is known. Therefore, in a following project, the pore structure of the films could be discretized and fluid flows in the pores could be computed using Computational Fluid Dynamics (CFD). The coupling of these simulations with DEM could even result in the rearrangement of the particle films caused by the fluids.

Additionally, the modeled film structures can help to resolve particle-particle contacts relevant for electric conductivity. Especially, the ratio of non-bonded contacts and sinter bridge contacts determines this conductivity, which is experimentally unfeasible. Here, the simulations can complement the experiments and relate, e.g. sensitivity of gas sensors to particle properties including particle size or film properties such as pore size and porosity.

Publications

1. V. Baric, L. Colombi Ciacchi, L. Mädler, *Compaction-induced restructuring of aggregated nanoparticle films using the discrete element method,* Powder Technology*, 342, 773-779 (2019)*

6.5 *hbc00023, hbc00025, hbc00028:* HLRN Projects of the Hybrid Materials Interfaces Group (HMI)

Technical Details:

HLRN Project ID:	**hbc00023**
Title:	Adsorption of binding peptides on ZnO. Towards a quantitative understanding of organic-inorganic interactions
Run time:	III/2017 – II/2018
Project Leader:	Dr. Massimo Delle Piane
Project Scientists:	Dr. Monika Michaelis, Dr. Steffen Lid, André Wark
HLRN Project ID:	**hbc00025**
Title:	Polymer hybrid materials – Atomistic Modelling of the Formation of a Thermo-set/Thermoplastic Interphase during Co-Curing
Run time:	III/2017 – II/2018
Project Leader:	Prof. Dr. Lucio Colombi Ciacchi
Project Scientists:	Dr. Massimo Delle Piane, Magdalena Laurien, Nils Hildebrand
HLRN Project ID:	**hbc00028**
Title:	Searching for an electronic fingerprint on 2D materials
Run time:	I/2018 – IV/2018
Project Leader:	Dr. Massimo Delle Piane
Project Scientists:	Sebastian Potthoff
Affiliation:	Hybrid Materials Interfaces Group, Bremen Center for Computational Materials Science, Faculty of Production Engineering, University of Bremen, Germany

hbc00023: Adsorption of binding peptides on ZnO. Towards a quantitative understanding of organic-inorganic interactions

Overview

The specific binding of peptides to biomolecular receptors is key to the regulation of biological processes such as cell adhesion or antibody recognition. The concept of molecular recognition can be extended to the field of materials science with individual peptide

sequences that selectively bind to inorganic mineral phases. Extending this concept further, sequences that recognize certain materials classes, inorganic compounds or even crystallographic facets of the same material have been identified, leading to highly promising applications in bio-nanotechnology. In this project we focus on zinc oxide (ZnO), aiming at a quantitative determination of the binding characteristics (binding free energy, adhesion forces) of ZnO-binding peptides interacting with the non-polar (10-10) surface of ZnO. The results will be interpreted in terms of both the primary peptide structures and of changes of peptide conformation (secondary structure) after adsorption.

Current results

This project ran through its first application period. We focused on five different peptides in our simulations, which have been identified by our experimental coworker using Phage display. The five ZnO-binding peptide structures were created using *De novo* secondary structure prediction tools and their conformational space was investigated through Molecular Dynamics coupled with Replica Exchange with Solute Tempering (REST) in both explicit MeOH and water. We then used these trajectories to calculate the CD spectra for comparison with experiments and reconstruct the Boltzmann distribution to analyze the secondary structure of the peptides in solution. Unfortunately, a big obstacle was found when the employed methodology proved to disagree with the experiment in bith solvents and for all peptides (Fig. 1). For the simulation in water not only we find no agreement with the measured spectrum for the mean spectra, but also no overlap between all calculated CD spectra for all investigated configurations of the trajectories. The disagreement between simulation and experiment might be attributed to different causes: (i) the CD spectra calculations via DichroCalc might be misleading, (ii) an insufficient sampling of the energy landscape and/or convergence issues of the H-REST simulation might misrepresent the conformational ensembles, and (iii) the underlying force field might be not appropriate for these systems. For this reason, the project continued trying to investigate the role of the force field, by comparing different popular choices (amber99, amber03, charmm36) and recent extensions designed to describe intrinsically disordered proteins. Some

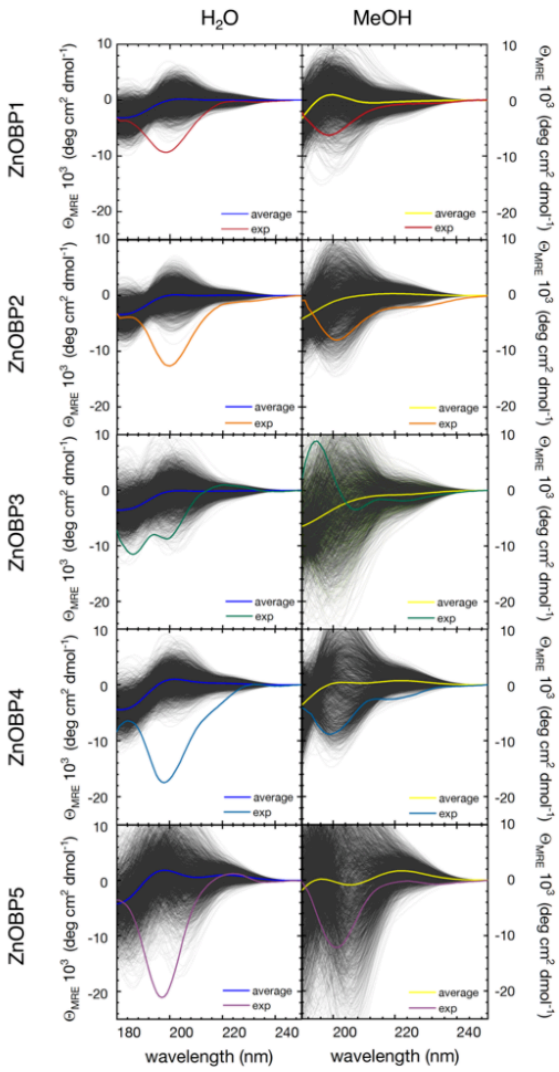

Fig 1: Calculation of CD spectra using DichroCalcfor the REST trajectories for ZnOBP1 to 5 in water and methanol. The black spectra are the spectra calculated from each snapshot of the trajectory, the blue and yellow spectra represent the averaged spectra from the trajectory for water and methanol, respectively.

improvements were found, but testing is still ongonig.

Outlook

When a reasonable choice of force field is found, reaching a good qualitative agreement with the experiment, the peptides will be simulated on two pre-prepared realistic models of the ZnO(10-10)/MeOH and the ZnO(10-10)/H2O interfaces. A modeling method based on REST in combination with Metadynamics (RESTMetaD) is employed, where the collective variable is the distance between surface and peptide, to extract and estimation of ΔG_{ads} for the five binding peptides.

hbc00025: Polymer hybrid materials – Atomistic Modelling of the Formation of a Thermo-set/Thermoplastic Interphase during Co-Curing

The scientific results obtained thanks to the allocated computational resources have been already included in the 2017 BremHLR Annual Status Report. The remaining allocated time was employed to refine and rerun some of the simulations to finalize the publication reporting the results.[1]

hbc00028: Searching for an electronic fingerprint on 2D materials

Overview

Two dimensional materials such as graphene and transition metal dichalcogenides (TMDCs) show great potential being employed in newly developed sensing devices. When integrated in liquid-gated field-effect transistors (FETs) they are able to detect small inorganic molecules such as NH_3 but also larger biomolecules like proteins or DNA. A sensing response is recorded via a shift of the Dirac voltage. This minimum of the drain current at different gate voltages marks the transition point between the *hole*-mobility-dominated and the *electron*-mobility-dominated regimes inside the conducting material. In this project we try to further investigate the 2d materials electronic response to adsorbed analyte molecules and establish a unique electronic fingerprint.

Results

An electronic fingerprint was first established by the means of dispersion corrected DFT calculations. Here the charge density difference of an adsorbed configuration (graphene slab and analyte molecule) was taken and from this setup, Bader charges were determined and assigned to each carbon atom in the graphene slab (cf. Fig. 2a). As not only small molecules can be detected by this kind of sensor, we also aimed at transferring this fingerprint to a classical setup, i.e. all-atom molecular dynamics. Here we used the GRAPPA polarizable force field, which employs a so-called rigid rod model. The polarizability is achieved by adding a *pseudo-atom* to each carbon atom's site. Here we extracted a classical adsorption fingerprint by the means of the dipole orientation (cf. Fig. 2b).

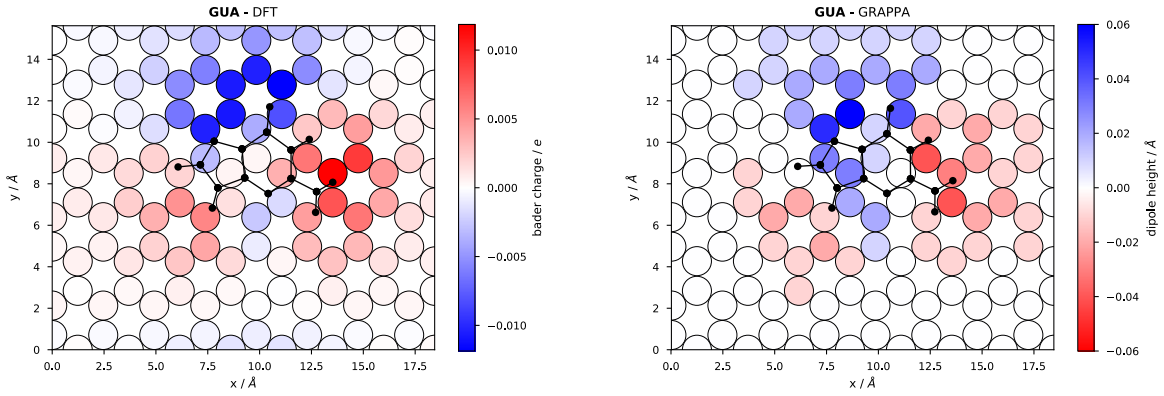

(a) (b)

Fig. 2: Guanine molecule adsorbed on graphene. (a) Electronic fingerprint derived from the charge density difference of DFT calculations. (b) Classical fingerprint derived from the dipole orientation of the GRAPPA force field.

Correlating the electronic and classical fingerprint yields a negative coeffiecient of 88% for the shown guanine system. This was also repeated for 6 different aminoacids and verified our findings with correlations throughout higher than 80%.

Outlook

Our simulations neglect two important facts, which have to be considered. First, during an experimental setup one does not observe a single molecule adsorbed to a graphene surface in vacuum. Rather the response of a *boltzman* averaged state of up to 10^{23} different configurations is measured. We want to address this fact by using advanced sampling methods (i.e REST simulations) to obtain an averaged adsorbtion fingerprint of an analyte molecule including its environment (e.g. water solvent). Using this average fingerprint, we want to address the second shortcoming: the lack of any electron transport in our setup. As a large system would be unfeasible to simulate using ab-inito transport calculations we obted for the DFTB level of theory in combination with the NEGF formalism. Here we replaced the analyte molecule's atoms by point charges. First results of a comparison between the obtained transmission coeffients encourage us in this approach (cf. Fig. 3). Reproducing the averaged fingerprint by point charges would then allow for the feasibility of conducting meaningful transport calculations for large scale systems as well as a step towards comparability with experimental setups.

PL9

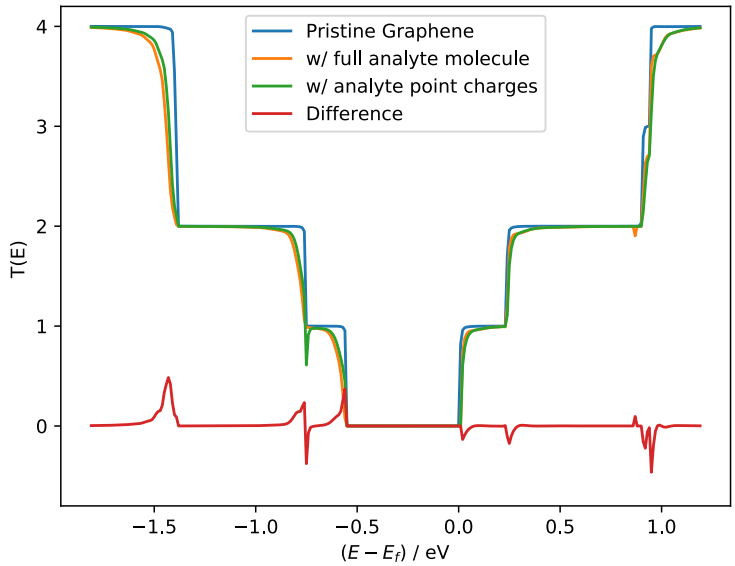

Fig. 3: Transmission curves obtained from DFTB+NEGF calculations: for a pristine graphene slab (blue), for guanine adsorbed to graphene with a full atomistic representation (orange) and for guanine adsorbed to graphene where the guanine molecule is replaced with point charges. The red line indicates the difference between the latter two.

Publications

1. M. Laurien, B. Demir, H. Büttemeyer, A. Herrmann, T. Walsh, L. Colombi Ciacchi, “Atomistic modelling of the formation of a thermoset/thermoplastic interphase during co-curing”. Submitted

Funding:

The project **hbc00023** was funded by the DFG with the project ID: CO1043/17-1 and is entitled “Adsorption von Bindungspeptiden an ZnO – Quantitatives Verständnis organisch-anorganischer Wechselwirkungen”. The project **hbc00028** is part of the RTG “Quantum Mechanical Materials Modelling (QM^3)”.

6.6 *hbi00027:* 3D Simulation of a magnetoplasmadynamic thruster with coaxial induced magnetic field

HLRN Project ID:	hbi00027
Run time:	IV/2015 – IV/2018
Project Leader:	PD Dr.-Ing. habil. Rodion Groll
Project Scientists:	Charles Chelem Mayigué, M. Sc.
Affiliation:	ZARM – Center of Applied Space Technology and Microgravity

Overview

The magnetoplasmadynamic (MPD) arcjet is a promising thruster which is developed for exploration missions to the moon and Mars, and for raising orbits of large space structures. The MPD arcjet utilizes mainly electromagnetic force, i.e, Lorentz force, which is generated in this work by interaction between the current density and a coaxial magnetic field azimuthally induced by the total discharge current. In the present work, we developed and used a density-based method associated with a divergence cleaning technique for the simulation of the MPD thrusters under a finite volume formulation. This new algorithm was developed for the single resistive MHD equations and make use of the central-upwind scheme of Kurganov and Tadmor for flux calculation. Electrical conductivity for fully ionized plasma and viscosity are predicted according to the Spitzer-Härm formulation and the Sutherland thermophysical model respectively. The perfect gas equation of state is also considered.

Introduction and motivation

Despite the advances in combustion research, the highest exhaust velocity of a functional chemical propulsion system, 3.600 to 4.500 m/s from sea level to high altitude, is still inadequate for most deep-space missions of interest. The present situation of space exploration calls for missions beyond the moon and for such missions, chemical propulsion is not a viable option, except for the case of launch vehicles where high thrust is required. Functionally, the inability of chemical propulsion systems to achieve higher exhaust velocities is due to limitation in the maximum tolerable temperature in the combustion chamber and to avoid excessive heat transfer to the walls. Both these limitations can be overcome by use of electric propulsion, which can be defined as the acceleration of gases for propulsion by electrical heating and/or by electric and magnetic volume forces. The magnetoplasmadynamic (MPD) thrusters have the unique capability, among all other developed electric propulsion systems, of processing megawatt power levels in a simple, small and robust device, producing thrust densities as high as 100 thousand N/m². These features render it an attractive option for high energy deep space missions requiring higher thrust levels than other electric thrusters. In its basic form, the MPD thruster consists of a cylindrical cathode surrounded by a concentric anode (Figure 1). An electric arc between the electrodes ionizes a gaseous propellant, and the interaction of the current with the self-induced magnetic field accelerates the plasma to produce thrust. The specific impulse of a self-field MPD thruster is related to the parameter I^2/m which is often used to characterize MPD thruster performance with I the discharge current and m the mass flow rate. High values of I^2/m correspond to predominantly electromagnetic acceleration, and provide higher values of specific impulse. Low values of I^2/m correspond to predominantly electrothermal

acceleration, and lower values of specific impulse. MPD efficiency typically increases with increasing I^2/m, but this also leads to strong numerical instabilities (the onset phenomena), which makes the solvers unstable and undermines its value. For modeling of the thruster, CFD code is required to understand the complex nature of the coupled electromagnetic and gas dynamic acceleration processes and the effects of relevant flow-field parameters which are otherwise quite hard to analyse with experiments. With the emergence of high-speed computational facilities, CFD code permits model validation using the existing experimental data base. Thus, the ultimate goals of the present project are: Use the developed density-based code to simulate the MPD thrusters in the purpose to obtain insight into the physics of thrust performance and energy dissipation in these devices and also obtain operating conditions and geometrical configurations of a specific type of thruster for which the solver is stable.

Results

A limited set of computer runs were performed to access the effect of geometric scale changes on self-field MPD thruster performance. The first geometry set (MPDT01) consisted of a 0.0095 m radius cathode with 0.264 m length, surrounded by a 0.025 m radius anode. The second set (MPDT02) doubled the anode radius to 0.051 m, but kept the cathode radius at 0.0095 m. The third set (MPDT03) kept the anode radius at 0.051 m, but increased the cathode radius to 0.0181 m. The last set (MPDT04) has the same parameter than MPDT02, but reduce the cathode length to 13.2 cm. For each combination of radii, the anode lengths are scaled from 1 to 5 times the anodes radius (aspect ratio). The argon propellant mass flow rate was kept constant at 6 g/s, and was assumed to be fully ionized for all cases. The five I^2/m values, ranging from 05×10^9 A²s/kg to 62×10^9A²s/kg are evaluated for each geometry. Results of the numerical simulations for MPDT01 are presented below. MPDT01 thruster was not able to converge for aspect ratio la/ra=1. Convergence was obtained for all the I^2/m values with $l_a/r_a > 1$. Thrust and plasma voltage increase with increasing I^2/m (Fig.1). The transition from electrothermal acceleration mode to electromagnetic acceleration mode occur at I^2/m around 18 which correspond to a discharge current value of 10 kA (critical current). The effect of this transition on the MPDT01 thruster performance is well illustrated on Efficiency profil (Fig. 1) which decreases by the electrothermal acceleration mode and starts to increase from the critical current when the electromagnetic thrust becomes dominant. Fig. 2 presents the main flow variables distribution inside and outside the thruster for two different values of I^2/m 18.7 and 62. These results are almost similar for the two other geometry configurations MPDT02 and MPDT03 with different stability range and different critical current value. But most generally, the simulation point out the fact that, at lower I^2/m, thruster operation require larger aspect ratio with shorter cathode length for more stability. For equivalent I^2/m value, small aspect ratio thrusters are required to improve the thruster flow efficiency.

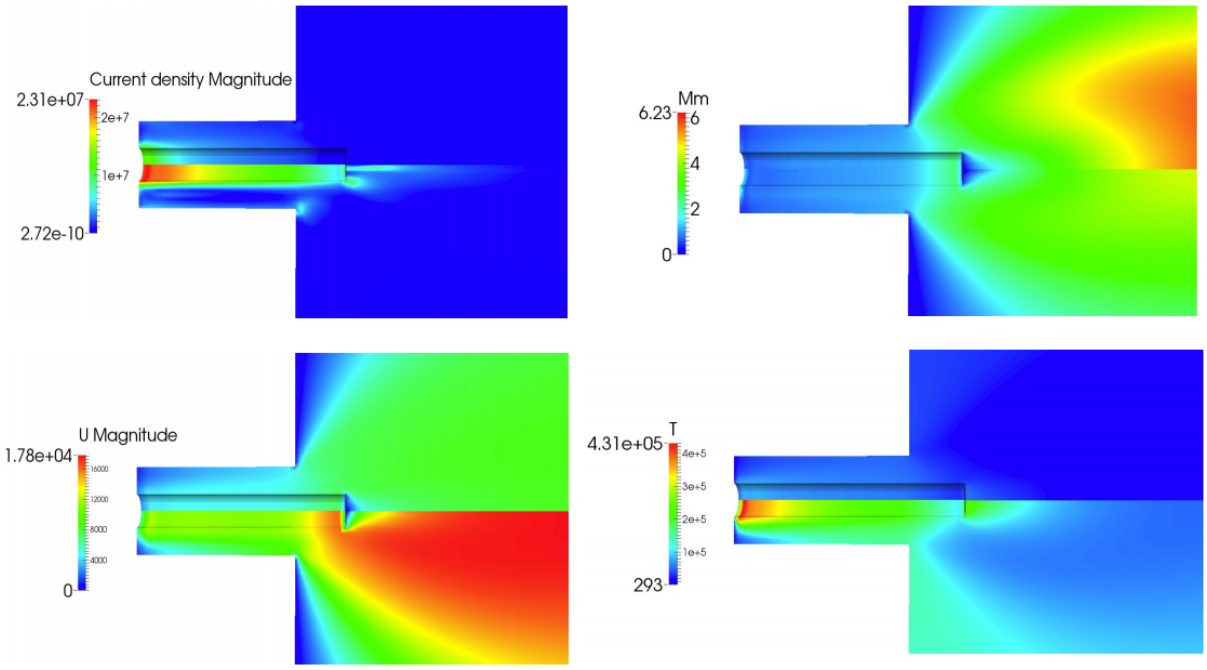

Fig. 1: Distribution of current density (Ji) [A/m²], magnetic Mach number (Mm), velocity (U) [m/s] and temperature (T) [K] and for MPDT01 with shorter cathode, 6 g/s mass flow rate and 04 aspect ratio. For each picture, *I²/m=18.7*(top) ***and I²/m***=*62*(bottom)

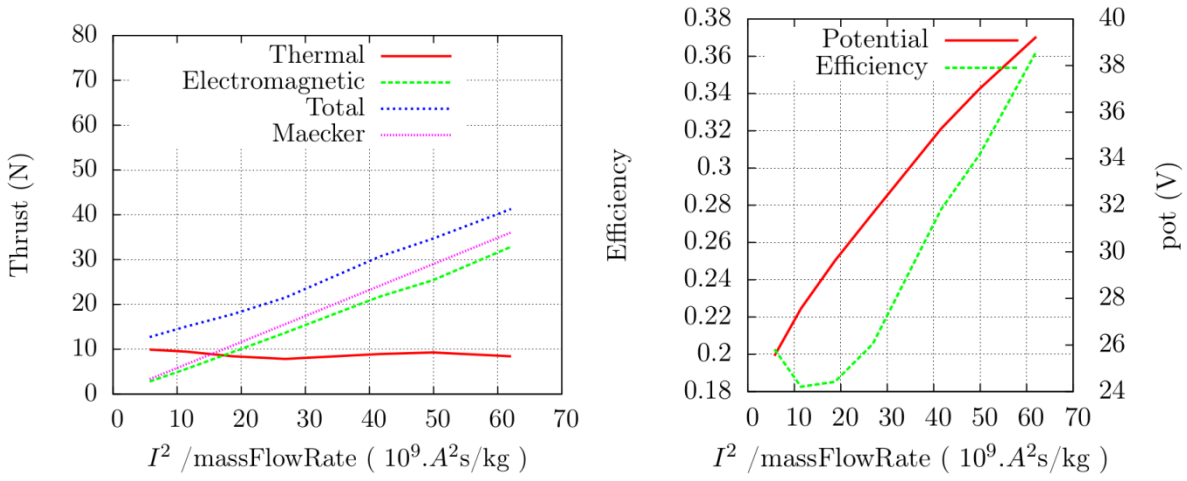

Fig. 2: Thrust [N] (left), Efficiency and plasma voltage (right) for MPDT01 with shorter cathode.

Outlook

The results obtained in this project indicate that the semi-discrete density-based central-upwind solver is able to deal with plasma flow simulation in MPD thrusters and therefore will be helpful for their development and designing. However, the code remains unstable by high I^2/m values. Thus, the improvement of the physical model will be an important topic for near future work.

Publications

1. *C. Chelem Mayigué, R. Groll, "A density-based method with semi-discrete central-upwind schemes for ideal magnetohydrodynamics", Arch. Appl. Mech. (2016) doi :10.1007/s00419-016-1216-7.*

2. *C. Chelem Mayigué, R. Groll, "Magneto-Plasmadynamic Thruster modelling with coaxial induced magnetic field", Int. J. Comp. Meth. and Exp. Meas., Vol. 4, No.4 (2016) 380–392.*

3. *C. Chelem Mayigué, R. Groll., "Numerical simulation of Argon fuelled self-field magnetoplasmadynamic thrusters using the central-upwind scheme flux interpolation", European Journal of Machanics / B Fluids 72 (2018) 645-663. https://doi.org/10.1016/j.euromechflu.2018.07.010.*

Presentations

1. C. Chelem Mayigue, R. Groll: 11th International Conference on Advances in Fluid Mechanics in Ancona (Italy), 5-7/09/2016.
2. C. Chelem Mayigue, R. Groll: 4th Northern germany OpenFoam User meetiNg (NOFUN) 2016, Braunschweig, Germany, 29/09/2016.

Acknowledgement

This work is funded by the *Deutscher Akademischer Austauschdienst* (DAAD) through the "Research grants for doctoral candidates and young academics and scientists" programme (grant number 57076385).

References

1. R. G. Jahn, E. Y. Choueiri, *Electric propulsion*, Academic Press Encyclopedia of Physical Science & Technology (2000) 1–17.
2. K. Sankaran, *Simulation of mpd flows using a flux-limited numerical method for the mhd equations*, Ph.D. thesis, Princeton University, Technology and Medicine, Princeton (2005).
3. A. Kurganov, S. Noelle, G. Petrova, Semi-discrete central-upwind schemes for hyperbolic conservation laws and hamilton-jacobi equations, SIAM Journal on Scientific Computations 23 (2001) 707–740.
4. C. J. Greenshields, H. G. Weller, L. Gasparini, J. M. Reese, Implementation of semi-discrete, non-staggered central schemes in a collocated, polyhedral, finite volume framework, for high-speed viscous flows, International journal for numerical methods in fluids 63 (2010) 1–21.

6.7 *hbi00030:* Investigation of performance of an argon fueled magnetoplasmadynamic thruster with applied magnetic fields

HLRN Project ID:	hbi00030
Run time:	II/2016 – I/2018
Project Leader:	PD Dr.-Ing. habil. Rodion Groll
Project Scientists:	Charles Chelem Mayigué, M. Sc.
Affiliation:	ZARM – Center of Applied Space Technology and Microgravity

Overview

The applied-field magnetoplasmadynamic thrusters (AF-MPDT) are the promising technology for space missions requiring high specific impulse, high thrust density with low on board electric power. In this device, the plasma is accelerated by combining the gas dynamic and the electromagnetic processes. In the present project, the numerical modeling of AF-MPDT is performed using a electromagnetic code to produce external magnetic field and the density-based code, developed in the on going MagJet project, to deal with magnetohydrodynamic (MHD) equations. The magnetic field is axially applied by an external coil surrounding the anode which interacts with the discharge current and the induced azimuthal current to produced thrust. We make used of the Spitzer-Härm formulation for the calculation of electrical conductivity as the plasma in this work is considered fully ionized.

Introduction and motivation

In the electric propulsion systems group, we have the magnetoplasmadynamic thrusters (MPDT), which is classified into two categories; Self-field MPDT (SFMPDT) and applied-field MPDT (AFMPDT). In SFMPDT, the main acceleration mechanism is represented by the interaction between the discharge current and the self-induced magnetic field. That means, high trust level can be obtained only for high discharge current (5-100 kA) and consequently for high power (MWs). Contrary to SFMPDT, the AFMPDT, introduce new acceleration mechanisms that do not directly depend on the discharge current and thus can allow the thruster to effectively operate at lower powers. At all, four acceleration mechanisms have been identified. The relative importance of each depends upon thruster design and operating conditions (current, mass flow rate, applied field strength). The four mechanisms are: Gas dynamic acceleration mechanism: this mode contains the joule heating and the expansion of the plasma through physical and/or magnetic nozzle. Self-field acceleration mechanism: Interaction of discharge current arc and self-induced azimuthal magnetic field lead to axial and radial acceleration. Swirl acceleration mechanism: Interaction of discharge current and applied magnetic fields results in azimuthal force that puts plasma into rotation. The rotation energy can be partly converted to axial acceleration downstream. Hall acceleration mechanism: Interaction of induced azimuthal current (Hall current) and applied magnetic field produces axial and radial lorentz forces.

Other advantages in adopting an AFMPDT is the extension of a significant fraction of the current downstream of the thruster geometry particularly on the pic of the cathode. For the thruster modeling, CFD code is required to understand the complex nature of the coupled electromagnetic and gasdynamic acceleration processes and the effects of relevant flow-field parameters which are otherwise quite hard to analyse with experiments. With the emergence

of high-speed computational facilities, CFD code permits model validation using the existing experimental data base. The main goals of the Applied-MhdJet project are: Optimize the thruster and electrode geometry and particularly the configuration of the applied magnetic field of an AFMPDT. Investigate the influence of externally-applied magnetic fields strength and discharge current on the thruster efficiency. Better understanding of all propellant acceleration mechanisms. The achievement of acceptable thruster performance, especially in terms of thrust efficiency.

Results

A limited set of computer runs were performed to access the effect of external magnetic strength and mass flow rate of Argon on the NASALeRC MPD thruster performance (see Tab.1). For the purpose of comparison of our results with previous study, we decided to change the former geometry with the applied field NASA Lewis Research Center's (NASALeRC) MPD thruster geometry, which in contrary to the Villani-H thruster was typically investigated for applied-field code with a wide range of experimental data. For the same reason, we also decide to replace the geometric scaling analysis based on the ratio of anode over cathode radius by the variation of the mass flow rate of argon which ranging from 0.06 g/s to 0.2 g/s. Thus, the configuration considered (AFMPDT01) consisted of a cathode with 1.27 cm radius, surrounded by an anode with 5.1 cm radius both are 7.6 cm long. For the AFMPDT01 configuration, the magnet coil that provide the applied magnetic field is 15.3 cm long with a 10.15 cm radius. To avoid the creation in the discharge chamber of two magnetic force pointing in opposite direction, the magnet is placed with one end coinciding with the exit plane of the thruster. The second configuration we considered in this work named AFMPDT02, maintains the same geometric dimensions of AFMPDT01 but here, two magnet coils with a 10.15 cm radius have been used instead of one. the first magnet is 11.72 cm long and it is placed one end at 1.6 cm downstream of the inlet. The second one is 3.4 cm long with one end at the thruster exit. For each value of mass flow rate, the discharge current strength are scaled form 750 A to 2000 A. The five values of the applied magnetic field strength was varied from 0.012 T to 0.08 T, as measured at the cathode tip. The most challenging results of the numerical simulations with AFMPDT01 realised at this stage of the project are presented bellow.

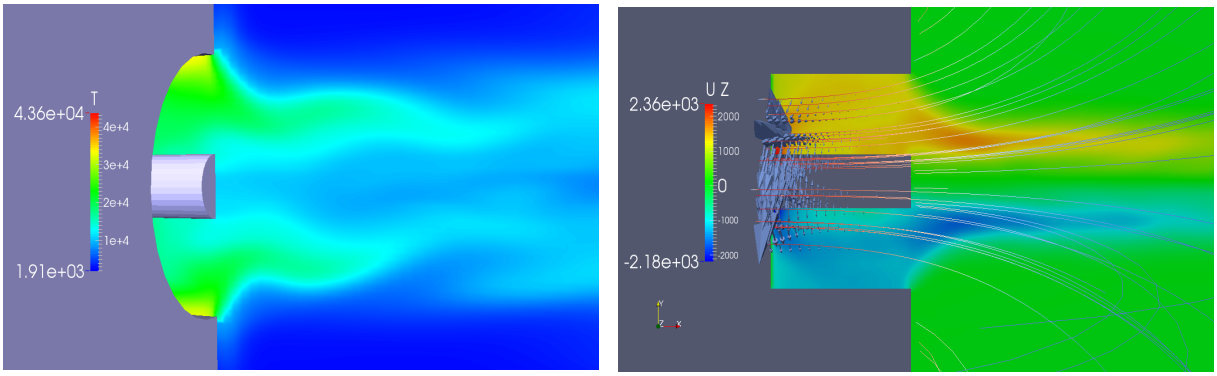

Fig. 1: Temperature distribution (T) [K] outside the discharge chamber (left) and Rotational speed (Uz) [m/s] including applied magnetic field line and induced magnetic field vector (right).

The main effect of the application of an axial magnetic field is to put the plasma in rotation inside the discharge chamber of the MPD thruster. Here, for a constant value of applied magnetic field strength, the swirl to self thrust ratio decreases by increasing the current (see Fig. 2). In the other hand for each current value, this ratio increases by increasing the applied

magnetic field. Thus, for the case of consideration, it appeared that the swirl component of thrust is dominant and is mostly responsible of the acceleration of the plasma out of the thruster.

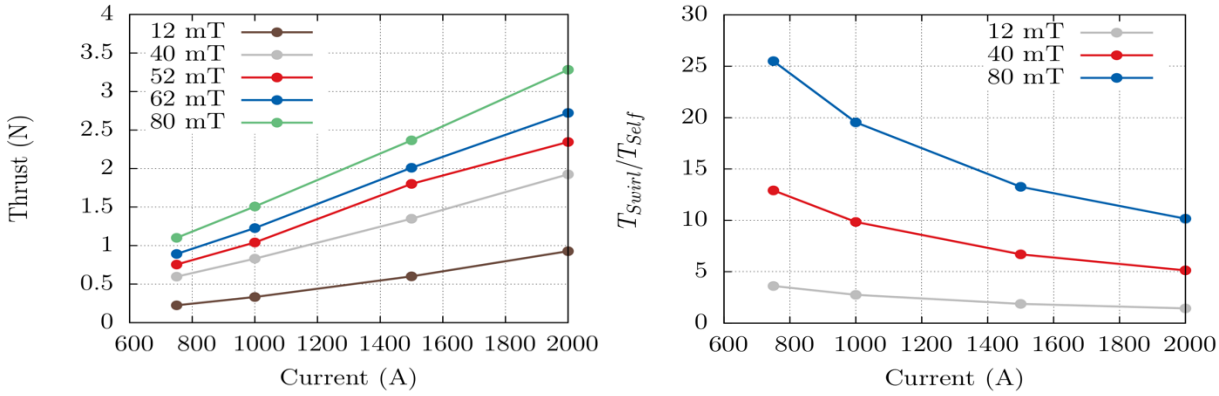

Fig. 2: Thrust [N] (left) and the ratio of swirl over self component of thrust (right) function of discharge current.

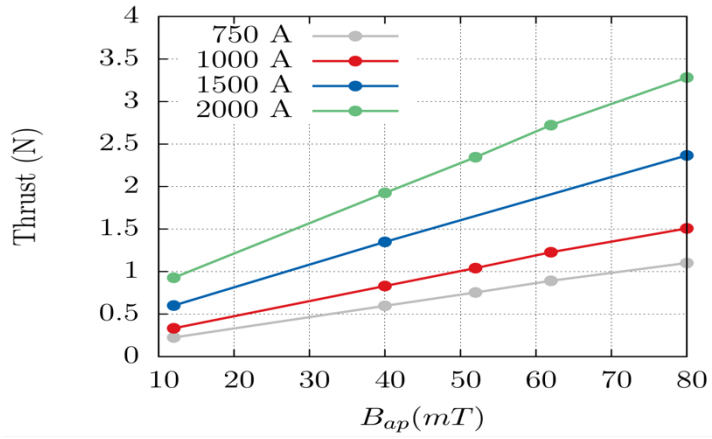

Fig. 3: Thrust [N] function of applied magnetic field strength.

Outside the MPD thruster, the acceleration is based on the conversion of the above mentioned rotational energy via expansion in a magnetic nozzle which is formed by the diverge magnetic field lines. The induced azimuthal currents interact with the applied magnetic field to produce a radially confining electromagnetic force. Fig.3 presents thrust variation function of the applied magnetic field and discharge current. The code reproduced the increase of thrust for both case as predicted by some previous modelling and analytic works.

Outlook

In this project, we successfully used the developed density-based code for the simulations of the applied-field NASALeRC MPD thruster and the method presents ability to reproduce the theory of thrust production and plasma acceleration. For that we used a configuration with one external magnet and investigated the effect of applied magnetic strength and discharge

current on the thruster performance. For the near future work it is planned to investigated the configuration (AFMPDT02) with two external magnets surrounding the discharge chamber in order to obtain a quasi uniform and horizontal applied field distribution near the anode to improve the thrust production as the swirl acceleration appeared as the most important component of thrust.

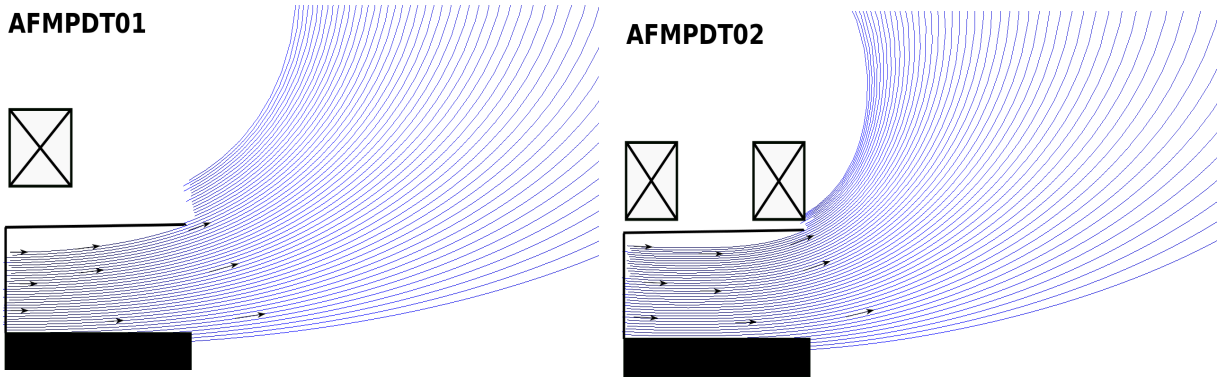

Fig. 4: Applied-field MPD thruster configurations considered in this project: one (left) and two (right) external magnet(s).

Publication

C. Chelem Mayigue, R. Groll, "*Performance investigation of an argon fueled magnetoplasmadynamic thruster with applied magnetic fields",* Journal of Applied Physics 124, 223301 (2018). https://doi.org/10.1063/1.5038421.

Acknowledgement

This work is funded by the *Deutscher Akademischer Austauschdienst* (DAAD) through the "Research grants for doctoral candidates and young academics and scientists" programme (grant number 57076385).

References

1. G. Krülle, M. Auweter-Kurtz, A. Sasoh, *Technology and application 335 aspects of applied field magnetoplasmadynamic propulsion*, Journal of Propulsion and Power 14 (5) (1998) 754–763. doi:10.2514/2.5338.

2. G. P. Mikellides, J. P. Turchi, F. N. Roderick, Applied-field magnetoplasmadynamic thrusters, part 1: Numerical simulations using the mach2 code, Journal of propulsion and power 16 (2000) 887–893. doi:10.2514/2.5656.

3. R. Albertoni, F. Paganucci, M. Andrenucci, A phenomenological performance model for applied-field mpd thrusters, Acta Astronautica 107 (2015) 177–186. doi.:10.1016/j.actaastro.2014.11.017

6.8 *hbi00033:* Flow transitions and regimes in core-annular pipe flow

HLRNProject ID:	hbi00033
Run time:	1/2016 – 03/2019
Project Leader:	Prof. Dr. Marc Avila
Project Scientists:	C. Plana, Dr. B. Song.
Affiliation:	Center of Applied Space Technology and Microgravity (ZARM) Universität Bremen

Overview

Core-annular pipe flow (CAF) has applications in transporting highly viscous fluids, such as crude oil in pipelines, as well as in microuidic flows. However, the perfect core-annular flow is in general linearly unstable and can exhibit multiple ow configurations, such as bamboo waves, slug flow, bubble flow, and oil in water dispersion, as a function of the operating conditions. The core-annular flow has been investigated widely, mainly in experiments, and some rather crude phase-diagram was given in terms of dimensional parameters, such as the nominal water flow rate and oil flow rate. For generality, the phase-diagram in terms of non-dimensional control parameters (e.g., Reynolds number) is highly desired for applications to different experimental setups and flow conditions, and for in-depth theoretical investigation on the bifurcation leading to different flow patterns. This project aims to probe the phase-diagram of core-annular pipe flow using direct numerical simulation (DNS) of the Navier-Stokes equations together with the Cahn-Hilliard equation that allows to naturally capture the interface in the binary fluid system.

Results

During last year, a large amount work was done in our paper on the simulation of CAF using the phase-field method [1], including an extended study of the convergence and linear stability analysis of the laminar CAF (see fig. 1). The paper demonstrates the ability of the phase-field method to accurately deal with non-Cartesian geometry, strong advection, unsteady fluctuations and large viscosity contrast. If focus on quantitative results, with a good agreement with literature. It is currently under review at the International Journal of Multiphase Flows.

During the first phase of 2018 we focused in the study of the slug flow formation. This configuration is characterized by the break-up of the core-annular arragement, with individual oil structures flowing separated by water regions. During slug flow, the more viscous oil touches the pipe wall and the viscous loses increase dramatically. Therfore, understanding the transition to the slug flow regime is crucial to avoid its formation in practical applications.

In contrast with the previous phase, where we studied the bamboo-wave regime using a large viscosity ratio mixture, here we focused in a combination of fluids with a milder viscosity and density ratio ($\hat{\rho} = 1, \hat{\mu} = 3$), in order to reduce the computational costs, due to the large grids and small time step sizes required to keep the error low when the large viscosity ratios are used. Figure [2] shows an example of the slug formation process. The laminar core-annular structure starts to deform until it eventually breaks up and the individual slugs could be observed.

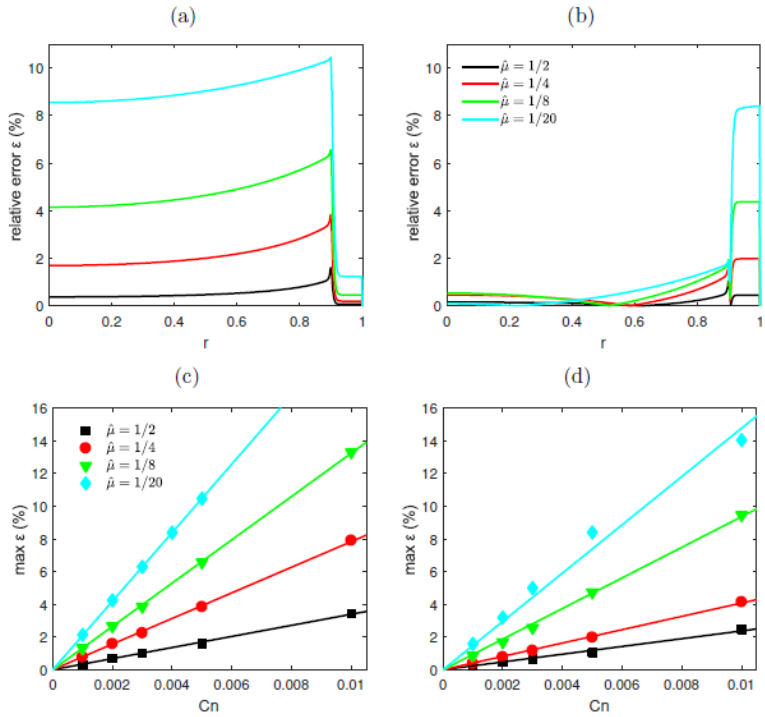

Fig. 1: Convergence study of phase-field CAF to analytical solution. a) relative error of pressure-driven flow. b) relative error of volume flux-driven flow. c) convergence of pressure-driven flow. d) convergence of volume flux-driven flow.

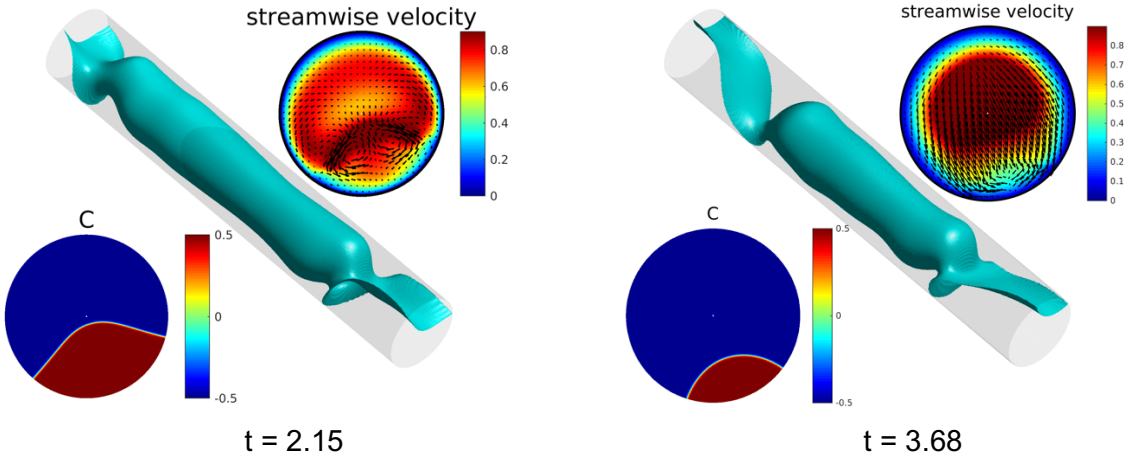

Fig. 2: Slug formation simulations. Left: Phase-field variable. Center: Interface (C =0). Right: In-plane velocity (arrows) + streamwise velocity (colormap)

In the second phase, we concentrated in the study of the transition to turbulence of core-annular flow at moderate Re. We used a mixture of kerosene and water for this problem, since it is widely used in the literature and presents a moderate viscosity and density ratios ($\hat{\rho} = 0.79, \hat{\mu} = 1.6$). Starting with laminar CAF, we perturbed the flow and let it evolve. We studied the linear instabilities and transition regions in the regimes (Re = 3000-12000) (see fig. [3]). However, the cost of simulating the saturation in the nonlinear regime was larger than expected for such high values of Re.

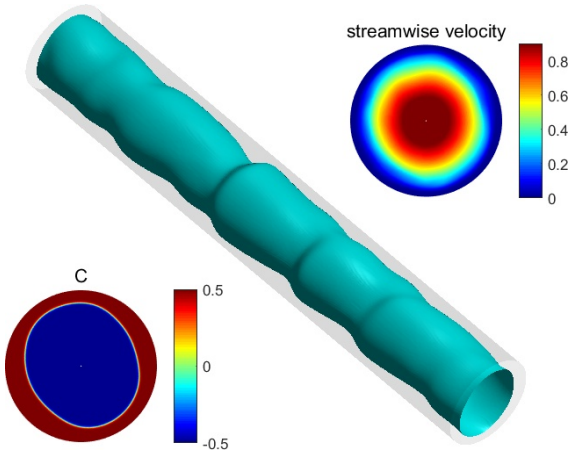

Fig. 3: Transition to turbulence in water/kerosene CAF at Re = 6000.Left: Phase-field variable. Center: Interface (C =0). Right: In-plane velocity (arrows) + streamwise velocity (colormap)

Outlook

We are currently focusing on the study of the transition to turbulence of CAF at low to moderate Re (Re = 500 – 3000). Additionally, we plan to improve the parallelization of our code, in order to increase its efficiency when using the hybrid approach. This will allow us to increase the speed-up and study the non-linear saturation at higher Re and work further into the slug-formation regime.

Publications

1. B. Song, C. Plana, J.M. Lopez, M. Avila, Phase-field simulation of core-annular pipe flow, International Journal of Multiphase Flow, *Under Review*

Presentations

1. C. Plana, B. Song, M. Avila, 12th EFMC, TU Wien, September 12, 2017

6.9 *hbi00036:* Fluiddynamische Untersuchung der Stressbeanspruchungen proteinstabilisierter o/w-Phasengrenzflächen beim Premix-Membranemulgieren

HLRN-Projektkennung:	hbi00036
Laufzeit:	II/2018 – II/2019
Projektleiter:	Prof. Dr.-Ing. Udo Fritsching
Projektbearbeiter.	Laura Luhede
Institut / Einrichtung:	Particles and Process Engineering, Universität Bremen

Überblick

Emulgierverfahren werden im Rahmen des Downstream-Prozessierens und der Weiterverarbeitung/Formulierung zur Homogenisierung oder auch Verkapselung in biogenen Produkten eingesetzt. Beim Premix-Emulgieren wird eine grobdisperse Voremulsion mittels der Dispergierung in porösen Membranen in eine Feinemulsion bzw -Dispersion überführt. Insbesondere das Stress-Verweilzeitverhalten und die darauf erfolgende Reaktion eines protein-stabilisierten dispersen Systems bedarf einer vertieften wissenschaftlichen Klärung. Hieraus können mechanistische Schädigungsmodelle abgeleitet werden. Die im Emulgier-Prozess auftretenden mikromechanischen Belastungen auf biologische Systeme sind nicht vollständig geklärt, die Prozessumgebung ist somit noch weiter zu entwickeln im Hinblick auf die Anpassung an spezielle biologische Systeme.

Der Fokus dieses Forschungsvorhabens liegt auf der Beschreibung des mehrphasigen fluiddynamischen Prozesses beim Premix-Emulgieren in porösen Strukturen. Es wurde ein Modell zur Beschreibung von Scher- und Dehnkräften an der Phasengrenze entwickelt und in die Open Source Software OpenFOAM implementiert. Dieses Modell wurde in idealisierten Strukturen sowie komplexen, porösen Geometrien verwendet. Der Einfluss von Scher- und Dehnkräften auf die Grenzfläche ist von besonderem Interesse für die Untersuchung von Tropfenaufbruchskriterien beim Premix-Emulgieren, sowie zur Bestimmung der dabei entstehenden Belastung der an Phasengrenzen adsorbierten Proteine. Ziel des Projekts ist es die Kriterien für Tropfendeformation und –Aufbruch zu ermitteln und anhand der Belastungen auf die Grenzfläche zu quantifizieren.

Ergebnisse

Es wurde ein Modell zur Beschreibung von Scher- und Dehnkräften an der Phasengrenze entwickelt. Die Validierung erfolgte an einer mehrphasigen Couette Strömung. Die Berechnung der auf die Grenzfläche wirkenden Kräfte wurden dazu mit der analytischen Lösung sowie experimentellen Daten verglichen.

Komplexere Systeme wurden behandelt, indem das Scher-Stress-Verweilzeitverhalten von Tropfen in verschiedenen idealisierten Porenstrukturen untersucht wurde. Im Folgenden wird das Verweilzeitverhalten anhand einer Verengung von einer großen Kapillare in eine kleinere dargestellt. Das vorliegende Gitter hat eine Zellanzahl von 1,6 Mio. Zellen mit einer mittleren Kantenlänge von 8 µm. Eine Gitterunabhängigkeit wurde für Zellgrößen von 8 – 10 µm Kantenlänge nachgewiesen. Das System ist massenkonservativ. Exemplarisch ist in Abb. 1 die Tropfendeformation bei verschiedenen Kapillarzahlen Ca zu sehen. Bei der kleinsten Kapillarzahl Ca = 0,181 (a) strömt der Tropfen, ähnlich wie bei einer Pfropfenströmung,

immer mit direktem Wandkontakt durch die Pore. Der Tropfen bleibt nach dem Poreneintritt in einer quasi-stationären Form. Hoher Scherstress findet an der Tropfengrenzfläche die sich in Kontakt mit der Porenwand befindet statt, während der Scherstress an der freien Grenzfläche vergleichsweise gering ist. Das Maximum befindet sich als schmaler Ring am unteren Ende des Tropfens beim Übergang zwischen der Porenwand und der freien Grenzfläche. Bei steigender Kapillarzahl (b) löst sich der Tropfen partiell von der Wand. Die Kontaktlinie zur Wand verschiebt sich dabei mit den Zeitschritten, da ein immer größer werdender Teil von der Wand abgelöst wird. Auch hier ist der höchste Scherstress an der liquid-solid Grenzfläche zu finden, während der Stress an der liquid-liquid Grenzfläche geringer bleibt. Steigt die Kapillarzahl weiter an (c) kommt zu einer noch schnelleren Tropfenablösung von der Wand, gefolgt von einer Einschnürung. Dies zeigt, dass der von der Wand gelöste Teil schnellere lokale Geschwindigkeiten aufweist, als der an der Wand vorhandene Teil. Mit zunehmender Residenzzeit führt diese Einschnürung zum Tropfenaufbruch. Die Lippe am Ende des Tropfens kann durch Unebenheiten im Ablöseprozess entstehen, sowie Instabilitäten in dem Fortschreiten der Kontaktlinie. Generell können aus den Ergebnissen stressbezogene Trends für die Tropfendeformation sowie den Tropfenaufbruch ermittelt werden: (1) Der Aufbruchsprozess kann durch die Wandablösung bedingte Instabilitäten in der Kontaktline ausgelöst werden; (2) der abgelöste Teil wird durch Scher und Dehnkräfte deformiert und (3) der Aufbruch ist bei lokalen Einschränkungen ähnlich den Vorgängen beim Jetting.

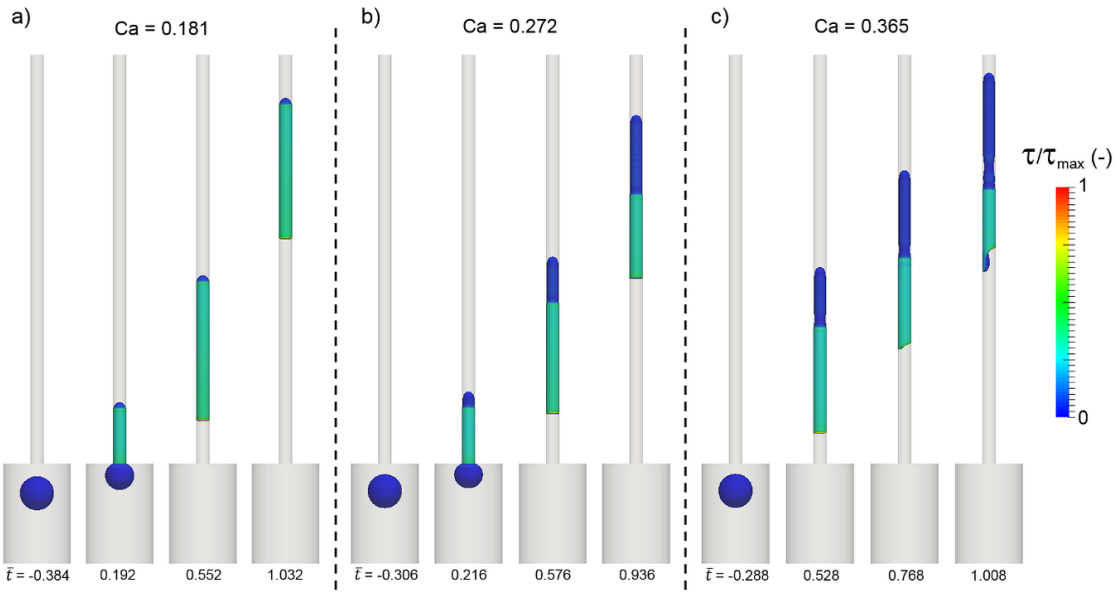

Abb. 1: Simulation von Einzeltropfen in einer Pore (d/dpore = 2,5 mm) für verschiedene Ca Zahlen und Zeitschritte t. Die Farbe zeigt qualitativ den an der Phasengrenzfläche vorhandenen Scherstress τ/τ_{max}, aus (Wollborn et al., 2019).

Die qualitativen Ergebnisse zeigen, dass eine Einteilung in Grenzflächenstress im Fluid und Stress an der Wand sinnvoll für die quantitative Analyse der Ergebnisse ist. Das Scher-Verweilzeitverhalten eines 500 µm großen Tropfens wird in Abb. 2 für verschiedene Ca-Zahlen gezeigt. An der fluiden Phasengrenze (a-c) ist eine breite Verteilung des Scherstresses über drei Größenordnungen zu sehen, welche sich mit steigendem Zeitschritt zu höherem Stress verschiebt. Bei Poreneintritt ist nur ein Teil des Tropfens in der Verengung, während sich der Rest noch frei vor der Pore befindet und kaum Schereinwirkung erfährt. Erst nachdem der Tropfen vollständig im Porenkanal eingetroffen

ist wirkt höherer Scherstress auf die Phasengrenze. Bei niedrigen Kapillarzahlen (a) wird eine stabile Verteilung des Scherstresses erreicht. Ein ähnliches Ergebnis wird auch für (b) beobachtet, wobei hier auch nach vollständigen Tropfeneintritt in den Porenkanal noch ein Versatz in der Verteilung zu beobachten ist. Dieser zeigt den Ablöseprozess, der schon in Abb. 1 beschrieben wurde. Für noch höhere Kapillarzahlen (c) wird keine stabile Verteilung des Scherstresses mehr in der beobachteten Zeit erreicht, da hier Tropfendeformation und Tropfenaufbruch auftreten. Dies zeigt, dass Tropfenaufbruch und Tropfendeformation mit dem Scherstressverhalten in Verbindung stehen.

Im Vergleich dazu zeigt der Wandscherstress (d-f) eine sehr enge Verteilung mit keinen signifikanten Änderungen über die Verweilzeit für alle untersuchten Kapillarzahlen. Daraus lässt sich ableiten, dass trotz der hohen Stressbelastung der der Wandscherstress keinen besonderen Einfluss auf Tropfendeformations- und Aufbruchsphänomene hat, sondern die Stressverteilungen an der fluiden Phasengrenze dominant sind.

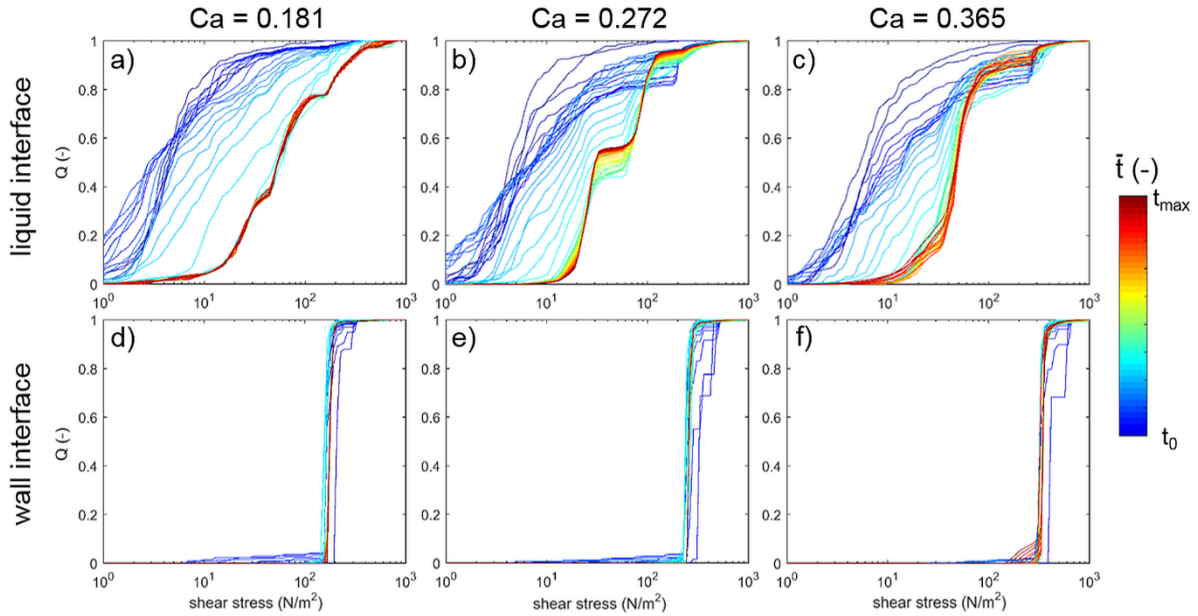

Abb. 2: Kumulative Verteilung des Grenzflächenstresses im Fluid und an der Wand, aus (Wollborn et al., 2019).

Diese Ergebnisse wurden im Detail in (Wollborn et al., 2019) veröffentlicht. Eine weitere Veröffentlichung zur genaueren Beschreibung des Tropfenaufbruchs befindet sich gerade in Arbeit und wird demnächst veröffentlicht. Neben den Ergebnissen zu Modellstrukturen wurden auch Simulationen in komplexen Geometrien durchgeführt (Abb. 3). Diese zeigen den Tropfenaufbruch in einer Membran. Weiterführende Simulationen zur genauen Auswertung und Einordnung der Ergebnisse sind nötig.

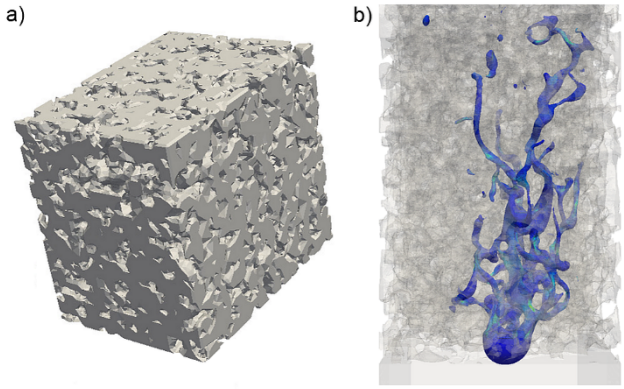

Abb. 3: CT-Scan einer gesinterten Glasmembran (P2, ROBU) und simulierte Tropfenverteilung in der Membranstruktur, aus (Wollborn et al., 2019).

Ausblick

In der neuen Förderperiode werden weitere Parameter und Geometrien im Bereich Modellstruktur untersucht. Insbesondere bei hohen Kapillarzahlen sind Effekte zu beobachten, die zu einer Dispergierung der kontinuierlichen Phasen innerhalb des Einzeltropfens führen. Diese sollen nun genauer untersucht werden. Dadurch können weitere Einflüsse auf den Tropfenaufbruch und das Scherstress-Verweilzeitverhalten in einer definierten Porenstruktur ermittelt werden.

Bei Emulgierexperimenten wurde Tropfenaufbruch aber auch bei geringen Kapillarzahlen beobachtet, welcher in den bisher untersuchten Modellstrukturen bisher nicht gezeigt werden konnte. Der Aufbruch erfolgt in dem Fall durch Verzweigungen und Änderung der Geschwindigkeitsfelder durch wechselnde Porengrößen. Dies soll mit neuen Modellstrukturen abgebildet werden. Die Stressbelastung an einer Verzweigung sowie einer Pore mit einem Durchmesser vielfach der Tropfengrößen werden untersucht. Dabei werden neben den Kapillarzahlen auch die Kontaktwinkel und Viskositätsverhältnisse variiert.

Publikationen

1. Wollborn, T., Luhede, L., & Fritsching, Evaluating interfacial shear and strain stress during droplet deformation in micro-pores. *Phys. Fluids*, *31*, 012109 (2019) https://doi.org/10.1063/1.5064858

Vorträge / Poster

1. Tobias Wollborn, Laura Luhede, Udo Fritsching, Numerical modeling and simulation of interface stress and deformation of droplets in liquid-liquid flow through constrictions, ProcessNet Jahrestagung und 33. DECHEMA-Jahrestagung der Biotechnologen 2018, Aachen, Deutschland, 10.-13.09.2018 (Poster)

6.10 *hbi00037:* Molekulardynamische Untersuchung der Stressbeanspruchungen auf Proteine an der Phasengrenzfläche beim Premix-Membranemulgieren

HLRN-Projektkennung:	hbi00037
Laufzeit:	II/2018 – II/2019
Projektleiter:	Prof. Dr.-Ing. Udo Fritsching
Projektbearbeiter.	Tobias Wollborn
Institut / Einrichtung:	Particles and Process Engineering, Universität Bremen

Überblick

Emulgierverfahren werden im Rahmen des Downstream-Prozessierens und der Weiterverarbeitung/Formulierung zur Homogenisierung oder auch Verkapselung in biogenen Produkten eingesetzt. Beim Premix-Emulgieren wird eine grobdisperse Voremulsion mittels der Dispergierung in porösen Membranen in eine Feinemulsion bzw. -dispersion überführt. Insbesondere das Stress-Verweilzeitverhalten und die darauf erfolgende Reaktion eines protein-stabilisierten dispersen Systems bedarf einer vertieften wissenschaftlichen Klärung. Hieraus können mechanistische Schädigungsmodelle abgeleitet werden. Die im Emulgier-Prozess auftretenden mikromechanischen Belastungen auf biologische Systeme sind nicht vollständig geklärt, die Prozessumgebung ist somit noch weiter zu entwickeln im Hinblick auf die Anpassung an spezielle biologische Systeme.

Um den Einfluss des Premix-Emulgierverfahrens und der dabei auftretenden Stress-Verweilzeit-Belastungen auf die agglomerierten Proteine (hier β-Lactoglobulin) im Fluid und an den Phasengrenzflächen zu untersuchen, werden numerische Untersuchungen auf molekulardynamischer Ebene an Proteinstrukturen durchgeführt. Diese Untersuchungen zeigen, inwieweit die Proteinstrukturen durch den Emulgiervorgang belastet und geschädigt werden können, beziehungsweise ob eine proteinschonendere Emulgierung mit den Membranen möglich ist.

Ergebnisse

Zielsetzung des Projektzeitraumes war die Untersuchung der Proteinentfaltung an Öl-Wasser-Grenzflächen und die Beschreibung der Auswirkungen strömungsinduzierten Scherbelastungen auf die adsorbierten Strukturen.

Proteinentfaltung an der Phasengrenzfläche:
Die Problematik der Proteinentfaltung an Phasengrenzflächen wurde bereits im vorherigen Projektantrag erläutert. Aufgrund der hohen Zeitskalen kann eine Proteinentfaltung in den in der Molecular Dynamics (MD) darstellbaren Zeiträume unter Normalbedingungen (T = 300 K) nicht beobachtet werden. Um diese Zeiträume zu verkürzen wird daher die kinetische Energie (Temperatur) des Systems erhöht. Erste erfolgreiche Tests damit wurden bereits im vorherigen Antrag vorgestellt. Inhalt des ersten Arbeitspaketes dieses Projekt war daher, ein repräsentatives Temperaturniveau zu ermitteln, welches die in der Literatur beschriebene Entfaltungscharakteristik widerspiegelt. Daher wurden verschiedene Temperaturniveaus überprüft. Abb. 4 zeigt beispielhaft die Resultate bei T = 400; 500; 600 K.

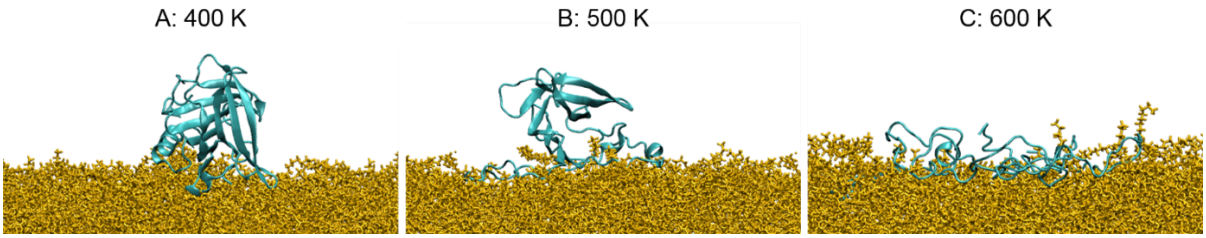

Abb. 4: Entfaltung von β-Lactoglobulin an der Öl-Wasser-Grenzfläche bei unterschiedlichen Temperaturniveaus.

Der Vergleich der drei Temperaturniveaus zeigt, dass bei T = 400 K (A) nahezu keine Änderung der Sekundärstruktur eintritt, bei T = 600 K (C) wird hingegen das komplette Protein denaturiert. Beide Temperaturniveaus eignen sich daher nicht zur Darstellung der Proteinentfaltung an Phasengrenzflächen. Bei T = 500 K (B) kann eine teilweise Entfaltung beobachtet werden. Auffällig dabei ist, dass die fassähnliche Struktur aus antiparallelen β-Faltblattstrukturen weitestgehend intakt bleibt. Dieser Strukturtyp bildet den stabilsten Teil von β-Lactoglobulin (BLG) und eine völlige Denaturierung an der Phasengrenzfläche ist unwahrscheinlich. Nichtsdestotrotz kann ein Rückgang an β-Faltblattstrukturen festgestellt werden, wie auch in (Zhai et al., 2010) beschrieben wird. Daher erscheint eine Entfaltung bei T = 500 K als am geeignetsten für die folgenden Untersuchungen und wird daher für die weiteren Studien verwendet. Die Untersuchung unterschiedlicher pH-Werte und Adsorptionskonfigurationen hat dabei ergeben, dass sich je nach Konfiguration unterschiedliche Entfaltungsgrade ergeben. Um diese auszudrücken wurde der RMSD (root mean square deviation)-Wert, also die Standardabweichung vom nativen Zustand bestimmt. Dieser beträgt in der MD-Simulation unter Normalbedingungen (T = 300 K) etwa 1.5 Å. Im Rahmen der Entfaltungsuntersuchungen wurden im Vergleich Werte zwischen 3.4 und 14.1 Å erreicht.

Scherbeanspruchung an der Phasengrenzfläche:
Zur Untersuchung des strömungsinduzierten Einflusses auf die adsorbierten Proteine wurden Schergradienten parallel zur Phasengrenzfläche angelegt. Für die Untersuchung der unterschiedlichen Schergradienten wurden Scherraten in der Größenordnung 10^9 s^{-1} verwendet. Unterhalb konnte kein Einfluss auf die Proteine beobachtet werden. Auch dies ist damit zu begründen, dass einerseits die benötigten Zeitskalen zu groß sind, andererseits damit, dass die bestehen Modelle nicht auf mechanische Denaturierungsprozesse ausgelegt sind. Die gewonnenen Erkenntnisse sind daher auf qualitativer Ebene zu bewerten. Die Resultate der Untersuchung sind in Abb. 5 beispielhaft für einen pH-Wert von pH = 3.5 aufgeführt, da hier die höchsten Entfaltungsgrade erreicht wurden.

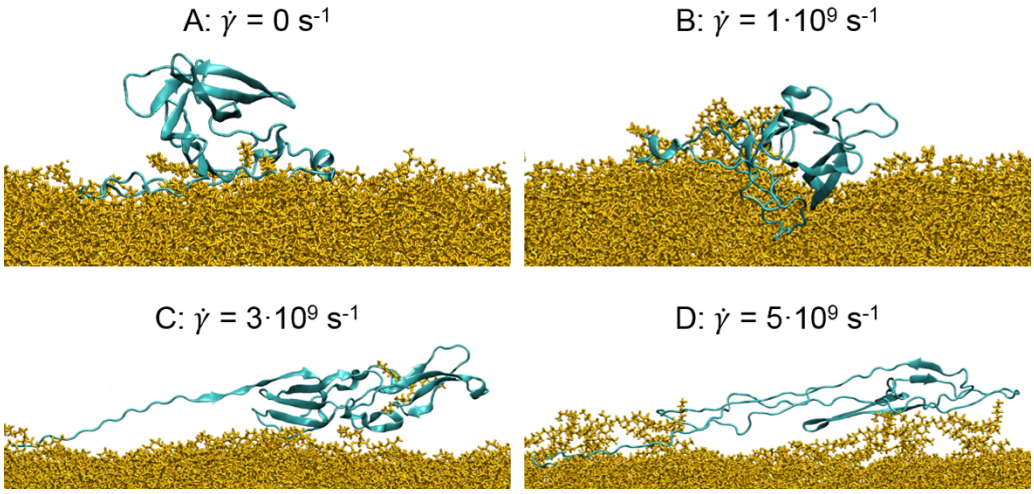

Abb. 5: Proteinbeanspruchung bei unterschiedlichen Scherraten.

Bei der niedrigsten Scherrate (B) ist im Vergleich zum Startzustand (A) lediglich eine Deformation des Proteins zu beobachten. Auch nach langer Simulationszeit (>100ns) kommt es zu keiner weiteren Denaturierung oder Ablösung. Bei höheren Scherraten (C und D) kommt es hingegen zu einer Veränderung der Sekundärstruktur. Nach anfänglicher Deformation löst sich das Protein teilweise von der Phasengrenzfläche. Das Protein wird auseinandergezogen, bis sich auch der letzte Teil von der Phasengrenzfläche ablöst. Der Beanspruchungsverlauf erscheint dabei zwischen bei beiden Scherraten (C und D) ähnlich. Der einzige Unterschied sind die Zeiträume (C: >30 ns, D: <10ns). Dies zeigt, dass eine niedrigere Beanspruchung (C) aufgebracht über einen längeren Zeitraum zu einer Strukturschädigung führen kann, ebenso wie eine höhere Belastung über einen kürzeren Zeitraum. Dadurch bestätigt sich die Grundhypothese des Projekts, dass bei der Schädigung von Proteinen nicht nur die Höhe des Stresses, sondern auch der Beanspruchungszeitraum, also das Stress-Verweilzeit-Verhalten, eine zentrale Rolle spielt. Die Proteindeformation zeigt jedoch auch, dass bei einer Deformation über die Phasengrenzfläche eine Beeinflussung durch benachbarte Proteine nicht ausgeschlossen werden kann. In Emulsionen liegen in der Regel vollständig bis hin zu multipel belegte Grenzflächen vor. Daher sind Effekte auf das Deformationsverhalten, hervorgerufen durch die räumliche Ausdehnung und elektrostatische Wechselwirkung benachbarter Protein, anzunehmen. Eine Ausweitung der Untersuchung auf Multiproteinszenarien ist daher der nächste Schritt.

Um die Auswirkungen der Grenzflächenbeanspruchung in Abhängigkeit des Entfaltungsgrades zu beschreiben, wurden die Untersuchungen für die unterschiedlichen Protein-Konfigurationen fortgeführt. Zudem wurde die Beanspruchungsrichtung variiert. Abb. 6 zeigt dabei die prozentuale Änderung der Sekundärstruktur in Abhängigkeit des Entfaltungsgrades und der aufgebrachten Beanspruchung normiert auf die Adhäsionskraft des Proteins.

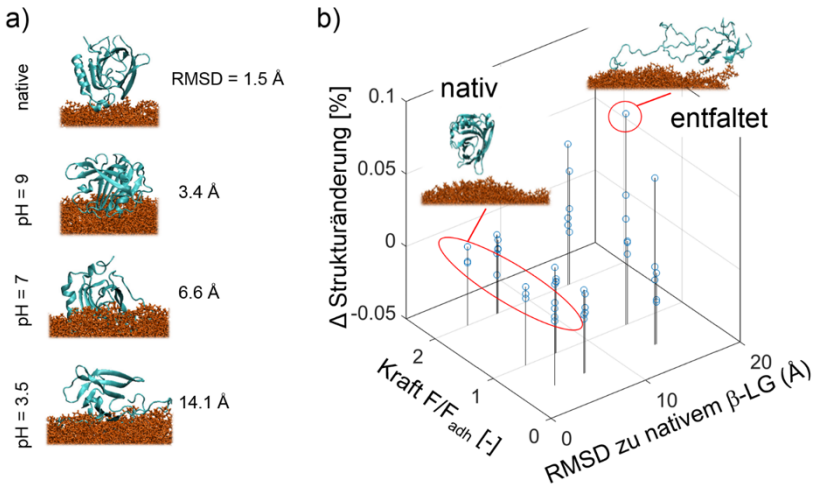

Abb. 6: Zusammenhang zwischen der Proteinentfaltung und dem RMSD-Wert (a) und Änderung der Sekundärstruktur als Funktion des Entfaltungsgrades und der aufgebrachten Beanspruchung (b).

Die Daten in b) zeigen deutlich, dass die stressbedingte Strukturänderung mit zunehmenden Entfaltungsgrad (exemplarisch in a) dargestellt) im Mittel zunimmt. Dabei liegen die beiden niedrigsten Entfaltungsgrade (RMSD = 3.4 Å und RMSD = 6.6 Å) nur unwesentlich über den lösungsbedingten Strukturschwankungen des nativen Proteins. Erst ab höheren Entfaltungsgraden (hier 14.1 Å) tritt ein deutlich stresssensitiveres Verhalten des Proteins auf. Die Höhe der aufgebrachten Kraft spielt dabei eine untergeordnete Rolle. Viel mehr ist die Kombination aus Kraft und Zeit (Stressverweilzeit-Verhalten) entscheidend, wie schon zu Abb. 5 erläutert. Die Strukturänderung ist dabei von der Adsorptionskonfiguration und der Beanspruchungsrichtung abhängig. So ergeben sich beispielsweise für den höchsten Entfaltungsgrad (RMSD = 14.1 Å) große Schwankungen in den Strukturänderungen. Insgesamt konnte durch die mechanische Beanspruchung von BLG nach Entfaltung an der Phasengrenzfläche ein stresssensitiveres Verhalten im Vergleich zur nativen Form beobachtet werden. Dadurch ist eine Strukturänderung im vergleichsweise scherarmen Premix-Membranemulgierprozess im Bereich des Möglichen.

Ausblick

Die bisherigen Untersuchungen zeigen aber auch, dass aufgrund der Streckung der Proteine entlang der Phasengrenzfläche (siehe Abb. 5) ein Einfluss benachbarter Proteine nicht ausgeschlossen werden kann. Gerade bei voll belegten Phasengrenzflächen (Monolayer/Multilayer), wie es in Emulsionen typisch ist, kann dieser Einfluss das Deformationsverhalten und somit die Strukturänderung beeinflussen. Dabei sind einerseits räumliche Kriterien, also auch elektrostatische Wechselwirkungen entscheidend. In der Fortsetzung dieses Projekts soll daher gezielt die mechanische Beanspruchung von Proteinschichten untersucht werden und der Effekt der Protein-Protein-Interaktion im Vergleich zur Einzelproteinbetrachtung dargestellt werden.

Vorträge / Poster

1. Tobias Wollborn, Udo Fritsching, Stress residence time behavior at liquid-liquid interfaces and their influence on the formulation, MAPEX Symposium 2018, Bremen, Deutschland, 18.-19.06.2018 (Poster)

6.11 hbk00032: Evaluating the FiniteVolumE Sea Ice-Ocean Model v. 2.0 at different resolutions

HLRN-Projektkennung: hbk00032

Laufzeit: III/2018–II/2019

Projektleiter: Prof. Dr. Thomas Jung [1]

Projektbearbeiter: Dmitry Sidorenko[2], Dirk Barbi, Sergey Danilov, Helge Gößling, Özgür Gürses, Sven Harig, Jan Hegewald, Nikolay Koldunov, Thomas Rackow, Natalja Rakowsky, Dmitry Sein, Tido Semmler, Qiang Wang, Claudia Wekerle

Institut / Einrichtung: [1] also at University of Bremen
[2] Alfred-Wegener-Institute for Polar and Marine Research, Bremerhaven

Summary

Recent attention of climate researches has been paid to the ocean components which operate on unstructured meshes and allow for variable resolution in key areas of the global ocean. One of these models is the Finite Element Sea Ice-Ocean Model (FESOM 1.4; Wang et al., 2014, Danilov et al., 2015) which has proven its validity in a series of scientific applications. FESOM 1.4 constitutes the ocean component of a climate system model (Sidorenko et al., 2015; Rackow et al., 2015) where it is coupled to the atmosphere model ECHAM6.3 (Stevens et al. 2013). AWI-CM is committed to several subprograms of CMIP phase 6.

Along with using FESOM 1.4 in various scientific applications faster numerical solutions operating on unstructured meshes have been sought for. A new dynamical core for FESOM has been developed (Danilov et al. 2017, Scholz et al. 2019). FESOM version 2.0 provides up to 4x times speedup compared to its preceder version 1.4, ensuring a throughput similar to that of regular-mesh models. The dynamical core of FESOM 2.0 is based on a finite volume discretisation and the new abbreviation of FESOM reads as the Finite-volumE Sea ice–Ocean Model.

In this project we evaluate FESOM 2.0 in standalone configurations. Our main objectives are (1) to analyze how different resolutions and surface forcings impact the simulated ocean state, (2) how to design a so called density function for distributing the prescribed amount of surface nodes and (3) to investigate the impact of representing mesoscales in key regions of the North Atlantic. In order to achieve these goals we constructed several numerical grids with different resolutions and conducted several ocean only simulations. We compare the multiple model results, analyze the differences and make recommendations for designing the optimal resolution grid.

Resolution density function vs. uniform resolution

Here we compare two non-uniform resolution distributions with ~1.5 and 5 million surface nodes (referenced thereafter as HR and XR, respectively) and another two which are similar in size but the grid points are distributed uniformly (referenced thereafter as ORCA25 and

STORM for low and high resolution, respectively). The uniform resolution meshes are based on well-known structured meshes (1/4° ORCA25 and 1/10° STORM) and obtained by division of the regular mesh rectangles into two triangles.

HR is an unstructured mesh that has a background resolution comparable with ORCA25. In HR and XR the surface nodes have been redistributed according to the observed variance of the sea surface height (see e.g., Sein et al., 2016) as derived from satellite altimetry. In XR the resolution density function takes further into account the information of the Rossby Radius of deformation by having two grid points per Rossby Radius over most of the globe (see e.g., Sein at al., 2017). The FESOM configuration of HR and ORCA25 meshes simulate ~15 years per day running on 30 HLRN nodes while XR and STORM meshes have 2 years per day throughput on 48 HLRN nodes.

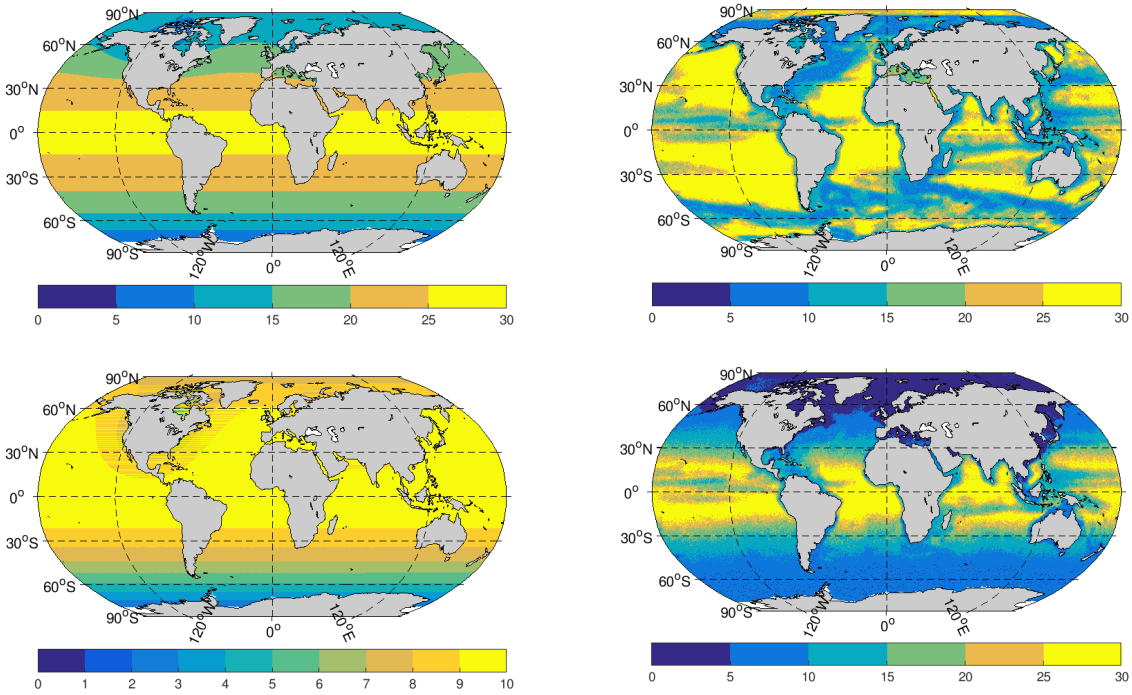

Figure 1: Mesh resolution of the model grids used in this study. ORCA25 (top left) and STORM (bottom left) are based on a regular grid approach. HR (top right) and XR (bottom right) are generated with refinement criteria based on sea surface height variability and Rossby radius of deformation, respectively. Note that the color bar is different in the bottom left figure. Number of surface nodes: ORCA25 = 0.9e6, HR = 1.3e6, XR = 5.0e6, STORM = 5.6e6

With each mesh we conducted 60-year model runs. The intercomparison and validation of results is still ongoing. As an example, we illustrate the simulated mid-depth temperature pattern averaged over the last 10 years of the simulation (Fig. 2). It is worth mentioning that the common biases present in general circulation ocean models (GCMs) such as cold biases in the eastern North Atlantic and warm biases in the Southern Ocean at 1000 m are notably reduced in HR and XR, but their overall spatial structures remain quite similar to ORCA25 and STORM. This indicates that the representation of bathymetry and the mesh resolution around the Gibraltar Strait might be significant where more nodes are deployed non-uniformly in HR and XR. On the other hand the systematic pattern of the model difference from climatology compares to those found in other models at different resolutions. This might indicate that there are general problems with the surface forcing.

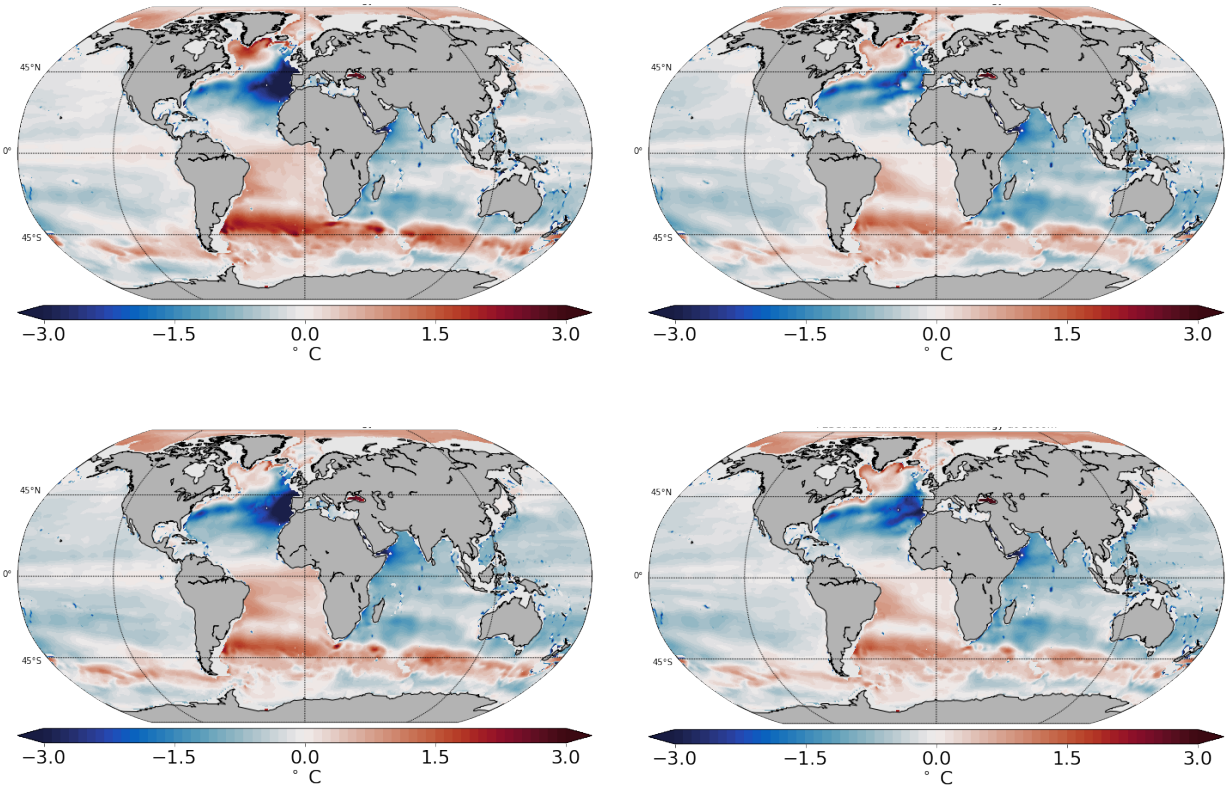

Figure 2: temperature difference from PHC climatology at at 1000 m as simulated with ORCA25 (upper left), HR (upper right), STORM (lower left) and XR (lower right) averaged means over 1998-2007 were used.

Coarsening approach for the North Atlantic

Here we compare several model configurations which are shown in Fig. 3 and exploit resolutions of 4km (M4), 8km (M8) and 25km (M25) in the North Atlantic and the same basic resolution of 25km in rest of the ocean. Based on our initial analysis and computational resources we have decided to apply coarsening from 8km to 25km (background resolution), in order to evaluate the influence of mesoscales in each key region on the simulated ocean hydrography and the circulation. Therefore, we coarsen the M8 mesh in several key regions of the North Atlantic. The regions are shown in Fig. 3 and are chosen as the Gulf of Mexico (mesh I), Equatorial Belt (mesh II), the Gulf Stream (GS) region (mesh III), Labrador Sea and GS separation zone (mesh IV), eastern North Atlantic (mesh V) and the Arctic Ocean (meshVI).

The analysis of these runs is still ongoing. As one might expect results show that the biases become larger in the regions of coarsening. For instance, Fig. 4 shows the snapshots of sea surface temperature and the absolute velocity in the Gulf Stream region for M4, M8 and M25 meshes. It is evident that M4 simulates more turbulent structures than the coarser meshes M8 and M25.

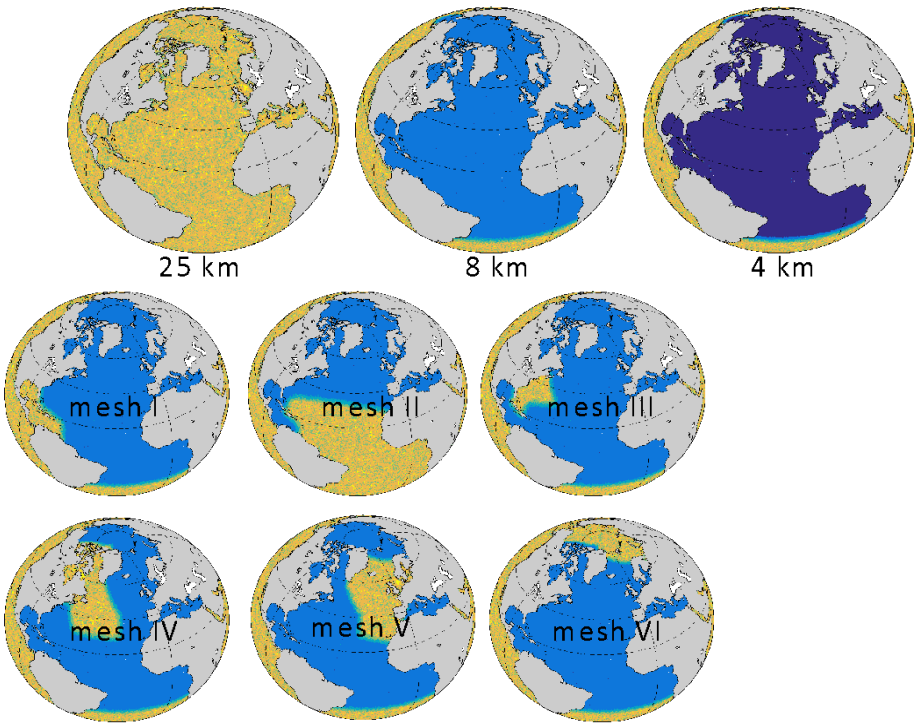

Figure 3: Parent and children meshes used in oursimulations. The resolution is represented by colors of yellow, light blue and dark blue for 25km, 8km, und 4km, respectively. Top row: Meshes with constant resolution in the North Atlantic and Arctic Ocean. Middle and bottom rows: Meshes where key regions are coarsened from 8km to 25km.

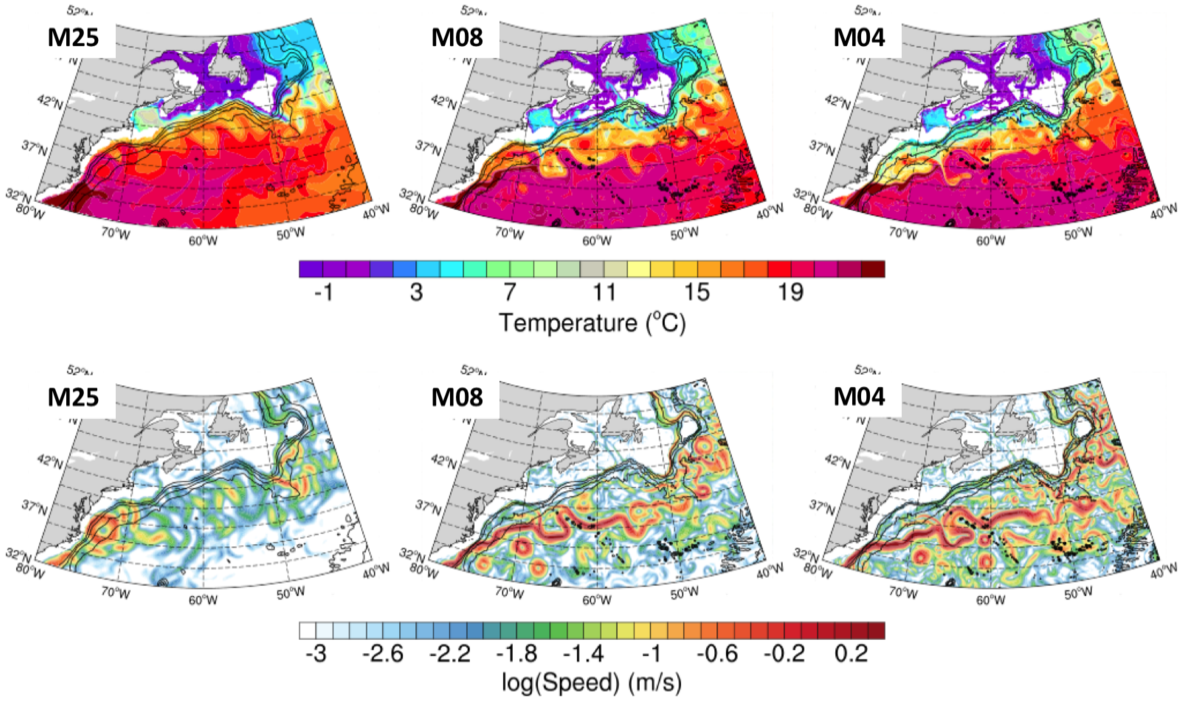

Figure 4: Snapshots of the simulated sea surface temperature and surface current speed (m/s) from three FESOM2 configurations with 25 km (left), 8 km (middle) und 4 km (right) resolution in the North Atlantic and Arctic (see also upper row in Figure 3).

References

Danilov, S. and co-authors, 2015: Finite-element sea ice model (FESIM), version 2. Geoscientific Model Development, 8(6), 1747-1761, doi:10.5194/gmd-8-1747-2015, 2015

Danilov, S., Sidorenko, D., Wang, Q. and Jung, T., 2017: The Finite-volumE Sea ice–Ocean Model (FESOM2), Geoscientific Model Development, 10(2), 765–789, doi:10.5194/gmd-10-765-2017.

Rackow, T., Goessling, H. F., Jung, T., Sidorenko, D., Semmler, T., Barbi, D., Handorf, D. (2016). Towards multi-resolution global climate modeling with ECHAM6-FESOM. Part II: climatevariability. Climate Dynamics, 1-26, doi:10.1007/s00382-016-3192-6

Scholz, P., Sidorenko, D., Gurses, O., Danilov, S., Koldunov, N., Wang, Q., Sein, D., Smolentseva, M., Rakowsky, N., and Jung, T.: Assessment of the Finite VolumE Sea Ice Ocean Model (FESOM2.0), Part I: Description of selected key model elements and comparison to its predecessor version, Geosci. Model Dev. Discuss., https://doi.org/10.5194/gmd-2018-329, in review, 2019.

Sein, D. V., Danilov, S., Biastoch, A., Durgadoo, J. V., Sidorenko, D., Harig, S. and Wang, Q. (2016). Designing variable ocean model resolution based on the observed ocean variability, Journal of Advances in Modeling Earth Systems, 8 (2), pp. 904-916, doi:10.1002/2016MS000650

Sein, D. V., Koldunov, N. V., Danilov, S., Wang, Q., Sidorenko, D., Fast, I., … Jung, T. (2017). Ocean modeling on a mesh with resolution following the local Rossby radius. Journal of Advances in Modeling Earth Systems, 9, 2601–2614, doi:10.1002/2017MS001099

Sidorenko, D. and co-authors 2015: Towards multi-resolution global climate modeling with ECHAM6–FESOM. Part I: model formulation and mean climate. Climate Dynamics, 44(3-4), 757-780, doi:10.1007/s00382-014-2290-6

Stevens, B. and co-authors, 2013: Atmospheric component of the MPI-M Earth System Model: ECHAM6. Journal of Advances in Modeling Earth Systems, 5(2), 146-172, doi:10.1002/jame.20015

Wang, Q. and co-authors, 2014: The Finite Element Sea Ice-Ocean Model (FESOM) v. 1.4: formulation of an ocean general circulation model. Geoscientific Model Development, 7(2), 663-693, doi:10.1016/j.ocemod.2013.10.005

6.12 *hbk00034:* Ice sheet - ice shelf - ocean interaction in the marginal seas of the Southern Ocean

and

hbk00038: Interaction between marine terminating glaciers and the ocean circulation in Northeast Greenland

HLRN Project ID::	hbk00034 / hbk00038
Run time:	III/2013-III/2019 / III/2014 – II/2019
Project Leader:	Prof. Torsten Kanzow[1,2]
Project Scientists:	Özgür Gürses[2], Svenja Ryan[2], Frank Schnaase[1,2], Lukrecia Stulic[2], Ralph Timmermann[2], Qiang Wang[2], Claudia Wekerle[2]
Affiliation:	[1] University of Bremen [2] Alfred Wegener Institute, Helmholtz Centre for Polar and Marine Research

Overview

In these projects, we use a global sea ice – ice shelf – ocean model to study the interaction between the deep ocean, the ice shelves fringing the Antarctic continent and part of the Greenland coast, and the ice sheets of Antarctica and Greenland. With its unstructured grid, the Finite Element Sea ice Ocean Model (FESOM) allows for an adequate resolution of the key regions, namely the grounding lines, the ice shelf fronts, and the continental shelf break. Special emphasis is placed on a correct representation of water mass exchange between the deep ocean and the continental shelf regions, and the pathways of water in the cavity beneath Filchner-Ronne Ice Shelf (FRIS) and the 79-North Glacier. Coupling with dynamic ice sheet/shelf models is one of the key activities in these projects and will allow for a complete and consistent representation of ocean – ice sheet interaction in decadal- to centennial-scale simulations. With the high computational burden imposed by the use of a finite-element ocean model (to which there is no alternative if local processes are to be represented in a global system), the projects depend on resources provided through the HLRN.

Results

One of the focus projects in this reporting period has addressed the interaction between the icescape in the southwestern Weddell Sea, the distribution of sea ice net growth rates on the continental shelf off the Filchner Ronne Ice Shelf (FRIS) front, and the FRIS cavity hydrography and ice shelf basal melt rates. A calving event in 1986 has released a giant tabular iceberg from Filchner Ice Shelf, and a large piece of this iceberg (A-23A) has remained grounded on the eastern slope of Berkner Bank. A mélange of sea ice and (smaller) icebergs tends to fill in the area south of this iceberg, affecting ocean circulation and increasing sea ice concentration to the eastern (luv) / decreasing sea ice concentration on the western (lee) side of the ice tongue. We used MODIS ice-surface temperature data to get the best possible information about existence, location, and extent of this time-varying fast-icebridge. In order to mimic the blocking of the ice movement by the fast-ice bridge in the

model, zero sea ice velocities were prescribed inthe area detected as fast ice. Results of this „FWall“ experiment were then compared to a reference run without data assimilation and thus no fast-ice bridge developing („FCCLM“).

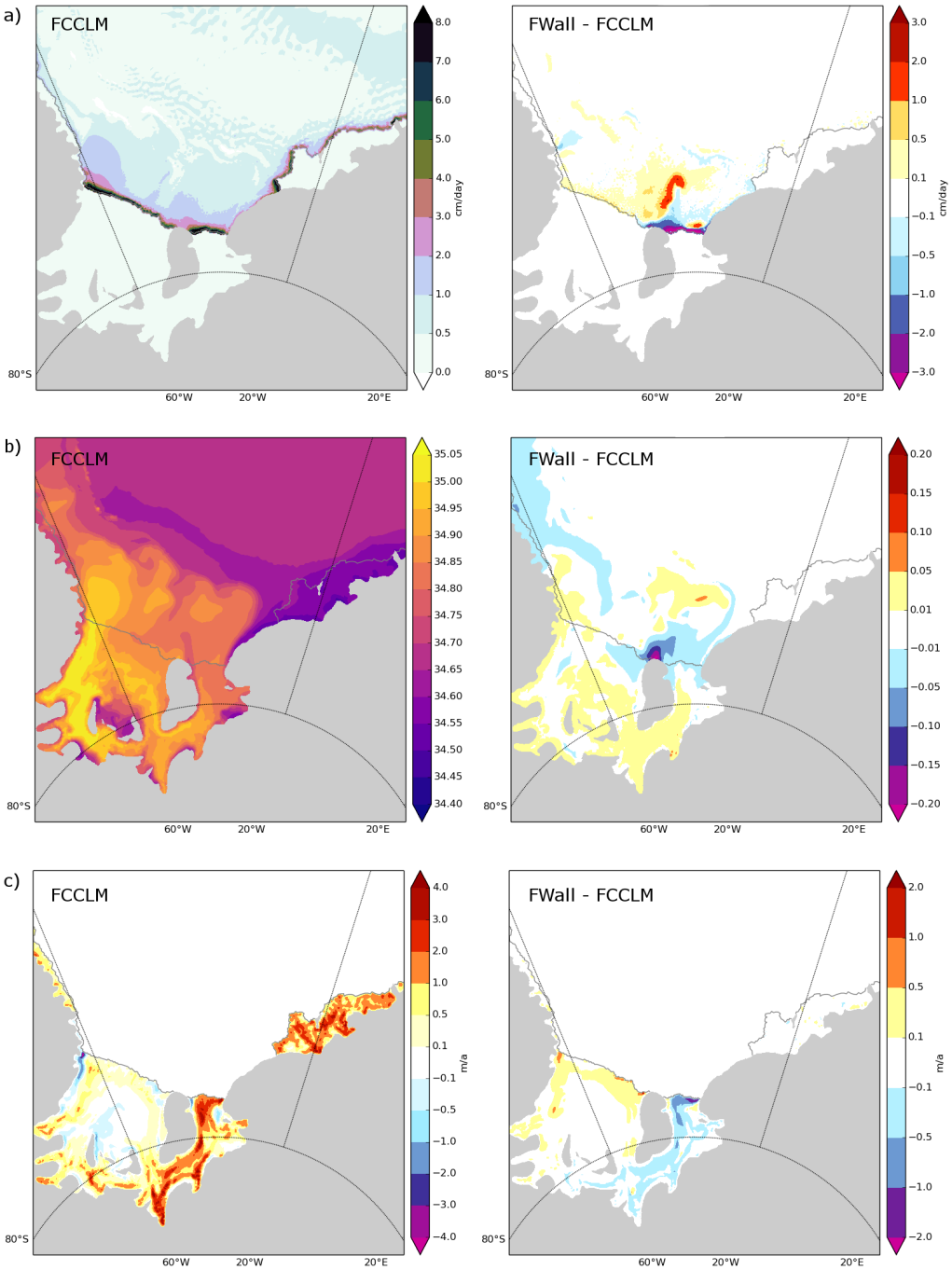

Fig. 1: a) Mean April-September 2002-2014 sea ice production from the FCCLM reference experiment and difference between the FWall simulation and FCCCLM. b) Mean September 2002-2014 bottom salinity from FCCLM and difference between FWall and FCCLM. c) Mean 2002-2014 basal melt rates from FCCLM and difference between FWall and FCCLM. Modified after Stulic et al. (in prep.)

We find that position and shape of the fast-ice bridge in the sensitivity experiment substantially affect interannual variability of polynya sea ice production. Model simulations yield an increased sea ice production westward of the ice bridge and a reduction eastward of it (Figure 1a). Bottom salinity anomalies (Figure 1b) reveal a similar pattern with reduced salinities in the region covered by the fast icebridge. Changed density gradients in the presence of the fast ice bridge affect the ocean circulation leading to decreased basal melt rates below the Filchner Ice Shelf (Figure 1c). Compared to MODIS-based estimates of sea ice net growth rates in various sectors of the southwestern Weddell Sea continental shelf, the simulation considering the fast ice bridge gives more realistic results. A paper reporting on these findings is currently being prepared.

Another focus project in 2018 has been on the exploration of potential benefits and drawbacks associated with discretizing sub-ice-shelf cavities with z coordinates instead of the terrain-following vertical coordinates that have to date been used in FESOM studies modelling ice shelf-ocean interaction. While z coordinates allow for a smaller minimum water column thickness in the cavity and for better representation of lateral mixing in the ocean (which typically follows lines of equal density, i.e. the so-called isopycnals), a smooth and realistic representation of the topographies of the ice shelf base and the seafloor and the dynamic treatment of dense-water plumes are more straightforward in terrain-following coordinates.

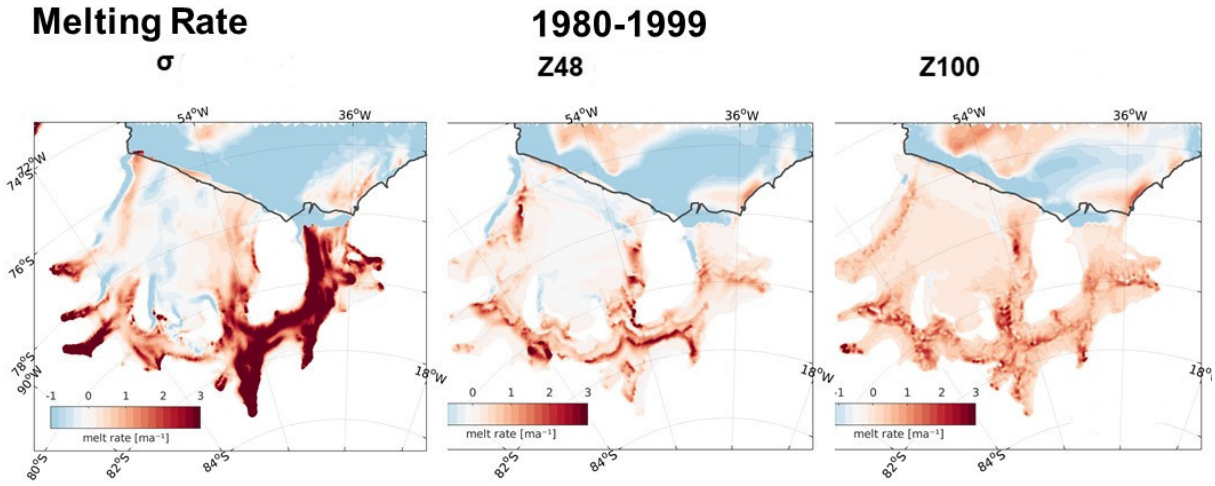

Fig. 2: Modelled ice shelf basal melt rates with terrain-following coordinates (left) and in a z-coordinate configuration with 48 (middle) and 100 (right) levels.

Results on a coarse-scale (not eddy-resolving) mesh indicate that the model representation of cavity water masses improves with z coordinates, but the distribution of ice-shelf basal melt rates falls short of what has been achieved with FESOM in terrain-following coordinates (Fig. 2) – with important implications for the ongoing ice shelf-ocean coupling projects. Increasing the vertical resolution in the z-coordinate configuration only marginally cures this deficiency. Whether an upgrade to eddy-resolving meshes leads to convergence of the two solutions is one of our current reseach items. We use the FRIS as a testbed for this sensitivity study because the existence of a comparatively large observational dataset allows for a more robust validation there than would be possible for, e.g., the 79N Glacier. Results, however, are clearly valid for model studies in the Arctic as well as in the Antarctic.

Further activities in this project have focussed on

1. a model intercomparison and IPCC scenario project that led to two peer-reviewed publications and on
2. a multi-parameter optimization of sea ice model parameters using the Green's functions approach

Results from these sub-projects will be highlighted in the report for 2019.

Outlook

Experience gained with and infrastructure developed for the coupled ice sheet – ice shelf – ocean model *RAnGO* (Timmermann and Goeller, 2017) is currently utilized for the implementation of a pan-Antarctic coupled model based on a combination of FESOM with the Parallel Ice Sheet Model (PISM). Work on this project is performed in co-operation with the Potsdam Institute for Climate Impact Research (PIK).

Publications

1. Naughten, K.A., K.J. Meissner, B.K. Galton-Fenzi, M.H. England, R. Timmermann, and H.H. Hellmer: Future projections of Antarctic ice shelf melting based on CMIP5 scenarios. *Journal of Climate*, DOI: 10.1175/JCLI-D-17-0854.1, 2018
2. Naughten, K.A., K.J. Meissner, B.K. Galton-Fenzi, M.H. England, R. Timmermann, H.H. Hellmer, T. Hattermann, and J.B. Debernard: Intercomparison of Antarctic ice-shelf, ocean, and sea-ice interactions simulated by MetROMS-iceshelf and FESOM 1.4. *Geosci. Model Dev.*, 11, 1257-1292, DOI:10.5194/gmd-11-1257-2018, 2018.
3. Ryan, S.: On the Flow of Modified Warm Deep Water toward the Filchner Ronne Ice Shelf, Weddell Sea, Antarctica. PhD thesis, University Bremen, 2018.
4. Wekerle, C., T. Krumpen, T. Dinter, W.J. von Appen, M. Iversen, and I. Salter: Origin and properties of sediment trap catchment areas in Fram Strait: results from Lagrangian modelling and remote sensing. Frontiers in Marine Science, 5, doi:https://doi.org/10.3389/fmars.2018.00407, 2018.

Presentations

1. Goeller, S. and R. Timmermann: Response to Filchner-Ronne Ice Shelf cavity warming in a coupled ocean-ice sheet model. EGU General assembly, 2018.
2. Gurses, O., S. Ryan, Q. Wang, R. Timmermann, C. Rodehacke, V. Kolatschek, M. Pfeiffer, and T. Semmler: Modelling the ocean circulation underneath the Filchner-Ronne ice shelf: What is the role of vertical discretization? Forum for Research into Ice Shelf Processess, Aussois, 2018.
3. Ryan, S., M. Schröder, R. Timmermann, T. Hattermann, and T. Kanzow: On the Modified Warm Deep Water Flow toward the Filchner Ronne Ice Shelf: Observations and Model Results. EGU General assembly, 2018.
4. Stulic, L., Timmermann, R., Paul, S., Zentek, R., Heinemann, G.: Sea-ice production in the southern Weddell Sea: role of fast ice, FRISP, September 3-6, 2018, Aussois, France
5. Stulic, L., Timmermann, R., Paul, S., Zentek, R., Heinemann, G.: Sea ice production in the southern Weddell Sea: role of atmospheric forcing and fast ice, EGU General Assembly, 2018.
6. Timmermann, R., Ö. Gürses, M. Rückamp, and F. Schnaase: Ice sheet-ocean coupling with FESOM: Technology, caveats and perspectives. REKLIM workshop, Boppard, 2018.
7. Timmermann, R., Ö. Gürses, M. Rückamp, and F. Schnaase: Ice sheet-ocean coupling with FESOM: Technology, caveats and perspectives. FRISP workshop, Aussois, 2018.

6.13 hbk00045/hbk0057: Joint Report

hbk00045: Determination of vertically resolved trends in the stratospheric ozone from SCIAMACHY limb measurements

HLRNProject ID:	hbk00045
Run time:	IV/2015 – IV/2018
Project Leader:	Dr. Alexei Rozanov
ProjectScientists:	C. Arosio
Affiliation:	Institute of Environmental Physics, University of Bremen

hbk0057: Persistent ozone depletion in the tropical stratosphere: identifying possible reasons

HLRNProject ID:	hbk00057
Run time:	I/2017 – II/2019
Project Leader:	Dr. Alexei Rozanov
Project Scientists:	E. Galytska
Affiliation:	Institute of Environmental Physics, University of Bremen

Overview

The crucial role of the stratospheric ozone for the thermal balance of the Earth's atmosphere as well as for the atmospheric dynamics, biosphere and human health determines the continuous interest of the scientific community to the state of the stratospheric ozone layer. After the anthropogenic emission of halogenated ozone depleting species has been ruled out by Montreal Protocol and its amendments the severe ozone decline discovered in early eighties of the last century began to slow down and even some indications of the ozone recovery have been inferred from observations (Newchurch et al., 2003; WMO 2007, 2011; Yang et al., 2006).

While earlier studies used total ozone amounts to study changes in the stratospheric ozone, rigorous investigations require the availability of long-term vertically resolved data sets as some altitude dependent processed might be masked out then vertically averaging the ozone profiles. For example, when analyzing the vertically resolved time series of ozone in the tropics during the first decade of the 21st century, the ozone recovery was identified in the middle to lower stratosphere (below about 30 km) while a significant ozone depletion was observed at altitudes of about 35 km (Eckert et al., 2013; Gebhardt et al., 2014; Kyrölä et al., 2013, Sofieva et al., 2017). Being vertically integrated these opposite changes result in a slightly positive trend which explains the signatures of a recovery seen in the observations of the ozone total column.

This study uses vertically resolved global distributions of stratospheric ozone obtained from measurements of the scattered solar light in the limb viewing geometry from the space-borne SCIAMACHY (SCanning Imaging Absorption spectroMeter for Atmospheric CHartographY) instrument (Bovensmann et al., 1999) onboard the European satellite Envisat to investigate the reasons for a significant decline in the tropical upper stratospheric ozone during the first decade of the 21st century. The investigations are supported by the modeling study using the

Chemical Transport Model (CTM)TOMCAT/SLIMCAT (Chipperfield, 2006). The results of these investigations are published by Galytska et al. (2019). Futhermore, the results obtained within the project hbk00045 are used to calculate tropospheric ozone colunms (Gaudel et al., 2018) and, jointly with the results from hbk00062, to obtain and analyze long term ozone records (Arozio et al., 2018).

Results

To investigate the reasons for the observed ozone decline in the tropical stratosphere between 30 an 35 km we investigated measured and modelled time series of ozone and NO_2. It was found out that the time series show a clear anti-correlation in both observed and modelled data with a strong decrease in ozone and strong increase in NO_2. Figure 1 shows a comparison of the changes in ozone and NO_2 obtained from SCIAMACHY observations and model runs of TOMCAT/SLIMCAT for the 2004 - 2012 period. As it is seen from the plot the results are in a good qualitative agreement showing a negative trend in ozone and a positive trend in NO_2 between30 and 35 km in the tropics (marked by dashed line boxes). However, the amplitudes of the trends in the modeled data are lower.

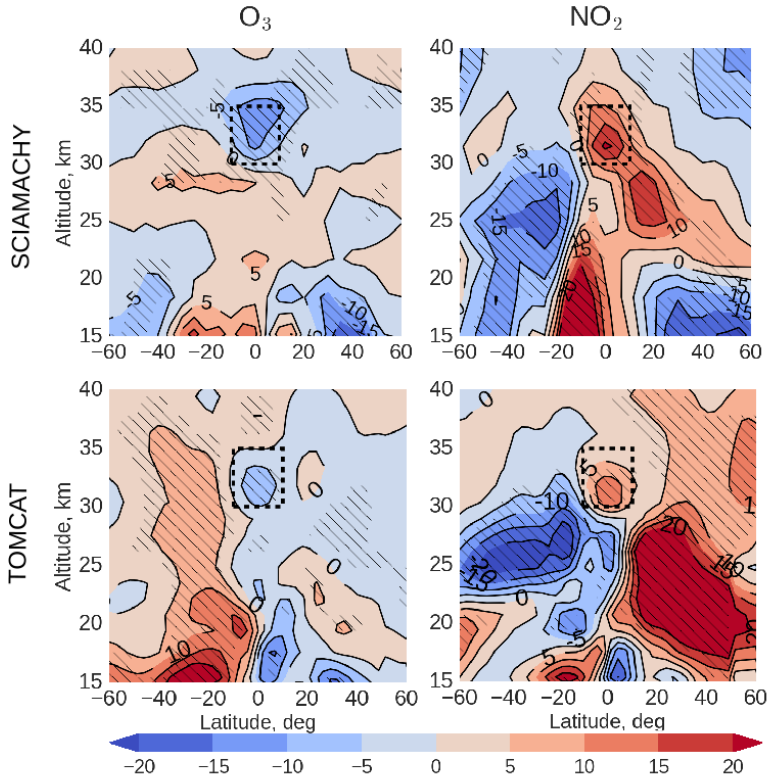

Figure 1: Ozone and NO2 linear changes (years per decade) from January 2004 to April 2012 from SCIAMACHY observations and SLIMCAT/TOMCAT model simulations. The dashed rectangle indicates the region of interest in the tropical mid-stratosphere. The hatched areas in (b) show changes significant at the 2σ level.

Investigation of the tracer-tracer correlations for ozone and NO_2 from SCIAMACHY observations and time series modelled by TOMCAT/SLIMCAT show a perfect anticorrelation for both data sets (see Figure 2). This confirms that the relationship between the two species is fully controlled by the chemical processes and these processes are well described by the model.

Nedoluha et al. (2015) suggested that the observed positive trends of NO_2 might be caused by a slowdown in the upwelling speed, which increases the residence time of N_2O (precoursor gas of NO_2) in the atmosphere and results thus in an increase of NO_2. However, our investigations of the age of air performed by using the TOMCAT/SLIMCAT model disprove this suggestion reporting insignificand nevative changes in the age of air during the period of interest. The results are shown in Figure 3 for the age of air (left panel) and its linear changes (right panel). Thus an indication of acceleration of the upwelling rather than of its slowing down (as suggested by Nedoluha et al. (2015)) was identified using the model data, although the results were statistically insignificant.

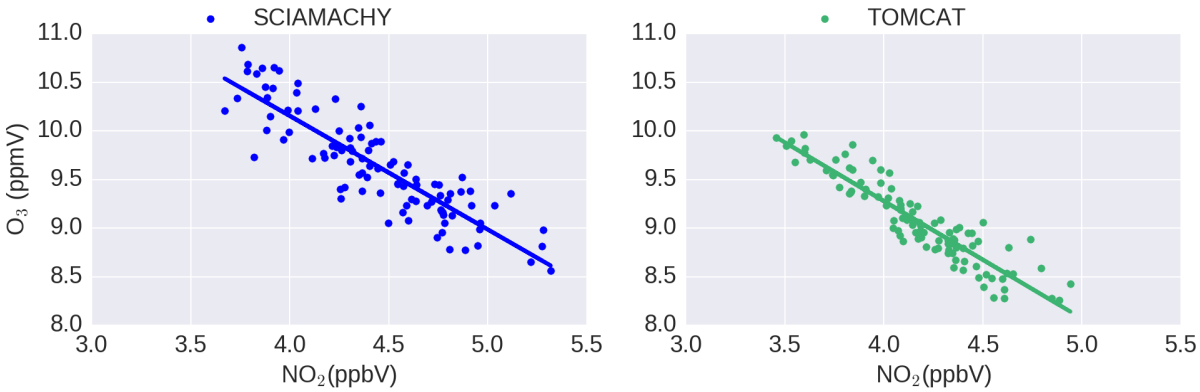

Figure 2: Tracer-tracer correlations from SCIAMACHY observations and SLIMCAT/TOMCAT model simulations.

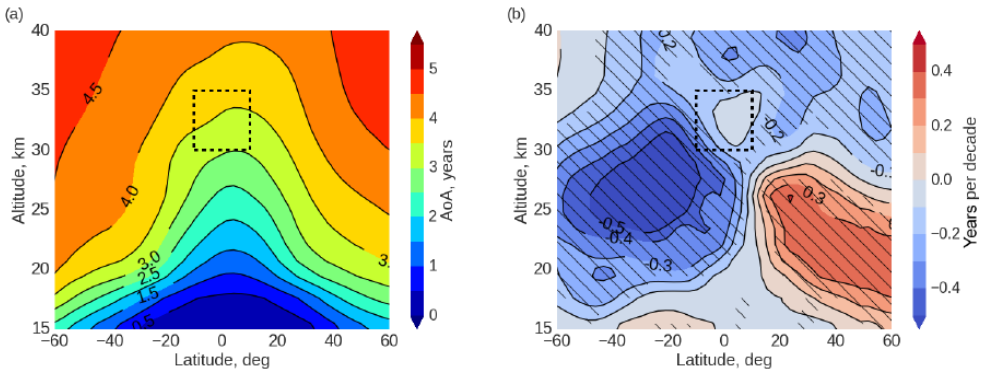

Figure 3: Latitude–altitude AoA (a) the zonally averaged distribution (years), (b) the linear changes (years per decade) from SLIMCAT model simulation during January 2004–April 2012. The dashed rectangle indicates the region of interest in the tropical mid-stratosphere. The hatched areas in (b) show changes significant at the 2σ level.

Analyzing the modeled trends in the age of air resolved by seasons, it was found that the circulation speeds up during the boreal winter while slowing down during the boreal autumn. These trends, however, cancel out when considering the whole year. With the increasing circulation speed, the amount of N_2O, which is a precursor of NO_2, increases resulting in the increase of NO_2 and the decrease of ozone (and vice versa). As the amount of N_2O is controlled by both the transport from the troposphere and photochemical destruction its variations are not canceled our when considering the whole year.

Figure 4 shows the measured and modeled time series of ozone and NO_2 for February and September and the corresponding trends. It is seen that the accelerating upwelling during the boreal autumn causes a strong increase in the NO_2 amount and the decrease in the ozone in both measured and modeled data. For February the situation is more complicated as the measured and observed trends do not agree, however, the observed trends are insignicant.

Thus it was concluded that the observed trends are caused by the seasonal variations in the change of the circulation speed. Possible reasons for these changes are currently under investigation.

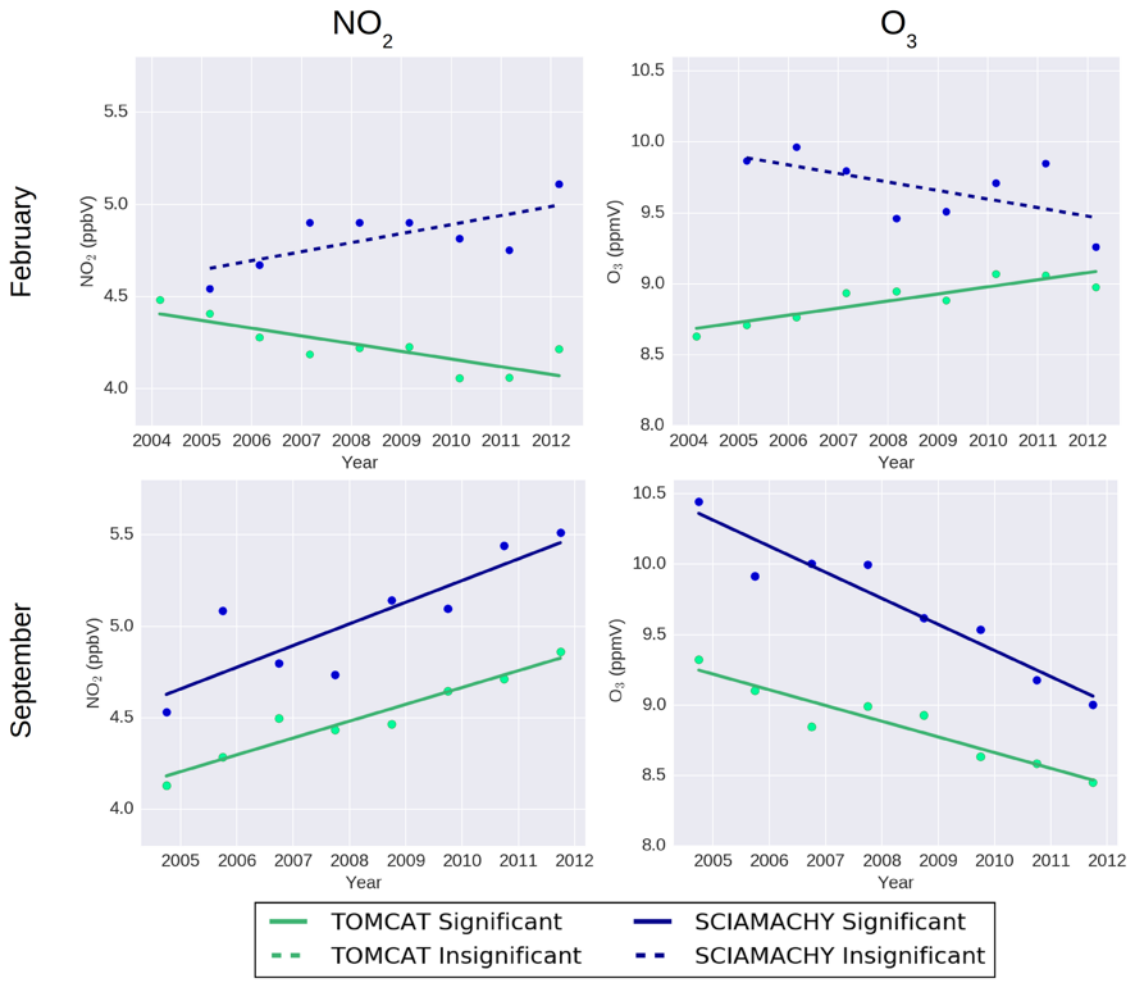

Figure 4: Monthly resolved ozone and NO2 trends from January 2004 to April 2012 from SCIAMACHY observations and SLIMCAT/TOMCAT model simulations.

Outlook

The project hbk00045 is completed. While the NO_2 related tasks within hb00057 are sucsessfully completed an issue with BrO time series still remains. As the obtained results on linear changes deviate from expectations and do not agree with the model results and other observations, futher investigations are needed to enable us to investigate a possible role of the bromine compounds in the stratospheric ozone changes.

Publications

1. Arosio, C., Rozanov, A., Malinina, E., Weber, M., and Burrows, J. P.: Merging of ozone profiles from SCIAMACHY, OMPS and SAGE II observations to study stratospheric ozone changes, Atmos. Meas. Tech. Discuss., https://doi.org/10.5194/amt-2018-275, in review, 2018.
2. Galytska E., Rozanov, A., Chipperfield, M.P., Dhomse, S.S., Weber, M., Arosio, C., Feng, W., and Burrows J.P., Dynamically controlled ozone decline in the tropical mid-stratosphere observed by SCIAMACHY, Atmos. Chem. Phys., 19, 767-783, https://doi.org/10.5194/acp-19-767-2019, 2019.
3. Gaudel, A., Cooper, O. R., Ancellet, G., Barret, B, Boynard, A., Burrows, J. P., et al.: Tropospheric Ozone Assessment Report: Present-day distribution and trends of tropospheric ozone relevant to climate and global atmospheric chemistry model evaluation. Elem Sci Anth. 2018; 6 (1):39. DOI: http://doi.org/10.1525/elementa.291.

Presentations

1. Arosio, C., Rozanov, A., Weber, M. and Burrows, J.P. (2018) Merging of ozone profiles from SCIAMACHY, OMPS-LP and SAGE II observations and trend studies. In: Second LOTUS workshop, 17-19 September 2018, Genf. (Unpublished)
2. Arosio, C., Rozanov, A., Galytska, E., Chipperfield, M.P., Dhomse, S. and Burrows, J.P. (2018) Merging ozone profiles from SCIAMACHY, OMPS-LP and SAGE II observations to study long-term stratospheric ozone changes. In: ATMOS 2018, 26.11. - 29.11.2018, Salzburg. (Unpublished)
3. Arosio, C., Rozanov, A., Malinina, E. and Burrows, J.P. (2018) Merging of stratospheric ozone profiles from OMPS and SCIAMACHY limb observations. In: EGU General Assembly, Vienna, Austria, April 2018, 08-13 April 2018, Vienna. (Unpublished)
4. Arosio, C., Rozanov, A., Malinina, E., and Burrows, J.P. (2018) Stratospheric ozone profile trends from SAGE II, SCIAMACHY and OMPS-LP merged observations. In: COSPAR 2018, 42th Assembly, 14-22 June 2018, Pasadena. (Unpublished)
5. Galytska, E., Chipperfield, M.P., Rozanov, A., Dhomse, S., Burrows, J.P. (2018) Understanding NO2 and O3 changes in tropical mid-stratosphere by means of a chemistry-transport model. In: European Geosciences Union (EGU) General Assembly 2018, 8-13 April 2018, Vienna, Austria.
6. Galytska, E., Rozanov, A., Chipperfield, M.P., Arosio, C., Dhomse, S., and Burrows, J.P. (2018) Ozone Decline in the Tropical Mid-stratosphere Observed by SCIAMACHY and Its Relation to the Stratospheric Dynamics. In: ATMOS-2018, 26-29 November, 2018, Salzburg, Austria.

References

1. Bovensmann, H.; Burrows, J. P.; Buchwitz, M.; Frerick, J.; Noël, S.; Rozanov, V. V.; Chance, K. V.; Goede, A. P. H. (1999). "SCIAMACHY: Mission Objectives and Measurement Modes". Journal of the Atmospheric Sciences. 56 (2): 127–150.
2. Chipperfield, M. P. (2006), New version of the TOMCAT/SLIMCAT off-line chemical transport model: Intercomparison of stratospheric tracer experiments. Q.J.R. Meteorol. Soc., 132: 1179-1203. doi:10.1256/qj.05.51
3. Eckert, E., von Clarmann, T., Kiefer, M., Stiller, G. P., Lossow, S., Glatthor, N., Degenstein, D. A., Froidevaux, L., Godin-Beekmann, S., Leblanc, T., McDermid, S., Pastel, M., Steinbrecht, W., Swart, D. P. J., Walker, K. A., and Bernath, P. F.: Drift-corrected trends and periodic variations in MIPAS IMK/IAA ozone measurements, Atmos. Chem. Phys., 14, 2571-2589, 2014.

4. Gebhardt, C., Rozanov, A., Hommel, R., Weber, M., Bovensmann, H., Burrows, J. P., Degenstein, D., Froidevaux, L., and Thompson, A. M.: Stratospheric ozone trends and variability as seen by SCIAMACHY from 2002 to 2012, Atmos. Chem. Phys., 14, 831-846, doi:10.5194/acp-14-831-2014, 2014.
5. Kyrölä, E., Laine, M., Sofieva, V., Tamminen, J., Päivärinta, S.-M., Tukiainen, S., Zawodny, J., and Thomason, L.: Combined SAGE II-GOMOS ozone profile data set for 1984-2011 and trend analysis of the vertical distribution of ozone, Atmos. Chem. Phys., 13, 10645-10658, doi:10.5194/acp-13-10645-2013, 2013.
6. Nedoluha, G. E., D. E. Siskind, A. Lambert, and C. Boone, The decrease in mid-stratospheric tropical ozone since 1991, Atmos. Chem. Phys., 15, 4215-4224, 2015, doi:10.5194/acp-15-4215-2015.
7. Newchurch, M. J., Yang, E.-S., Cunnold, D. M., Reinsel, G. C., Zawodny, J. M., and Russell III, J. M.: Evidence for slowdown in stratospheric ozone loss: First stage of ozone recovery, J. Geophys. Res., 108, 4507, doi:10.1029/2003JD003471, 2003.
8. Sofieva, V. F., Kyrölä, E., Laine, M., Tamminen, J., Degenstein, D., Bourassa, A., Roth, C., Zawada, D., Weber, M., Rozanov, A., Rahpoe, N., Stiller, G., Laeng, A., von Clarmann, T., Walker, K. A., Sheese, P., Hubert, D., van Roozendael, M., Zehner, C., Damadeo, R., Zawodny, J., Kramarova, N., and Bhartia, P. K.: Merged SAGE II, Ozone_cci and OMPS ozone profile dataset and evaluation of ozone trends in the stratosphere, Atmos. Chem. Phys., 17, 12533-12552, https://doi.org/10.5194/acp-17-12533-2017, 2017.
9. WMO: Scientific Assessment of Ozone Depletion: 2006, Global Ozone Research and Monitoring Project Report 50, World Meteorological Organization, Geneva, www.wmo.int/pages/prog/arep/gaw/ozone2006/ozoneasstreport.html, 2007.
10. WMO: Scientific Assessment of Ozone Depletion: 2010, Global Ozone Research and Monitoring Project Report 52, World Meteorological Organization, Geneva, www.unep.ch/ozone/AssessmentPanels/SAP/ScientificAssessment2010/00-SAP-2010-Assement-report.pdf, 2011.
11. Yang, E.-S., Cunnold, D. M., Salawitch, R. J., McCormick, M. P., Russell III, J. M., Zawodny, J. M., Oltmans, S., and Newchurch, M. J.: Attribution of recovery in lower-stratospheric ozone, J. Geophys. Res., 111, D17309, doi:10.1029/2005JD006371, 2006.

6.14 *hbk00055:* Investigating the biogeochemistry of the high latitudes during the period of rapid change: modelling and satellite retrievals

HLRNProject ID:	hbk00055
Run time:	IV/2017 – III/2019
Project Leader:	Prof. Dr. Bracher[1, 2]
ProjectScientists:	S. Losa[1], M. A. Soppa[1], M. Losch[1], V. Pefanis[1], J. Oelker[2]
Affiliation:	[1]Alfred Wegener Institute Helmholtz Centre for Polar and Marine Reesearch, Bremerhaven [2]University of Bremen

Overview

The aim of the computing project is to obtain long-term time series of ocean biogeochemical model simulations and satellite retrievals to analyse the changes in biodiversity and biogeochemical cycling observed over the lastyears in the Polar regions (the Southern and Arctic Oceans) and to improve our understanding of possible interactions between the open water, sea ice, snow, ocean biogeochemistry and ecosystem and chemical composition of the Atmospheric Boundary Layer under the recently observed climate changes. Within the HLRN project, the coloured dissolved organic matter (CDOM) and phytoplankton dynamics as well as phytoplankton diversity in response to Arctic Amplification are simulated with the biogeochemical model Darwin (Follows et al., 2007, Dutkiewicz et al., 2015) coupled to the Massachusetts Institute of Technology General Circulation Model (MITgcm, MITgcm Group, 2012). The study relates to the DFG project "**A**rti**c**Amplification: **C**limate Relevant **A**tmospheric and Surfa**C**e Processes, and Feedback Mechanisms **(AC)^3**" within the establishment of Transregional Collaborative Research Centre TR 172 and is partly conducted in the frame of the Helmholtz Climate Initiative **REKLIM** (Regional Climate Change), a joint research project of the Helmholtz Association of German Research Centres (HGF). In support to the DFG research "**PhySyn**" within the framework of the DFG-Priority Program 1158 "Antarctic Research" we simulate phenology and time series of the dominant phytoplankton functional types (PFTs) in the Southern Ocean (including the Great Calcite Belt).

Results

Within this computing project, a 6-PFTs version of the Darwin-MITgcm was further developed, which improved significantly the simulated phenology and dominance of the observed PFTs in the Southern Ocean (Figure 1). In particular, a series of experiments with different assumptions on the physiological traits of various phytoplankton groups allowed to set up the biogeochemical model version that describes best, to the authors knowledge, the observed competition and co-existence of diatoms, coccolithophores and *Phaeocystis sp.*. The new model configuration (augmented by two types of diatoms and two different life stages of *Phaeocystis*) led to plausible simulations of the coccolithophores and diatoms in **the Great Calcite Belt** (Losa et al. 2018). The simulated dynamics of these two important biomineralizing PFTs agree well with *in situ* data (Smith et al., 2017) and satellite-based information on similar phytoplankton groups: SynSenPFT (Losa et al. 2017, obtained within the same computing project running in previous years) and PFTs chlorophyll *"a"* derived given other hyperspectral satellite measurements from the Ozone Monitoring Instrument, OMI, and Global Ozone Monitoring Experiment – 2, GOME-2 (Losa et al. 2018).

Sufficient model simulations of PFTs and CDOM were obtained for the Arctic Ocean (Figure 2, 3). A precise evaluation of the results with available *in situ* observations (Gonçalves-Araujo et al., 2015, 2016, Liu et al. 2018, 2019) is still to be performed. Nevertheless, the current model configuration (together with satellite retrievals) gives the opportunity to investigate possible bio-physical interactions/feedbacks in the Arctic (Soppa et al. 2019, in revision).

Outlook

A series of model simulations are planned for the Arctic Ocean. This includes model sensitivity experiments with respect to the use of the radiative transfer model (RTM, Dutkiewicz et al., 2015) with simple parametrization of or spectrally depended and resolved absorption by CDOM and PFTs chlorophyll *"a"* for studying the biogeochemical impact on light penetration and radiative heating.

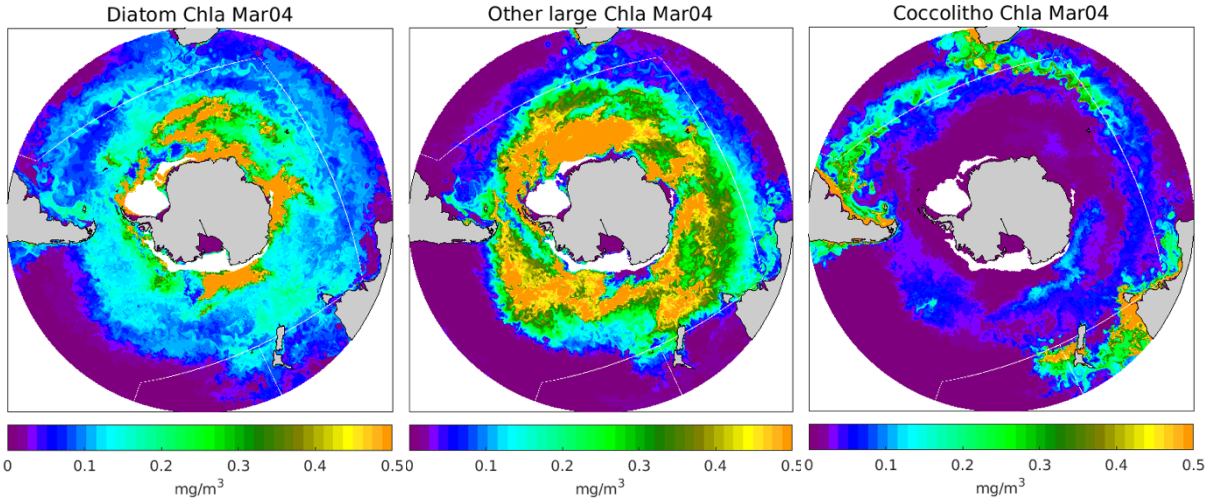

Fig. 1: Spatial distribution of the model simulated Southern Ocean chlorophyll "a" for diatoms (large + small), other large (nano-) phytoplankton (including *Phaeocystis*) and coccolithophores in August 2005.

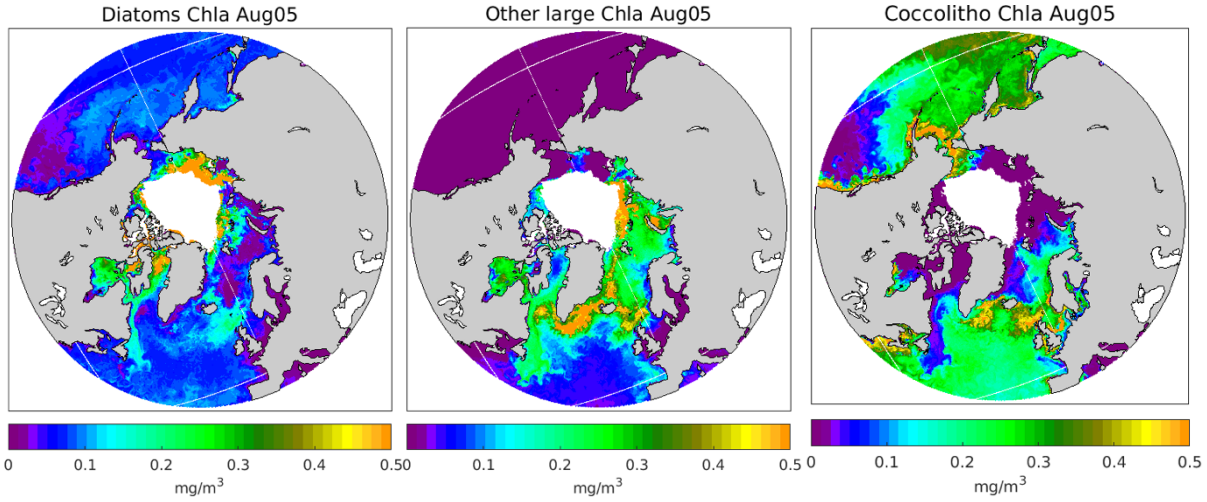

Fig. 2: Spatial distribution of the model simulated Arctic chlorophyll "a" for diatoms (large + small), other large (nano-) phytoplankton and coccolithophores in August 2005.

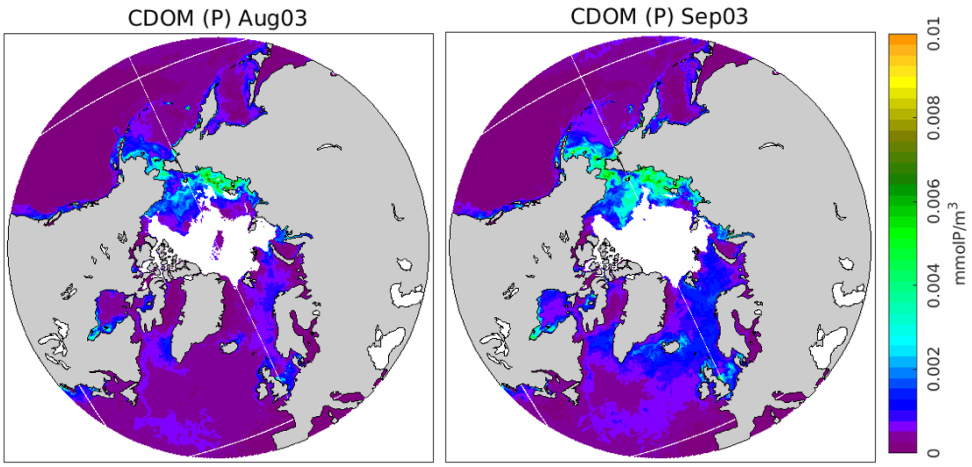

Fig. 3: Spatial distribution of the Arctic CDOM simulated for August and September 2003.

Publications

1. S. N. Losa, J. Oelker, M. A. Soppa, S. Dutkiewicz, M. Losch, T. Dinter, V. V. Rozanov, A. Richter, J.P. Burrows, A. Bracher, *Investigating the phytoplankton diversity in the great calcite belt: perspectives from hyper- and multispectral satellite retrievals and numerical modelling*. Extended Abstract of the XXIV Ocean Optics, Dubrovnik, Croatia (2018); https://oceanopticsconference.org/extended/Losa_Svetlana.pdf

Presentations

1. V.Pefanis, M. A. Soppa, S. Losa, S. Hellmann, M. Janout, V. Rozanov, T. Dinter and A. Bracher, Assessing bio-physical feedbacks in the shelf areas of Laptev Sea, 2nd $(AC)^3$ Science Conference on Arctic Amplification, Bremerhaven, Germany, 12 November – 14 November 2018.
2. S. N. Losa, M. A. Soppa, V. Pefanis, M. Losch, B. Heim, J. Oelker, S. Dutkiewicz, T. Dinter, V.V. Rozanov, and A. Bracher, Modeling the Arctic coloured dissolved organic matter (CDOM) and phytoplankton diversity in/with support to/from satellite retrievals, FAMOS Annual Meeting, Bergen (Norway), 23 October – 26 October 2018.
3. S. N. Losa, J. Oelker, M. A. Soppa, M. Losch, S. Dutkiewicz, T. Dinter, A. Richter, V. V. Rozanov, J. P. Burrows and A. Bracher, Investigating the phytoplankton diversity in the Great Calcite Belt: perspective from modelling and satellite retrievals, Ocean Optics Conference XXIV, Dubrovnik (Croatia), 7 October – 12 October 2018.
4. V. Pefanis, M. A. Soppa, S. Hellmann, J. Hoelemann, M. Janout, F. Martynov, B. Heim, V. Rozanov, S. Losa, T. Dinter and A. Bracher, First steps towards assessing the radiation budget in the shelf areas of the Laptev Sea by remote sensing and radiative transfer modelling, 15th International Circumpolar Remote Sensing Symposium, Potsdam, Germany, 10 September – 14 September 2018.
5. S. N. Losa, M. A. Soppa, V. Pefanis, M. Losch, B. Heim, J. Oelker, S. Dutkiewicz, T. Dinter, V. V. Rozanov and A. Bracher, Modeling the Arctic coloured dissolved organic matter (CDOM) and phytoplankton diversity in/with support to satellite retrievals, REKLIM Workshop, Boppard (Germany), 15 May – 17 May 2018.
6. S. N. Losa, J. Oelker, M. A. Soppa, M. Losch, S. Dutkiewicz, T. Dinter, A. Richter, V. V. Rozanov, J. P. Burrows and A. Bracher, The Southern Ocean phytoplankton diversity from space and numerical modelling, 27. Internationale Polartagung, Rostock, 25 March - 29 March 2018.

References

1. Deppeler S. L. and Davidson A. T. (2017). Southern Ocean Phytoplankton in a Changing Climate. Front. Mar. Sci. 4:40. doi: 10.3389/fmars.2017.00040.
2. Dutkiewicz, S., Hickman, A. E., Jahn, O., Gregg, W. W., C. B. Mouw, C. B., and M. J. Follows (2015) Capturing optically important constituents and properties in a marine biogeochemical and ecosystem model Biogeosciences, 12, 4447–4481.
3. Gonçalves-Araujo, R., Stedmon, C. A., Heim, B., Dubinenkov, I., Kraberg, A., Moiseev, D. and Bracher, A. (2015) From Fresh to Marine Waters: Characterization and Fate of Dissolved Organic Matter in the Lena River Delta Region, Siberia, Front. Mar. Sci., 2, 108, doi:10.3389/fmars.2015.00108.
4. Gonçalves-Araujo, R., Granskog, M. A., Bracher, A., Azetsu-Scott, K., Dodd, P. A. and Stedmon, C. A. (2016) Using fluorescent dissolved organic matter to trace and distinguish the origin of Arctic surface waters, Sci. Rep., 6, 33978, doi:10.1038/srep33978.
5. Liu, Y., Boss, E., Chase, A., Xi, H., Zhang, X., Röttgers, R., Pan, Y. and Bracher, A. (2019): Retrieval of Phytoplankton Pigments from Underway Spectrophotometry in the Fram Strait, Remote Sensing. doi: 10.3390/rs11030318.
6. Liu, Y., Röttgers, R., Ramírez-Pérez, M., Dinter, T., Steinmetz, F., Nöthig, E. M., Hellmann, S., Wiegmann, S. and Bracher, A. (2018): Underway spectrophotometry in the Fram Strait (European Arctic Ocean): a highly resolved chlorophyll a data source for complementing satellite ocean color, Optics Express. doi: 10.1364/OE.26.00A678.
7. Losa, S. N., Soppa, M. A., Dinter, T., Wolanin A., Brewin R. J. W., Bricaud A., Oelker, J., Peeken I., Gentili B., Rozanov V. V., Bracher, A. (2017). Synergistic exploitation of hyper- and multispectral Sentinel measurements to determine Phytoplankton Functional Types (SynSenPFT), *Frontiers in Marine Science,* 4, 203. Doi: 10.3389/fmars.2017.00203.
8. Menemenlis, D., Campin, J.-M., Heimbach, P., Hill, C., Lee, T., Nguyen, A., Schodlock, M., and H. Zhang (2008). High resolution global ocean and sea ice data synthesis (2008) Mercator Ocean Quartely Newsletter, 31, 13–21.
9. MITgcm Group (2012), MITgcm Manual, Online documentation, MIT/EAPS, Cambridge, MA 02139, USA.
10. Smith et al. (2017) The influence of the environmental variability on the biogeography of coccolithophores and diatoms in the Great Calcite Belt, Biogeosciences, 14, 4905–4925 and diatoms in the Great Calcite Belt, Biogeosciences, 14, 4905–4925.
11. Soppa, M. A., Hirata, T., Silva, B., Dinter, T., Peeken, I., Wiegmann, S., Bracher, A. (2014) Global Retrieval of Diatom Abundance Based on Phytoplankton Pigments and Satellite Data. Remote Sensing, 6(10), 10089–10106.
12. Soppa, M. A., Peeken, I., and Bracher, A. (2017). Global chlorophyll “a” concentration for diatoms, haptophytes and prokaryotes obtained with the Diagnostic Pigment Analysis of HPLC data compiled from several databases and individual cruises. doi:10.1594/PANGAEA.875879
13. Soppa, M. A., Pefanis, V., Hellmann, S., Losa, S. N., Hölemann, J., Martynov, F., Heim, B., Janout, M. A., Dinter, T., Rozanov, V., Bracher, A. (2019). Assessing the Influence of Water Constituents on the Radiative Heating of the Laptev Sea Schelf Waters, *Frontiers in Marine Science,* (in revision).
14. Soppa, M., Völker, C. and Bracher, A. (2016): Diatom Phenology in the Southern Ocean: Mean Patterns, Trends and the Role of Climate Oscillations, Remote Sensing, 8 (420), pp. 1–17.
15. Tréguer, P., Bowler, C., Moriceau, B., Dutkiewicz, S., Gehlen, M., Aumont, O., Bittner, L., Dugdale, R., Finkel, Z., Iudicone, D., Jahn, O., Guidi, L., Lasbleiz, M., Leblanc, K., Levy, M., Pondaven, P. (2018) Influence of diatom diversity on the ocean biological carbon pump, Nature Geoscience, II (1): 27–37, doi: 10.1038/s41561-017-0028-x.

6.15 *hbk00059:* Joint state-parameter estimation for the Last Glacial Maximum with CESM1.2

HLRNProject ID:	hb00059
Run time:	05/2017 – 02/2019
Project Leader:	Prof. Dr. M. Schulz
ProjectScientists:	J. García-Pintado
Affiliation:	Fachbereich Geowissenschaften, MARUM – Zentrum für Marine Umweltwissenschaften, Universität Bremen

Overview

The PALMOD project, funded by BMBF, seeks to understand climate system dynamics and variability during the last glacial cycle. Specific topics are: i) to identify and quantify the relative contributions of the fundamental processes which determined the Earth's climate trajectory and variability during the last glacial cycle, ii) to simulate with comprehensive Earth System Models (ESMs) the climate from the peak of the last interglacial (the Eemian warm period) up to the present, including the changes in the spectrum of variability, and iii) to assess possible future climate trajectories beyond this century during the next millennia with sophisticated ESMs tested in such a way.

Relevant to this computing project proposal, an expected major outcome of the first (4-yr) phase of PALMOD is to obtain a comprehensive data synthesis of paleoclimatic conditions during the last glacial cycle, associated with explicit estimates of uncertainty. This involves combining in the best possible ways the outcome of long-term climate model simulations with the last generation of multi paleo proxy data (planktic foraminifera, diatoms, dinoflagellates, radiolaria, geochemical proxies as Mg/Ca in planktic foraminifera shells, etc.). For this, we are using a global climate model; the Community Earth System Model version 1.2 (CESM1.2), and assimilating homogenized multi-proxy observations, generated within the scope of PALMOD, into CESM. Ensemble reconstructions from the coupled model at the Last Glacial Maximum (LGM) are being analysed along with a transient higher resolution simulation of the post LGM-deglaciation.

Results

In the previous year, we set up an assimilation scheme and conducted analysis of tropical coral d18O and Sr/Ca for preindustrial conditions and synthetic analysis based on LGM pseudo-proxy observations of SST derived from the MARGO multiproxy database, in preparation for the coming PalMod compilation of marine and terrestrial proxy observations. García-Pintado and Paul (2018), supported by computations in HLRN-III, summarises some work regarding the synthetic analyses. Overall, the sensitivity analyses were extremely useful to rank a number of key uncertain parameters in the coupled climate model, which are not sufficiently constrained by modern observations (past climates are an extrapolation situation under which current parameter have not been tested), and so to guide decisions regarding the selection of control variables for the coming LGM analyses. Also, the analysis of tropical coral, calibrated against HadISST, illustrated some of the problems in relation with the sparsity of the datasets and on the model-data comparison approaches, which are a stumbling stone for the assimilation of paleoclimate proxy observations. It is clear that from a local point of view strong nonlinear sensitivities appear and hamper linear approaches to data assimilation. An example is depicted in Figure 1, which shows a strong nonlinear

relationship between SST at an observation location in the North Atlantic and a global parameter controlling low cloud formation as a function of moisture. While this may be seen as an extreme case, it is not unique and illustrates the issue of nonlinearity when combined with the issue of sparsity in the observational dataset. This calls for specific quality control design and reconsideration of the model-data comparison for paleoclimate analyses.

As summarized in the caption of Figure 1, in this case, the strongest factor in the nonlinear relation actually results from a southward movement of the North Atlantic subpolar. This does not necessarily mean that there is a substantial change of regime. However, in addition to these situations, strong transitions appear for some model configurations, which (at the view of more recent experiments in HLRN-IV) indicate, e.g., that a bistable AMOC is possible with this model. The implications for the resulting modeled climate are huge. Moreover, a “low AMOC” regime is shown as a strong atractor, in which the model sensitivity to certain parameters for the model physics is negligible as compared with the corresponding sensitivities for a “strong AMOC” regime. Also, recent simulations in HLRN-IV confirm that integration times of ~1000 year are needed to have a reasonable trust in the sensitivity estimation. Other example of the conducted experiment is shown in Figure 2, where the finite difference sensitivity iterated Kalman smoother (FDS-IKS, as described in García-Pintado and Paul, 2018) is evaluated versus an (spherical simplex) ensemble transform Kalman filter (ETKF). In this case, the bias reduction is quantitatively similar, but the computational cost is substantially lower for the FDS-IKS.

On the other hand, in the new HLRN-IV, in addition to the former standard CESM model, we have now successfully configured the isotope-enabled CESM1.2 (iCESM), and conducted a battery of throughput analysis with several configurations of the iCESM, including water isotopes and carbon isotopes. Initial tests for preindustrial conditions have now been conducted and are under evaluation.

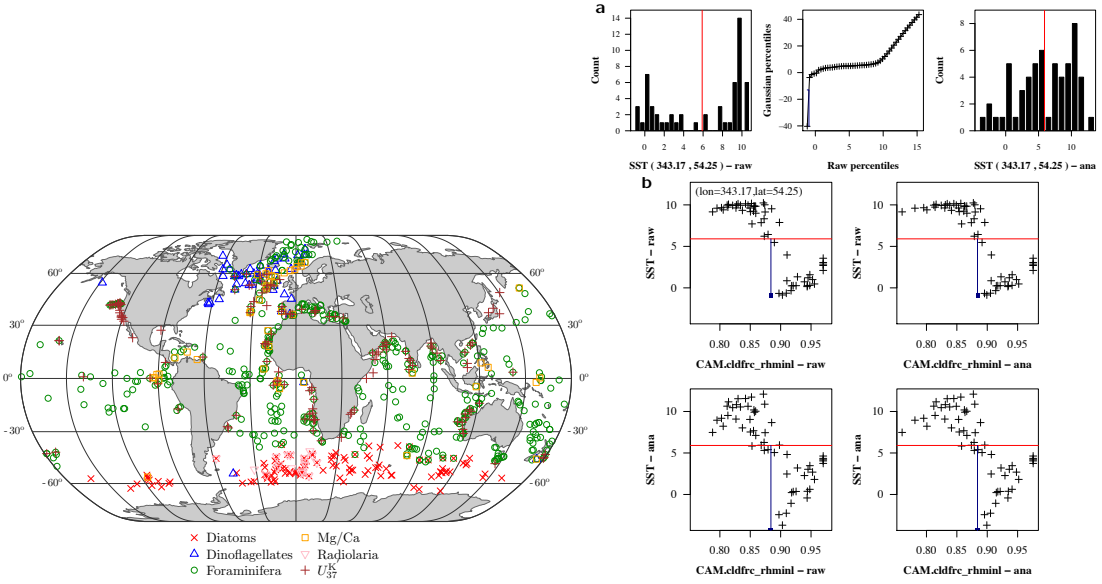

Fig. 1: Distribution of MARGO paleoclimate proxy observations for LGM, and one example of strong nonlinear relation between SST at a location in the North Atlantic and the global threshold in moisture for low cloud formation. A southward displacement of the North Atlantic subpolar front as this threshold increases creates the strong negative jump at the observation location, contrasting with the otherwise positive sensitivity of SST to this parameter at the site. The location corresponding to the scaterplots is shown by a triangle in the North Atlantic in Figure 2.

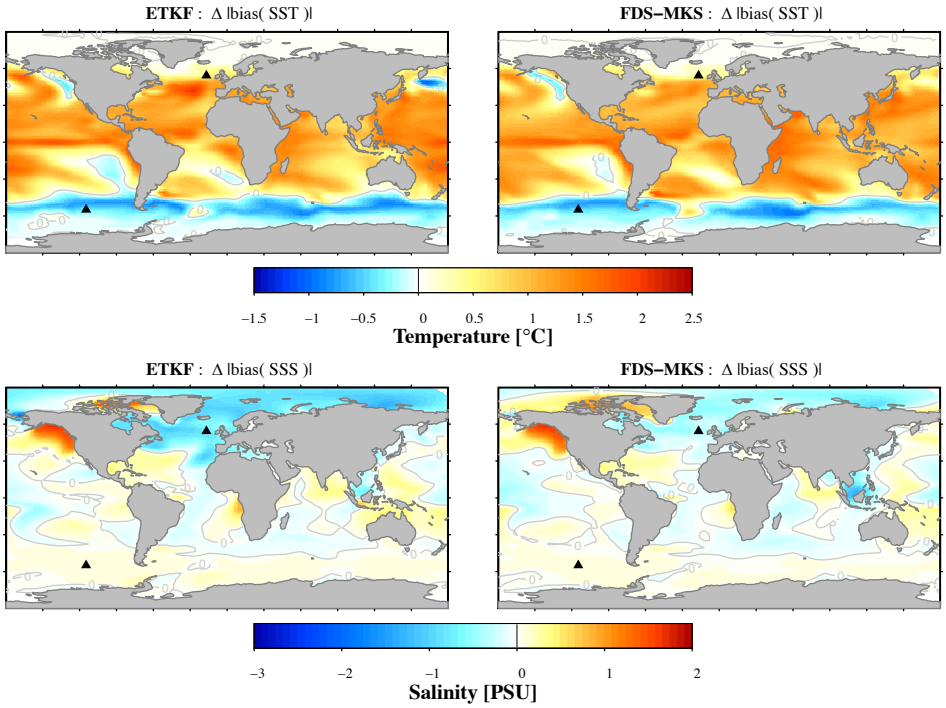

Fig. 2: Absolute bias reduction for an Ensemble TranformKalman Filter (ETKF) and the finite differenced sensitivity iterated Kalman smoother (FDS-IKS) for a synthetic test and preindustrial climate. The shown variables are sea surface temperature (SST) and sea surface salinity (SSS). The statistics are the absolute bias between the background and the truth minus the absolute bias between theanalysis and the truth. Thus, positive values are a net bias reduction. Isolines at value 0 shown in grey

Outlook

We are in the process of setting up initial conditions, including the water isotopes and carbon isotopes for the equilibrium simulation at LGM. The isotope-enabled CESM simulations will be conducted for preindustrial conditions and LGM in first instance. In addition, simulations with the atmospheric component (iCAM5) forced by gridded boundary conditions for SST and sea ice are also under preparation. Results will be intercompared, within the framework of PalMod, with results from the model MPI-ESM-wiso (conducted by collaborators in AWI), and analysed with the new proxy compilations processed within PalMod by other groups.

Publications

1. J. García-Pintado, A. Paul, *Evaluation of iterative Kalman smoother schemes for multi-decadal past climate analysis with comprehensive Earth system models,* Geoscientific Model Development*, 11, 5051-5084 (2018)*

Presentations

1. J. García-Pintado, B. Fallah, T. Felis, J. Zinke, M. Pfeiffer, A. Paul., Exploring coral data for multi-decadal paleoclimate reanalysis with the Community Earth System Model, EGU, Vienna, 11 April, 2018

6.16 hbk00060: North Pacific Ocean circulation and biogeochemistry in warming climate since the Last Glacial Maximum

HLRN Project ID:	hbk00060
Run time:	III/2017 – IV/2018
Full project time:	08.2017 – 07.2020
Project Leader:	Prof. G. Lohmann
Project Scientists:	Dr. X. Gong, Dr. P. Scholz, Dr. V. Schourup-Kristensen, Dr. L. Lembke-Jene, Prof. Dr. R. Tiedemann
Affiliation:	Alfred Wegener Institute Helmholtz Center for Polar and Marine Research, Bremerhaven, Germany IUP, University Bremen, Bremen, Germany

Overview

North Pacific Ocean develops the Earth climate system not only by influencing oceanic water mass and heat distributions, but also via changing global carbon cycle. Observations have characterized the subarctic Pacific as a region where atmospheric CO_2 sinks into oceans most effectively against the on-gonging global warming and CO_2 rise in the atmosphere, besides that in the Southern Ocean. Mechanically, North Pacific functions its 'soft-tissue' role via processes of unique features compared to the Southern Ocean. Specifically, blooming of primary productivity brings carbon into the subarctic Pacific and its marginal oceans in late Spring and Summer, while the winter process of North Pacific ventilation uplifts dissolved inorganic carbon (DIC) from intermediate depths into the surface oceanfor a CO_2 release into atmosphere. Overall, the interplay between physical and biogeochemical processes among seasons determines annual-mean budget and efficiency of the North Pacific in controlling global carbon system. Therefore, to characterize the physical and biogeochemical features within their coupled system is key to develop further understanding about the North Pacific roles in Earth climate and carbon systems.

In this project, we aim to understand physical processes of the North Pacific overturning and its control on coeval biogeochemical processes. Besides the modern climate state, we also extend our focus on the North Pacific system on the basis of the several climates since the Last Glacial Maximum (LGM), ~23,000 - 18,000 years before present (yrs B.P.), including: Mid Holocene (MH, 6,000 yrs B.P.), Early Holocene (EH, 9,000 yrs B.P.) and the LGM. Our simulations of the North Pacific in different climates afford possibility in discussing potential nonlinear behaviour in North Pacific overturning and the resultant biogeochemical characteristics that may decouples from the background ocean physics.Specifically, we focus on the following scientific questions: (1) the dependence of the North Pacific Ocean stratification on the background climate states; (2) the control of the North Pacific overturning on marine primary productivity, remineralization and mid-depth anoxia; (3) regulation of biological vs. physical carbon pump in subarctic Pacific Ocean.

According to our scientific targets, we will use the standalone ocean model Finite Element Sea Ice–Ocean Model (FESOM) and the coupled ocean-sea ice-biogeochemical FESOM-REcoM model to simulate Present-Day (PD) and the 3 paleo oceans of MH, EH and LGM. Concerning the simulation resource and computing time, our modelling task in this project

are divided to two parts: Firstly, to run the stand-alone FESOM model to quasi-equilibrium states for each proposed climate. Second, on the basis of the FESOM-simulated, quasi-equilibrium ocean, to utilize and run the coupled ocean-sea ice-biogeochemical FESOM-REcoM model.

Strategically, our project correlates to the BMBF project: *"WTZ China–NOPAWAC-North Pacific Ocean in Warming Climates During the Quaternary"* (01.08.2017 - 31.07.2020). In addition, our work in this project succeeds from our previous HLRN projects, including 'Climatic evolution in the marginal seas of the Northwest Pacific Ocean since the last glacial period until present day: changes in the formation of North Pacific Intermediate Water formation and their implications on the Pacific realm' (HLRN project: hbk0042) and 'Glacial-interglacial change of the biogeochemical process in the Pacific subarctic oceans' (HLRN project: hbk0054). In these projects, we have generated and test grid meshes for the modern and glacial oceans, as shown in Fig. 1.

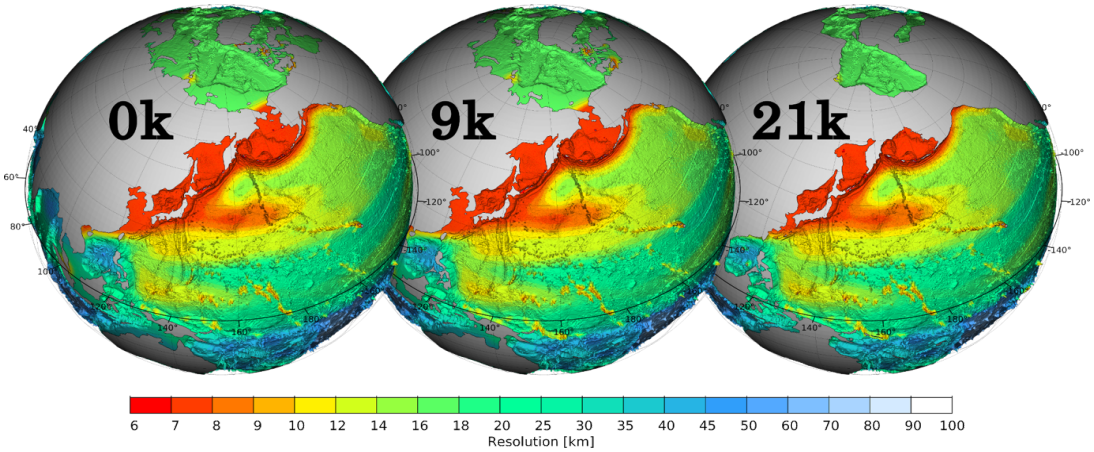

Fig. 1: Mesh resolution of the northwestern Pacific FESOM configuration for time-slice experiments of PDand MHconditions (left), EH (middle), and the LGM (right). In our grid meshes, the up to 6 km resolution is in the NW Pacific and its marginal seas (the Sea of Okhotsk, Sea of Japan and Bering Sea).

Achievements

In year 2018, we mainly focus on continuing the FESOM simulations for PD and LGM states. This will also provide us important experience in understanding the results of MH and EH simulations in the future. In addition, this is also in line with our research (NOWAPAC) and HLRN computing proposals. Specifically, we have achieved the following mile stones:

1. To have finished FESOM experiment of PD with COREII atmospheric forcing by another 4 rounds of ~ 200 model years. In particular, this is important for our modeled ocean to develop features down to intermediate depths (deeper than 1000m). According to our most recent research [Gong et al. 2019], temperatures and salinities at intermediate-depth Pacific Ocean are determinant factors for the North Pacific ventilation and also the calculation of carbon reservoir using FESOM-REcoM model in the future.
2. To have finished the FESOM experiment of LGM by two new rounds, ~120 model years. We have evaluated the LGM experiments with focus on upper ocean (Fig. 2) and a N-S transect at 180E (Fig. 3), as well as its drift from the initial conditions.
3. To have simulated PD ocean to an overturning state with reasonable vertical stratification in the North Pacific, and ready to start FESOM-REcoM simulations.

Our experiments characterize the North Pacific by lower upper-ocean temperatures in the LGM compared to PD conditions generally (Fig. 2). In contrast, Bay of Alaska shows regional heterogeneity of relatively warmer oceans in winter, and thus overall higher temperatures of annual average. This regional feature correlate to higher surface air temperatures in the atmospheric forcing that is simulated by MPI-ESM model.

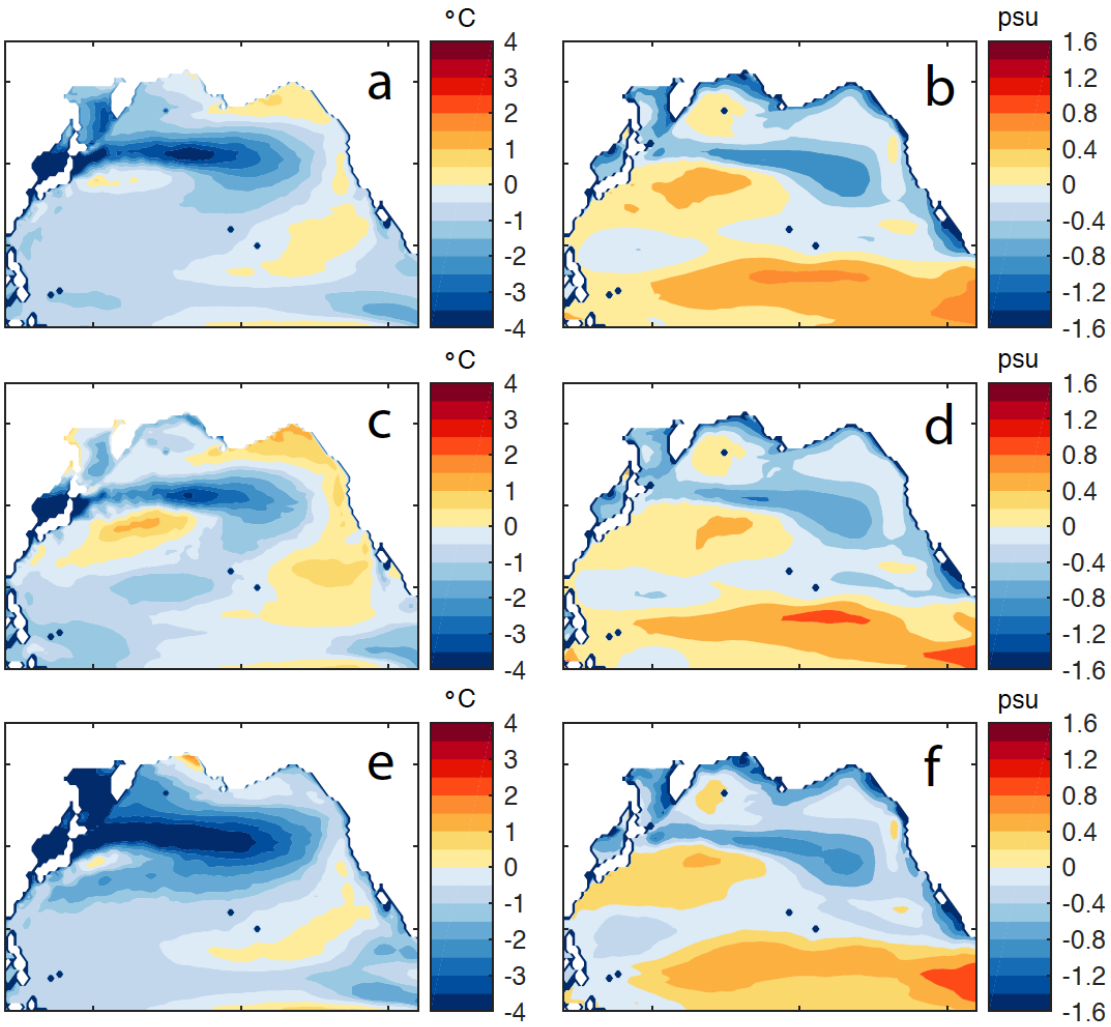

Fig. 2: Modelled 10m ocean temperatures and salinities of LGM to PI conditions by FESOM model. (a-b) Annual mean LGM-to-PD anomalies of temperatures of salinities. (c-d) are for DJF mean, with (e-f) for JJA mean.

Similarly, the warmer Bay of Alaska during LGM is also suggested by our ESM simulation of AWI-CM model (not shown here). On the other hand, this feature requires further discussion by comparing to marine proxy evidences. Moreover, we notice that the warmer Bay of Alaska in our FESOM simulation becomes less pronounced compared to the initial conditions, as shown in Fig. 3a, c and e. Here, our hypotheses are to attribute such offset to either a switch of ocean model from MPIOM to FESOM, higher resolutions in the ocean model or a lack of atmosphere feedbacks in our FESOM standalone experiment. All these possibilities will be tested in the future work by doing sensitivity experiments.

In the upper ocean, our model suggests a larger meridional gradient in salinities during the LGM compared to PD (Fig. 2b, d and f). This is due to coeval weaker Kuroshio Current in the

LGM experiment, also in line with indications by paleoceanographic evidences [Zheng et al. 2017].

Our PD experiment has characterized the North Pacific Intermediate water by a cold and low-salinity tongue extending from subarctic Pacific to low latitudes at the S-N transect of 180E (Fig. 4), which isquantitively comparable with WOA dataset. Here, with respect to the vertical stratification state, our FESOM stand-alone experiment has generated a modern ocean state ready to conduct the coupled FESOM-REcoM experiment.

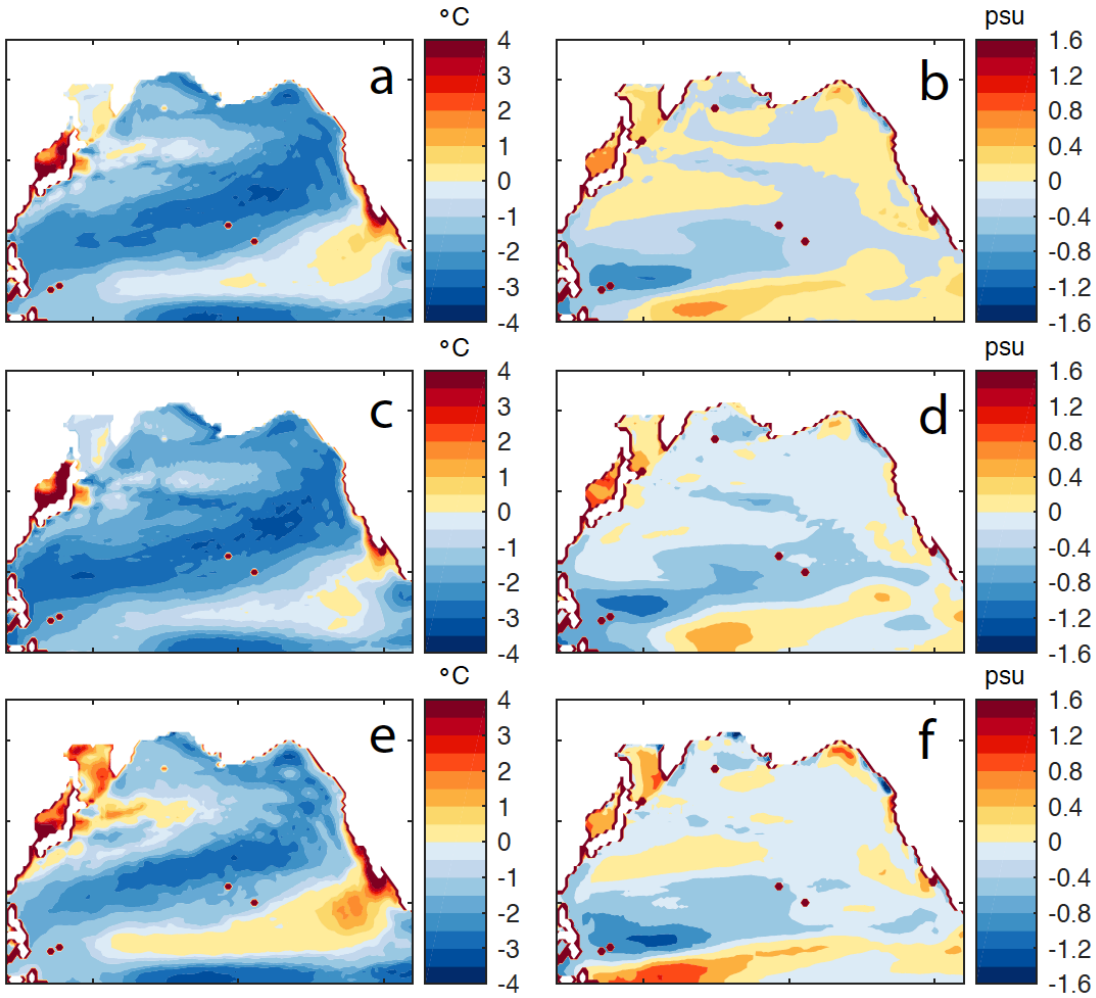

Fig. 3: Modeled offset of LGM ocean temperatures and salinities by FESOM compared to the initial conditions that stem from the MPI-ESM experiment. (a-b) Annual mean offsets for 10m temperatures and salinities, respectively. (c-d) are for DJF mean, with (e-f) for JJA mean.

In comparison, our LGM experiment suggested a stronger stratification between surface and intermediate ocean (Fig. 4f). This is different from the LGM oceans that are used to initiate the FESOM LGM experiment. On the other hand, the FESOM experiment after the 120 model years show higher surface salinities in the Okhotsk Sea compared to the initial values, thus of potential to weaken the stratification and enhance regional convection. At this point, we plan to continue the FESOM LGM simulation for another 120 years, and then check the change in vertical stratification.

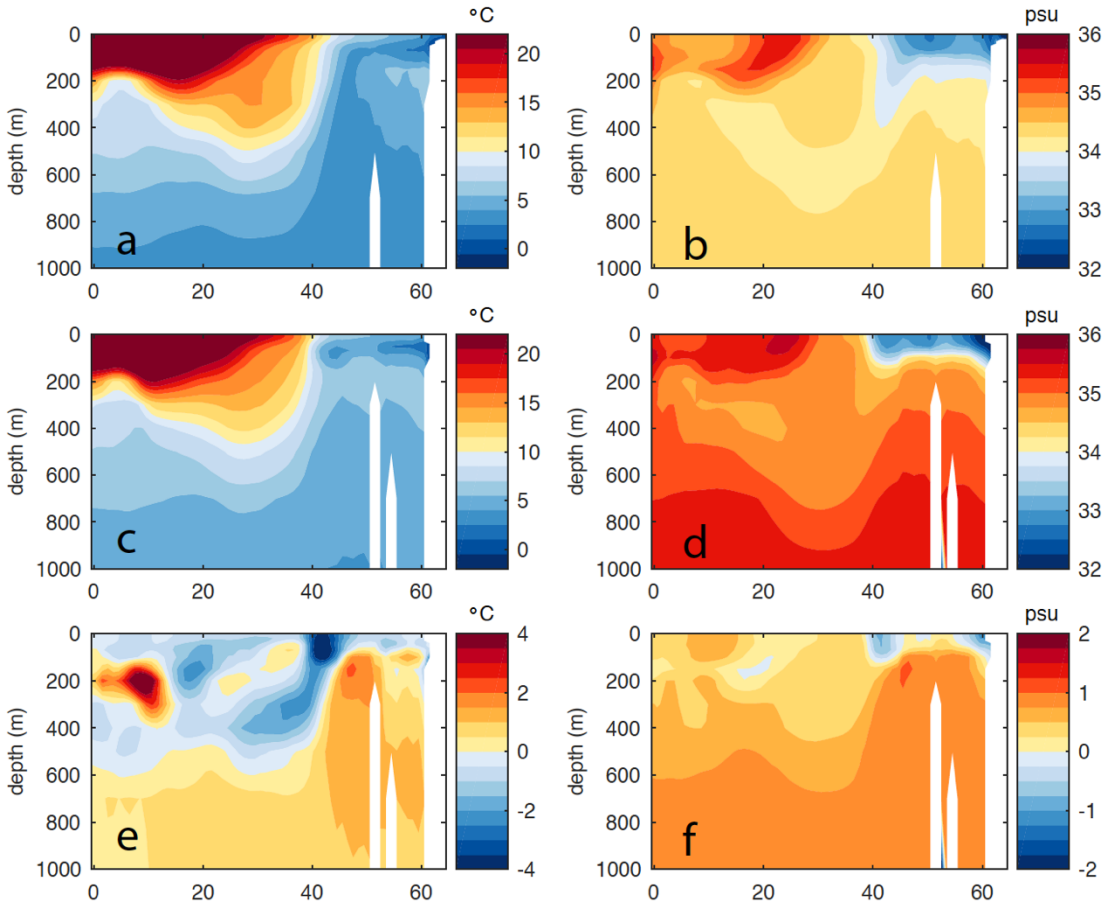

Fig. 4: Modelled temperature and salinity at 180E transect in PD and LGM oceans by FESOM model. (a-b) show PD transect of temperature and salinities, respectively, with (c-d) for the LGM experiment. (e-f) show the modelled anomalies of LGM to PD conditions.

Perspective of continuation in a following HLRN project

Seceding from our results, our work next step will focus on the following directions:

1. Further analysis to understand the results of the finished simulations.
2. Set up of sensitivity experiment to test the impact of the lack of 'atmosphere-ocean' coupled system in drifting our high-resolution simulations under the PD and LGM conditions.
3. To continue the stand-alone FESOM experiment MH, EH and LGM.
4. To start the FESOM-REcoM experiment for PD conditions.

To finish the following simulation work, we will consider continuing our application to HLRN about computing resource until the end of the BMBF project: *"WTZ China–NOPAWAC-North Pacific Ocean in Warming Climates During the Quaternary"* (01.08.2017 - 31.07.2020).

References

Gong et al. Enhanced North Pacific deep-ocean stratification by stronger intermediate water formation during Heinrich Stadial 1, Nature Communications 10 (2019).

Zheng, X., et al. Synchronicity of Kuroshio Current and climate system variability since the Last Glacial Maximum. Earth and Planetary Science Letters 452 (2016).

6.17 *hbk00061:* Combining ocean models and proxy data

HLRN Project ID:	hbk00061
Run time:	III/2017 – II/2019
Project Leader:	Prof. Michael Schulz
Project Scientist:	Charlotte Breitkreuz
Affiliation:	MARUM – Center for Marine Environmental Sciences and Faculty of Geosciences, University of Bremen

Overview

This project is part of the National Climate Modeling Initiative PalMod. The overarching goal of PalMod is to simulate the complete last glacial cycle, that is, the past 120 thousand years, with comprehensive Earth-system models. Understanding past climate states is essential for predicting future climate change and validating climate models by applying them to climate states that were very different from today is important to deepen our trust in models and hence, in their projections for future climate.

Our project focuses on the development and application of a data assimilation (DA) method to estimate the state of the ocean during the Last Glacial Maximum (LGM, 19-23 thousand years ago) with ocean general circulation model and proxy data. The LGM was the last time during the Earth's history when the climate was substantially different from today, but remained relatively stable for a few thousand years. The large-scale patterns of the ocean circulation during this time remain uncertain. Reconstructions from proxy data as well as from modeling studies have large uncertainties and different studies show a broad range of possibilities of the ocean state during that time interval. Uncertainties in paleo-climate modeling originate, for example, from uncertain boundary conditions, uncertainties in model parameters, and other model errors. Proxy data, on the other hand, have uncertainties regarding the imprint of the climate signal in the proxy, disturbances during the deposition, and measurement errors. Combining climate models with proxy data and their respective uncertainties via DA is a powerful means to obtain more reliable estimates of past climate states.

The DA method in this project aims at optimizing uncertain model parameters and boundary conditions including the atmospheric forcing of the ocean, such as precipitation and air temperature. A successful estimate is consistent with the physics incorporated in the model and with the proxy data within their respective uncertainties. Data assimilation is frequently used in the field of weather forecasting, but it is still not well-established in the community of paleoclimatology because available proxy data is very sparse and comprehensive data sets of past climate states have only become available in the past years.

Methods

We employ the Massachusetts Institute of Technology general circulation model (MITgcm), a coupled ocean-sea ice general circulation model. The model uses a cubed-sphere grid with 192 x 32 horizontal grid cells, resulting in a resolution of about 285 km, and 15 vertical levels. The low resolution of the model enables us to perform long equilibrium simulations, running about 2,000 model years to a quasi-steady state. The MITgcm is enhanced with a water isotope module (Völpel et al., 2017) that gives us the possibility to simulate the oxygen isotopic ratio of seawater ($\delta^{18}O_{sw}$) in the whole water column.

A recent state estimate of the LGM ocean was obtained by Kurahashi-Nakamura et al. (2017) with the adjoint method. The method requires the adjoint of the model code, which can be obtained by "automatic differentiation". However, this approach is not applicable to many models. Moreover, the adjoint method does not readily provide an uncertainty estimate of the solution and it is computationally very expensive. We, therefore, aim at developing an efficient DA method that provides an uncertainty estimate and that is independent of the existence of an adjoint, such that it can be applied with other, more expensive models.

To that end, we combine a state reduction approach with a finite difference sensitivity-iterative Kalman smoother (FDS-IKS, García-Pintado and Paul, 2018) to estimate the spatially varying atmospheric forcing fields. The state reduction approach enables us to estimate the spatially varying atmospheric forcing by only estimating a number of parameters at the order of 10^1. The FDS-IKS is based on the iterative Kalman smoother (Bell, 1994) and uses an approximation of the tangent linear derivative of the model through finite difference sensitivities obtained from perturbation experiments.

Results

We tested the approach by applying it to pseudo-proxy data generated from target model simulations and estimating 16 parameters in air temperature, precipitation, and isotopic composition of precipitation and water vapor. The data were sampled from the target model simulation at locations where data is available for the LGM and an error was added to the data to include the uncertainty that is present in LGM proxy data. Our results demonstrate that the method is capable of efficiently reducing the model-data misfit and reconstructing the target ocean circulation.

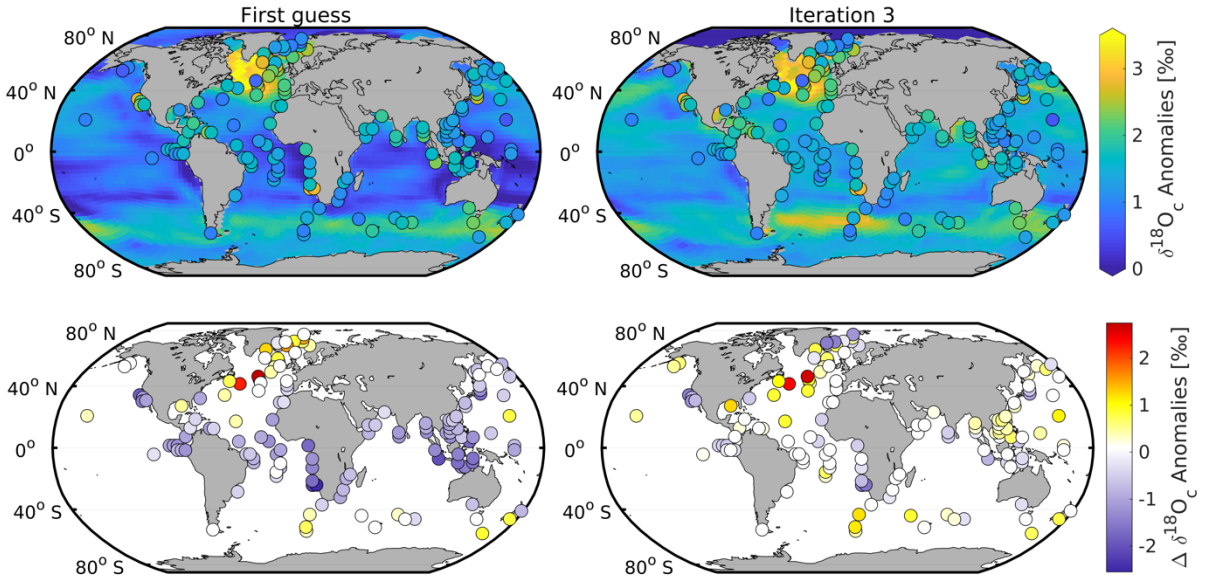

Fig. 1: Simulated 100-year mean surface field (0–50 m) of $\delta^{18}O_c$ LGM-Late Holocene anomalies in the first guess and LGM optimization (iteration 3) and assimilated planktic $\delta^{18}O_c$ anomaly data (upper panels), and respective model-data differences (lower panels). Differences smaller than the uncertainty of the observational data are displayed in white.

We additionally applied the method to estimate the state of the LGM ocean. To constrain the LGM estimate, we used global data on the oxygen isotopic composition of calcite ($\delta^{18}O_c$) and a global sea surface temperature reconstruction (MARGO Project members, 2009). The model-data misfit is greatly reduced within the first three iterations (Figure 1), but some model-data misfit remains for the planktic and benthic $\delta^{18}O_c$ data (Figures 1 and 2). The estimated LGM ocean state shows a shallower North Atlantic Deep Water (Figure 2, lower panel) compared to today coinciding well with previous estimates (e.g., Lynch-Stieglitz et al., 2007).

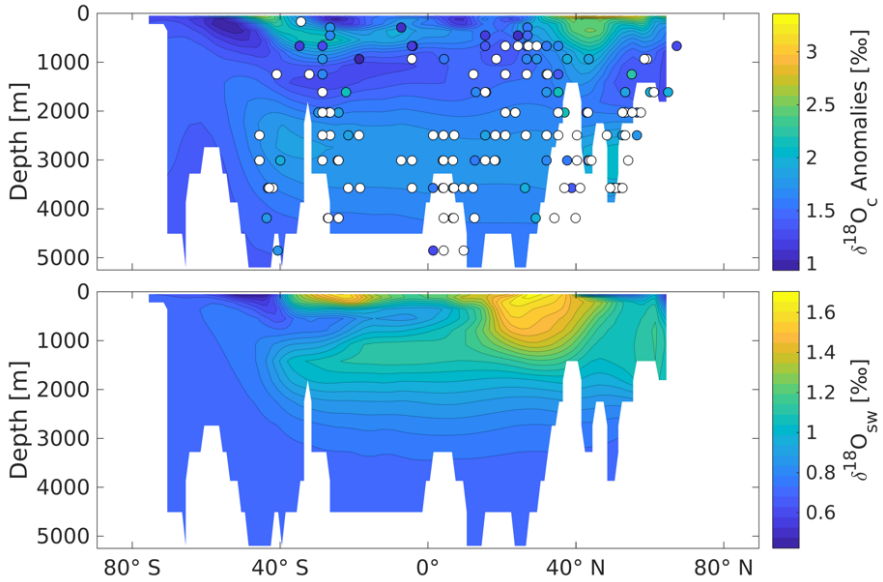

Fig. 2: Simulated 100-year mean $\delta^{18}O_c$ LGM-Late Holocene anomalies (upper panel) and simulated 100-year mean $\delta^{18}O_{sw}$ at a vertical transect through the Atlantic Ocean at 32.5° W in the LGM optimization (iteration 3) and assimilated benthic δ18Oc anomalydata. Data points where the model agrees with the observational data within their respective uncertainties are displayed in white.

Publications

1. C. Breitkreuz, A. Paul, S. Multiza, M. Schulz, *An efficient Kalman smoother method and state reduction approach for (paleo-)ocean state estimation* (submitted to Geoscientific Model Development).

Presentations

- C. Breitkreuz, A. Paul, P. J. van Leeuwen, M. Schulz, *A new particle filter method to estimate the state of the ocean during the Last Glacial Maximum,* Poster at EGU General Assembly, April 2018, Vienna.

- C. Breitkreuz, A. Paul, J. García-Pintado, M. Schulz, *Using data assimilation to estimate the global ocean state during the Last Glacial Maximum,* Poster at the 3 Cluster Conference, October 2018, Berlin.

References

Bell, B. M.: The iterated Kalman smoother as a Gauss–Newton method, SIAM Journal on Optimization, 4, 626–636, 1994.

García-Pintado, J. and Paul, A.: Evaluation of iterative Kalman smoother schemes for multi-decadal past climate analysis with comprehensive Earth system models, Geoscientific Model Development, 11, 5051–5084, 2018.

Kurahashi-Nakamura, T., Paul, A., and Losch, M. Dynamical reconstruction of the global ocean state during the Last Glacial Maximum. Paleoceanography, 32(4):326–350, 2017.

Lynch-Stieglitz, J., Adkins, J. F., Curry, W. B., Dokken, T., Hall, I. R., Herguera, J. C., Hirschi, J. J.-M., Ivanova, E. V., Kissel, C., Marchal, O., et al.: Atlantic meridional overturning circulation during the Last Glacial Maximum, Science, 316, 66–69, 2007.

MARGO Project Members. Constraints on the magnitude and patterns of ocean cooling at the last glacial maximum. Nature Geoscience, 2(2):127–132, 2009.

Völpel, R., André, P., Krandick, A., Mulitza, S., and Schulz, M. Stable water isotopes in the MITgcm. Geoscientific Model Development, 10(8):3125, 2017.

6.18 **hbk00062*:* Retrieval of stratospheric ozone profiles from OMPS observations in limb geometry**

HLRN Project ID:	hbk00062
Run time:	IV/2017 – III/2019
Project Leader:	Dr. Alexei Rozanov
Project Scientists:	C. Arosio
Affiliation:	Institute of Environmental Physics, University of Bremen

Overview

Stratospheric ozone recovery is expected by model studies (Eyring et al. 2010), as a consequence of the decreasing emission of chlorine-containing ozone depleting substances (ODSs) and the increasing concentration of CO_2. ODSs are involved in catalytic cycles which contribute to ozone destruction, while the increasing CO_2 leads to a cooling of the stratosphere, reducing the efficiency of some temperature-dependent ozone depleting reactions.

To monitor the status of the ozone layer and the onset of its recovery, satellite measurements are an important tool, as they provide observations with high temporal and spatial resolution. In particular, measurements in limb geometry, as performed by SCIAMACHY (SCanning Imaging Absorption spectroMeter for Atmospheric Chartography) and OMPS-LP (Ozone Mapping and Profiler Suite – Limb Profiler), enable the study of ozone profiles with a vertical resolution of about 3 km. However, single satellite missions are generally too short to assess long-term ozone changes and a merging of several time series is therefore required.

Several studies addressed the analysis of stratospheric ozone trends over the last decades, for example Harris et al. 2015, Sofieva et al. 2017 and Steinbrecht et al. 2017. The authors found a large variability between data sets. However, they detected positive trends in the upper stratosphere, particularly at mid-latitudes, a hint of the ozone recovery. In the lower stratosphere, where a decrease in ozone concentration is expected due to the speed-up of the tropical upwelling, results are still affected by a large uncertainty and the observation of negative trends are still disputed.

In this framework, the main aim of this project is the retrieval of ozone profiles from OMPS-LPobservations, from the beginning of 2012 till present. The radiative transfer model and spectroscopic data bases are the same used for the retrieval of SCIAMACHY ozone profiles. The retrieval approach is also similar, in order to minimize systematic biases between the two time series. Once OMPS-LP ozone profiles are retrieved and validated, the second goal is the merging with the SCIAMACHY time series, to study altitude, latitude and longitude resolved ozone changes over the last 15 years.

Results

A first complete retrieval of OMPS-LP time series (from February 2012 to December 2018) has been performed.

To check the quality of the data set, we validated the ozone profiles against ozonesondes measurements, particularly valuable in the lower stratosphere up to 30 km. The high vertically-resolved observations from sondes had first to be convolved with the averaging

kernels of the retrieval, to be comparable with lower resolution satellite observations. Fig. 1 shows the results of the comparison in terms of relative differences between sondes and OMPS-LP profiles in several latitude bands, averaged over the 2012-2018 period. The best performance has been found at northern mid-lattiudes with an agreement within ±3 % between 12 and 28 km. In the tropics a discrepancy above 10 % is visible below 15 km. The small ozone values in the ULTS amplifies the relative difference at these altitudes. In addition, even though we accounted for aerosol and cirrus clouds in the ozone retrieval, they may still affect the retrieval at these altitudes. In the southern hemisphere the comparison is not as good as in the northern hemisphere, but still within ±7 % below 30 km.

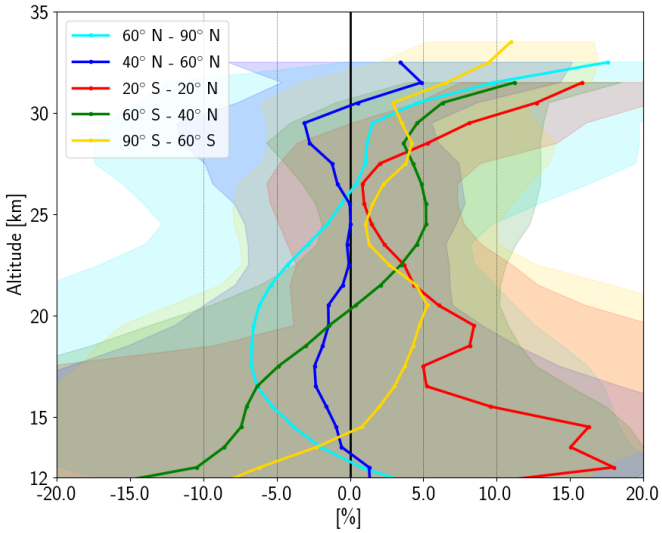

Figure 1: Relative differences between OMPS-LP retrieved ozone profiles and ozonesondes measurements in 5 latitude bands averaged over the 2012-2018 period

The merging with SCIAMACHY time series was performed using MLS (Microwave Limb Sounder) observations as a transfer function. SCIAMACHY and OMPS missions have an overlap of only 2 months, not sufficient to remove the bias between the two instruments. Merging the two data sets, we obtained an ozone time series starting from 2003, vertically resolved every 3.3 km. Spatially, we binned the profiles every 5° latitude and 20° longitude, enabling the study of longitudinally resolved structures and changes in the ozone distribution.

A multi-linear regression model, accounding for several phenomena which affect the ozone distribution, like the Quasi Biennial Oscillation, Solar activity and El Nino, have been applied. Results are reported in Fig. 2: on the left panel zonally averaged trends over the 2003-2018 period are shown. Significant trends correspond to non-dashed areas and were mainly found at mid-latitudes in the middle upper stratosphere, with the highest values in the northern hemisphere. In the lower tropical stratosphere, negative but not significant trends were detected. In panel (b) of this figure, the longitudinally resolved structure is displayed at 38 km, where a lage variability was found: positive values overe the Candian sector and small non-significant values over Siberia. The assessment of the stability and reliability of these longitudinal structures is still ongoing.

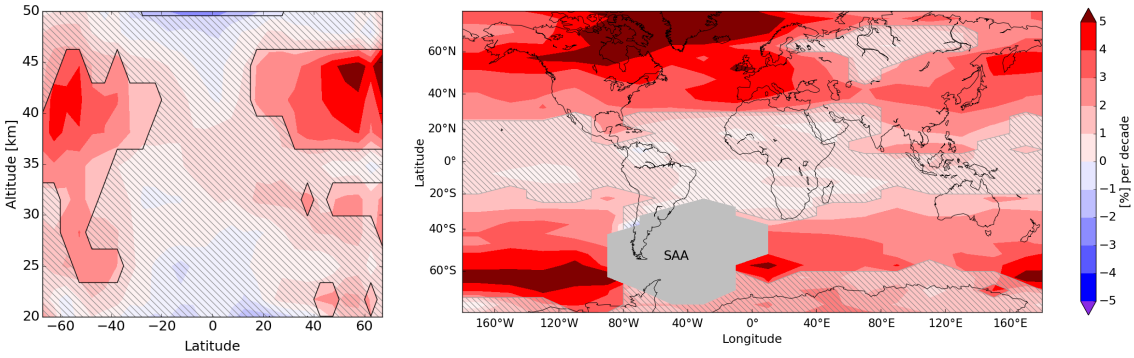

Figure 2: Long-term ozone changes over the 2003-2017 period: in left panel the zonally averaged trends, in the right panel longitudinally resolved results at the altitude of 38 km. Shaded areas indicate non-significant trends.

In the tropical middle stratosphere over the last 15 years, a fluctuation of the trend has been found, from negative values until 2011 to positive values from 2011. The causes behind this change are still under investigations. Galytska et al. 2019 studied the long-terms changes over SCIAMACHY period and related the positive trend around 35 km in the tropics to dynamical changes: the vertical transport was found to speed up during winter months, causing a change in the residence time of NO_2, which in turns affects ozone concentration in this region.

Outlook

An improvement of the ozone retrieval is planned, including also a retrieval of polar mesospheric clouds (PMC). Currently, profiles affected by the presence of a PMC in the instrument field of view are screened out.

A comparison with a chemistry transport model is planned to help understanding the changes in ozone distribution over the last 15 years and assess the reliability of the longitude-resolved features that we found in our merged data set.

Publications

1. Arosio, C., et al. "Retrieval of ozone profiles from OMPS limb scattering observations." Atmospheric Measurement Techniques 11.4 (2018): 2135-2149.
2. Arosio, C., et al. “Merging of ozone profiles from SCIAMACHY, OMPS and SAGE II observations to study stratospheric ozone changes”, Atmospheric Measurement Techniques Discuss., https://doi.org/10.5194/amt-2018-275, in review, 2018.

Presentations

1. Arosio, C., Rozanov, A., Galytska, E., Chipperfield, M., Dhomse, S., Burrows, J.P.: “*Merging ozone profiles from SCIAMACHY, OMPS-LP and SAGE II observations to study long-term stratospheric ozone changes*”, ATMOS, 26-29 November 2018, Salzburg, Austria.
2. Arosio, C., Rozanov, A., Malinina, E., Burrows, J.P.: “*Merging of stratospheric ozone profiles from OMPS and SCIAMACHY limb observations*”, EGU 2018, 7-12 April 2018, Vienna, Austria

References

Eyring, V., et al. "Multi-model assessment of stratospheric ozone return dates and ozone recovery in CCMVal-2 models."*Atmospheric Chemistry and Physics* 10.19 (2010): 9451-9472.

Galytska, Evgenia, et al. "Dynamically controlled ozone decline in the tropical mid-stratosphere observed by SCIAMACHY."*Atmospheric Chemistry and Physics* 19.2 (2019): 767-783.

Harris, Neil RP, et al. "Past changes in the vertical distribution of ozone–Part 3: Analysis and interpretation of trends."*Atmospheric Chemistry and Physics* 15.17 (2015): 9965-9982.

Sofieva, Viktoria F., et al. "Merged SAGE II, Ozone_cci and OMPS ozone profile dataset and evaluation of ozone trends in the stratosphere."*Atmospheric Chemistry and Physics* 17.20 (2017): 12533-12552.

Steinbrecht, Wolfgang, et al. "An update on ozone profile trends for the period 2000 to 2016."*Atmospheric chemistry and physics* 17.17 (2017): 10675-10690.

6.19 hbk00064: Coupled ensemble data assimilation for Earth system models

HLRNProject ID:	hbk00064
Run time:	IV/2017 – IV/2018
Project Leader:	Prof. Dr. Thomas Jung[1,2]
ProjectScientists:	Dr. Qi Tang[2], Dr. Lars Nerger[2],
Affiliation:	[1] also at University of Bremen [2] Alfred-Wegener-Institute for Polar and Marine Research, Bremerhaven

Overview

Earth system models simulate different compartments like the ocean, atmosphere, or land surface. Data assimilation for Earth system modeling is challenging due to the complexity of different compartments within the model. In this project, we explore the role of data assimilation into an Earth system model which contains different compartments like the ocean and the atmosphere. Numerical experiments are carried out using the AWI climate model AWI-CM (Sidorenko et al., 2015) and the parallel data assimilation framework PDAF (http://pdaf.awi.de, Nerger et al., 2005, Nerger and Hiller, 2013). Within AWI-CM, the ocean model FESOM and the atmospheric model ECHAM are coupled through the coupler software OASIS3-MCT.

Currently the system allows assimilating global satellite sea surface temperature (SST) and temperature and salinity profiles into the ocean state and thus influences the atmospheric state through the model dynamics, which is the so-called 'weakly coupled DA'. In the ocean, the sea surface height, velocity, temperature and salinity are updated daily using an ensemble Kalman filter (EnKF) for a one-year simulation/assimilation period. The ensemble contains up to 46 model states. For FESOM, the resolution is varying between 160 km in the open ocean and about 30 km in the equatorial region and parts of the Arctic Ocean.For ECHAM a resolution of T63 with 47 layers is used. We analyze whether data assimilation can improve the prediction of ocean states in a coupled ocean-atmosphere model. For the one-year assimilation run, 12,144 processor cores were used with fully parallelized codes for 12 hours on HLRN.

Results

1. Assimilation of SST

The satellite SST observations used in this study are the Copernicus Level-3 product and were collected daily from multiple sensors covering almost the complete globe (80°N – 80°S) with a resolution of 0.1 degrees, see Figure 1. Data gaps exist due to clouds. The initial ensemble was generated from an EOF decomposition of a 1-year model run for the same year 2016. We found that the main challenging point is that the assimilation run over one full year requires stability. The particular reason for this challenge is that in the case of a coupled model the initial model state can be strongly different from the reality represented by the observational data. To this end, the deviation between the initial state estimate and the SST observations is quite large and reaches up to 10 °C for the year 2016. This large deviation

makes a particularly careful application of the data assimilation necessary to avoid too big shocks to the model state.

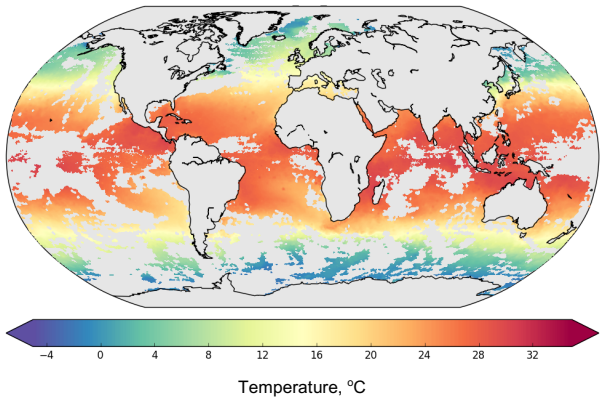

Fig. 1: SST observation on Jan 1st, 2016. Original high-resolution SST data were interpolated onto model grid points.

To handle the large deviations, a first step was to implement a treatment for SST data at the sea-ice edge. The implementation considers the fact that the satellite SST can have data points for ice-free water where the model predicts sea-ice. At these places the difference between the satellite and the modeled SST is not usable as they represent distinct environmental conditions. Accordingly, observations close to model grid points with sea ice are omitted from the assimilation. Further, no assimilation updates are computed for model grid points containing sea ice. Without these adaptations the assimilation resulted in unrealistically low SST under the sea ice close to the sea ice edge.

Results were evaluated by comparing the differences of SST between model predictions and observations at observation grid points. After 30 days, the ocean water temperature error was 2.12 °C for the free run, while it was 1.01 °C for the assimilation run. The global reduction of the error was about 50% after 30 days, see Figure 2.

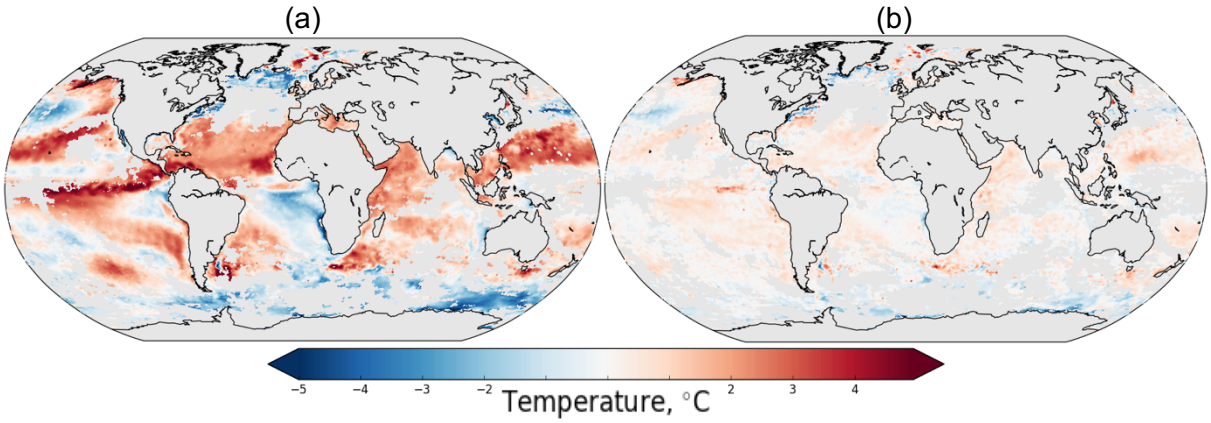

Fig. 2: SST difference between model simulations and observations after 30 days for (a) the free run and (b) the assimilation run.

A further issue is the information transfer of SST into deeper layers of the ocean model, which is performed via the ensemble-estimated cross-covariances. This is particularly relevant around the Equator with fast surface waves and hence a large variability and large variance estimate of the initial model SST, which results in a strong influence of the data assimilation. We found that increasing the estimated observation errors can help here, but

one needs unrealistically high standard deviations of at least 5°C to avoid the unrealistically low temperatures. To solve this problem, we first tried to let the initial ensemble evolve freely over 1 month before starting the assimilation of the observations by February 1, 2016. This 1-month ensemble spinup improves the ensemble quality and hence the stability of the assimilation process. Another test was to start with a high observation error, which is then reduced over time to reach a realistic observation error, which should be at about 0.8°C for the model based on our experience with ocean-only configurations. Another possibility to deal with this problem is vertical localization. Deeper layer grids are updated incrementally according to their depths, which allows limiting the update in deeper layers to avoid instability. This was also tested for our SST assimilation experiment. However, the improvement was small.

2. Assimilation of temperature and salinity profiles

For profile assimilation, the assimilation of either temperature or salinity observations, or the combined assimilation of both were tested for the same year using the same model configuration. The temperature and salinity profiles are from the EN4 data set from the UK MetOffice. They can reach down to 5000m and the average number of profiles is about 1000 per day with quality check, see Figure 3.

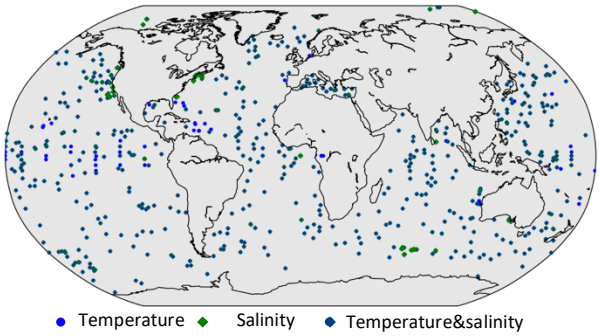

Fig. 3: Locations of temperature and salinity profile on Jan 1st, 2016 for both the surface and the deep ocean layers.

The original observational data were sparse in the horizontal direction, while in vertical direction 400 levels were included. Therefore, a vertical average over 100 meters around each layer depth was calculated and later used as observation data. Data assimilation experiments were done by updating 1) only temperature, 2) only salinity or 3) both temperature and salinity. The observation error was set to 0.8 °C and 0.5 psu for each of the above scenarios. As the number of observations is limited, we analyse the results by plotting the simulation field together with the observation points. Figure 4 shows such fields for the scenario. Large differences of temperature can be observed inthe Equatorial region. However, similar as for SST assimilation, the assimilation of temperature profiles still caused the system instability problem, while the assimilation of salinity was relatively safe, although the improvement was relatively small.

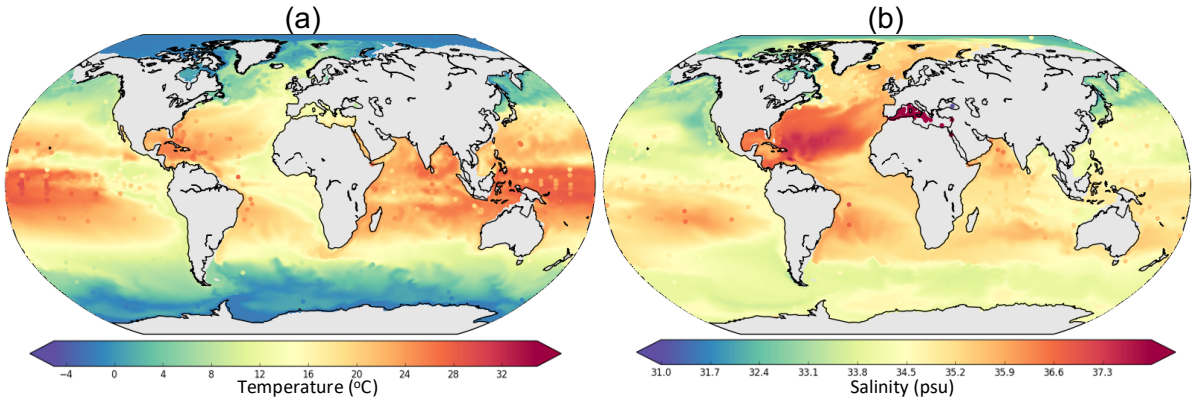

Fig. 4: Model simulated and observed (a) temperature and (b) salinity after 4 days at 100m depth (observations shown as dots).

Outlook

As the assimilation of SST and profile data was only performed into the ocean model state, more experiments need to be done to find an efficient way to reduce the large deviation between the observation and simulation to make the assimilation run stable. Thus, the effect of such weakly-coupled data assimilation on the prediction of atmospheric variables is still unknown and needs to be investigated.

Presentations

Nerger, L., Tang, Q., and Sidorenko, D., Building a Scalable Ensemble Data Assimilation System for Coupled Models with PDAF. University of Reading, Data Assimilation Research Center, Reading, UK, June 13th, 2018. Oral.

Tang, Q., Sidorenko, D., and Nerger, L., Assimilation of satellite and profile observations into a coupled ocean-atmosphere model. AGU fall meeting 2018. December 13th, 2018. Washington D.C., USA. Poster.

Tang, Q., and Nerger, L., Coupled Data Assimilation with AWI-CM and PDAF. ESM project General Assembly 2018. September 12th, 2018. Leipzig, Germany. Oral.

References

Nerger, L., and W. Hiller (2013), Software for ensemble-based data assimilation systems — Implementation strategies and scalability, Computers & Geosciences, 55, 110-118.

Nerger, L., W. Hiller, and J. Schröter (2005), PDAF-the parallel data assimilation framework: experiences with Kalman filtering, in Use Of High Performance Computing In Meteorology, edited, pp. 63-83, World Scientific.

Sidorenko, D., et al. (2015), Towards multi-resolution global climate modeling with ECHAM6–FESOM. Part I: model formulation and mean climate, Climate Dynamics, 44(3), 757-780.

6.20 *hbk00066:* Development of ocean and non-breaking wave coupled Model (FESOM-Wave) and applications to modern and paleo oceans

HLRN Project ID:	hbk00066
Run time:	I/2018 – IV/2018
Project Leader:	Prof. Dr. Gerrit Lohmann
Project Scientists:	Shizhu Wang, Dr. Xun Gong, Dr. Patrick Scholz, Dr. Dirk Barbi and Dr. Dmitry Sidorenko
Affiliation:	Alfred Wegener Institute, Helmholtz Centre for Polar and Marine Research

Overview

Non-breaking surface wave (NBW) is an important process in the upper ocean. The mixing induced by it has been proven necessary to ameliorate the temperature simulations in ocean models (Qiao et al., 2004), especially for the subsurface layer (~50 m). All the ocean models that have employed NBW-induced mixing to improve their simulations, however, are structured-mesh models (e.g., Shu et al., 2011; Song et al., 2012). To adequately resolve the small but key geometrical features in the ocean, mesh resolutions are required to be much higher than that are currently affordable in long-term simulations of structured-mesh models. This promoted the development of unstructured-mesh ocean models in the past decades. The Finite Element Sea ice-Ocean Model (FESOM) is the first mature global unstructured-mesh ocean model that is developed mainly for the purpose of climate research (Danilov et al., 2004; Q. Wang et al., 2008). In this project, as the first attempt to detect the effect of NBW on unstructured-mesh models, we incorporate the NBW-induced mixing coefficients created by MASNUM wave model (the MArine Science and NUmerical Modeling surface wave model) into FESOM. Moreover, the capability of FESOM in conducting high-resolution simulations with less computing resources enables us to analyze the impact of mesh resolution on ocean model results.

Experimental Setup

Based on a coarse FESOM mesh (meshID: CORE2; Figure 1a), we run two experiments with and without NBW (with the experiment setup shown in Table 1), to analyze the effect of NBW on upper-ocean simulation in FESOM. The CORE2 mesh has a nominal resolution of about 1° in most parts of the ocean, a refinement to about 24 km north of 50 °N, and 1/3 ° in the equatorial band, as well as moderate refinement (1/3 ° to 1/2 °) along the coasts. In the vertical, 47 z-levels are used with a resolution of 10 m in the top 100 m and gradually increased downwards. The model is forced from the surface with the data from CORE Ⅱ (Large & Yeager, 2009), which includes surface air temperature, specific humidity, surface wind speed, radiation flux and precipitation. The surface forcing for the river runoff is taken from the interannual monthly dataset provided by Dai et al. (2009).

Table 1: Experiment setups of two FESOM simulations with and without NBW.

Experiment id	**Forcing**	**Non-breaking surface wave**
Ectrl	COREv2	NO
Enbw	COREv2	YES

Table 2: Experiment setups of two FESOM simulations using meshes of different resolutions.

Experiment id	**Forcing**	**Mesh**
Elow	COREv2	CORE2
Ehigh	COREv2	SOO

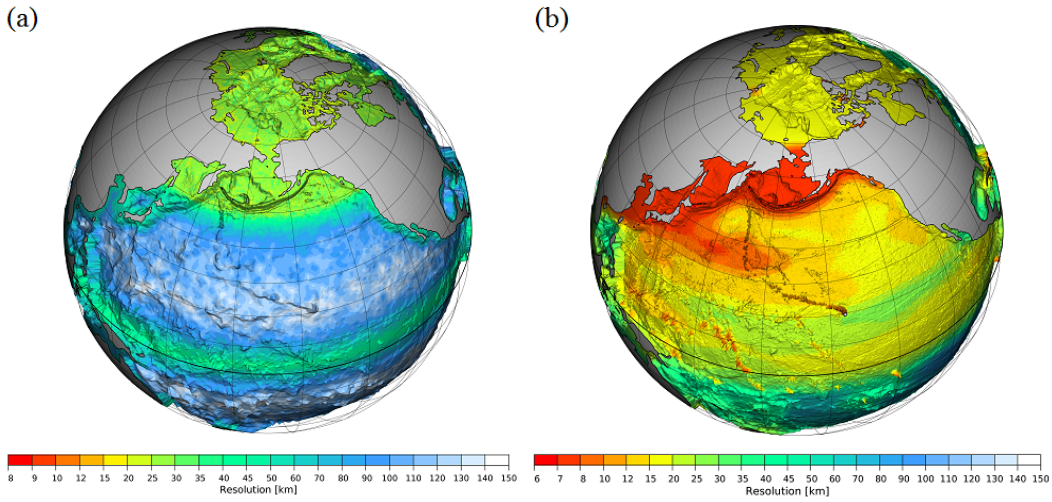

Fig. 1: FESOM (a) CORE2 mesh and (b) SOO mesh.

Results

In this project, we use ocean standalone model and the sea surface temperature (SST) is largely determined by the forcing field. The change of SST due to NBW, accordingly, is rather small. So we analyze the temperature change in the subsurface layer (~50 m). To validate our results, the World Ocean Atlas 2013 version 2 (WOA13 V2; Locarnini et al., 2013) dataset is employed. According to Qiao et al. (2004), the effect of NBW resides mainly on the summer hemisphere and in the Eastern Tropical Pacific (ETP), so four regions in the mid latitudes (the North Pacific, 140 °E - 120 °W, 25 °N - 35 °E; the South Pacific, 180 °W - 70 °W, 25 °S - 35 °S; the North Atlantic, 50 °W - 10 °W, 30 °N - 40 °N; the ETP, 110 °W - 70 °W, 5 °S - 5 °N) are chosen to compare the role of NBW in changing subsurface temperatures. In mid latitudes, simulated subsurface temperatures in Ectrl show a persistent cold bias compared to observations (Figure 2a, 2b and 2c, solid red line). NBW exerts a strong warming in the subsurface, resulting in more reasonable and accurate temperature representations (in Figure 2a, 2b and 2c, the dashed lines comply well with the red dots).

The warming effect of NBW is stronger in local summer, with the amplitude exceeding 1.0 ℃. In the ETP, the obvious cold bias in the subsurface exists all year round. In most of the months, the incorporation of NBW-induced mixing ameliorates models results, with the warming effect peaking in April. But the NBW mixing creates a too strong warming in May, June and July, deteriorating the model results.

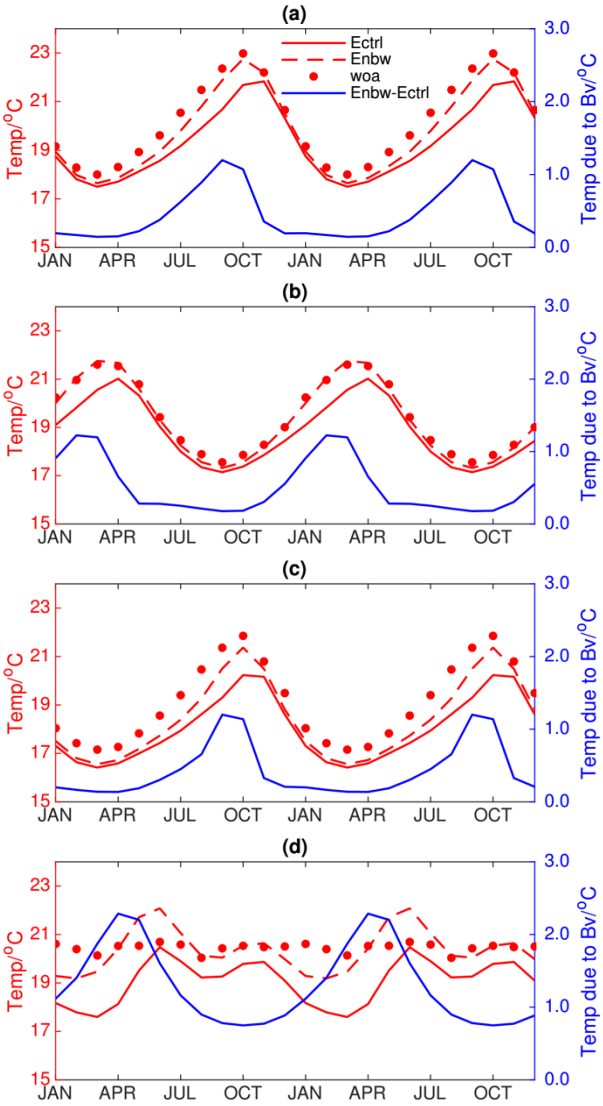

Fig. 2: Subsurface temperature and NBW-induced temperature change in (a) NP, (b) SP, (c) NA and (d) ETP.

We interpolate the results of Elow and Ehigh from FESOM mesh to the same 0.1°×0.1° longitude-latitude format, to eliminate the potential impact of postprocessing on the results. Simulated SSTs in Northwest Pacific in February and August are shown in Figure 3. A prominent advantage of high-resolution mesh can be easily seen: the small geometrical details in the ocean, e.g., the narrow Tartar Strait and the small islands, which are total absent in the CORE2 mesh, can be well represented by the SOO mesh. With respect to the SSTs, both meshes can simulate reasonable large-scale SST patterns in summer and winter. But for the curved structure of the Kuroshio extension, the CORE2 mesh cannot well simulate it because the coarse mesh smooths the flow details within the grid scale, thus depicting a too wide flow axis. The SOO mesh, on the other hand, captures a reasonable

Kuroshio extension, with a compacted and strong flow axis. The horizontal advection in the eddy-resolving SOO mesh, can be strengthened due to the dynamics of the resolved mesoscale eddies. For example, the almost absent inflow from the Kuroshio extension to the Yellow Sea in Elow (Figure 3a) is well simulated in Ehigh (Figure 3c).

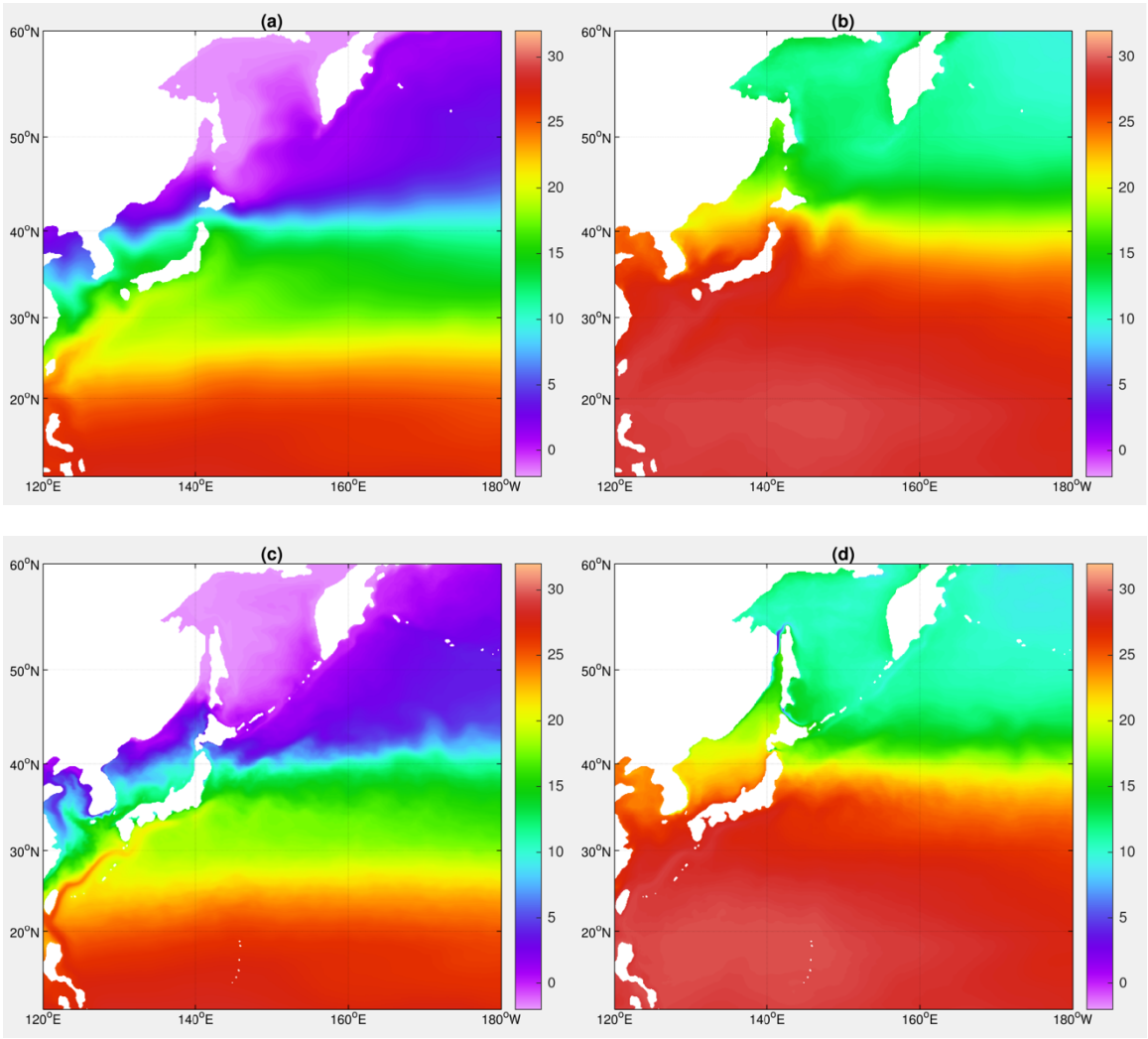

Fig. 3: Simulated SSTs in Western Pacific using meshes of different resolutions. (a) February, CORE2 mesh; (b) August, CORE2 mesh; (c) February, SOO mesh; (d) August, SOO mesh.

Discussions

Our results have shown that like the role that NBW has played in improving upper-ocean simulations in structured-mesh ocean models, this process exerts a similar impact on unstructured-mesh models (in our case, the FESOM model). Almost all of the cold biases in subsurface in the mid latitudes can be eliminated due to NBW-induced mixing. In the Eastern Tropical Pacific, however, caveat need to be taken. While it improves the simulation from August to April, NBW deteriorates the model results in May, June and July. Actually, in this 'doldrum' region, the temperature change due to NBW is a combined effect of NBW-induced mixing coefficients and the vertical temperature gradients (S. Wang et al., 2019). So we guess the too-strong warming effect in May, June and July results from the exaggerated vertical temperature gradients.

The distorted presentation of the western boundary current (WBC) is a common failing of the coarse-resolution ocean models. It has been shown that using eddy-resolving resolution can significantly improve the simulation of the ocean dynamics and the air-sea interaction processes in the WBC regions, thus reducing the temperature biases (e.g., Kwon et al., 2010; Sein et al., 2016). Our FESOM mesh with regional refinement in Northwest Pacific also shows its capability to capture the curved structure of the Kuroshio extension. The coarse-resolution smooths the spatial variability and thus simulates a wider but weaker Kuroshio extension.

Eddies help create re-stratification in the water column (Chanut et al., 2008), thus counteracting the de-stratification of the vertical mixing due for example to the non-breaking surface wave. Therefore, the performance of temperature simulation in the upper ocean is indeed associated with the overall effect of the two counteracting processes. The mixing induced by NBW will be incorporated into FESOM using the high-resolution mesh, to diagnose the respective role of Eddies and NBW in changing upper ocean simulations.

Reference

1. Chanut, J., Barnier, B., Large, W., Debreu, L., Penduff, T., Molines, J. M., & Mathiot, P. (2008), Mesoscale eddies in the Labrador Sea and their contribution to convection and restratification. Journal of Physical Oceanography, 38(8), 1617-1643.
2. Dai, A., Qian, T., Trenberth, K. E., & Milliman, J. D. (2009), Changes in continental freshwater discharge from 1948 to 2004. Journal of Climate, 22(10), 2773-2792.
3. Danilov, S., Kivman, G., & Schröter, J. (2004), A finite-element ocean model: principles and evaluation. Ocean Modelling, 6(2), 125-150.
4. Kwon, Y.-O., Alexander, M. A., Bond, N. A., Frankignoul, C., Nakamura, H., Qiu, B., & Thompson, L. A. (2010), Role of the Gulf Stream and Kuroshio–Oyashio Systems in Large-Scale Atmosphere–Ocean Interaction: A Review. Journal of Climate, 23(12), 3249-3281. doi:10.1175/2010jcli3343.1
5. Large, W. G., & Yeager, S. (2009), The global climatology of an interannually varying air–sea flux data set. Climate Dynamics, 33(2-3), 341-364.
6. Locarnini, R., Mishonov, A., Antonov, J., Boyer, T., Garcia, H., Baranova, O., et al. (2013), World Ocean Atlas 2013, Volume 1: Temperature, edited by: Levitus, S. A. Mishonov Technical Ed., NOAA Atlas NESDIS, 73, 40.
7. Qiao, F., Yuan, Y., Yang, Y., Zheng, Q., Xia, C., & Ma, J. (2004), Wave-induced mixing in the upper ocean: Distribution and application to a global ocean circulation model. Geophysical Research Letters, 31(11).
8. Sein, D. V., Danilov, S., Biastoch, A., Durgadoo, J. V., Sidorenko, D., Harig, S., & Wang, Q. (2016), Designing variable ocean model resolution based on the observed ocean variability. Journal of Advances in Modeling Earth Systems, 8(2), 904-916.
9. Wang, Q., Danilov, S., & Schröter, J. (2008), Finite element ocean circulation model based on triangular prismatic elements, with application in studying the effect of topography representation. Journal of Geophysical Research Atmospheres, 113(C5), 24-35.
10. Wang, S., Wang, Q., Shu, Q., Scholz, P., Lohmann, G., & Qiao, F. (2019), Improving the Upper-ocean Temperature in an Ocean Climate Model (FESOM 1.4): Shortwave Penetration vs. Mixing Induced by Non-breaking Surface Waves. Journal of Advances in Modeling Earth Systems.

6.21 hbk00067: Seespiegelschwankungen des Kaspischen Meeres im Spätquartär und ihr Einfluss auf die Klimadynamik

HLRN-Projektkennung:	hbk00067
Laufzeit:	I/2018 – I/2019
Projektleiter:	Prof. Michael Schulz
Projektbearbeiter.	Dr. Matthias Prange, Sri Nandini
Institut / Einrichtung:	MARUM – Zentrum für Marine Umweltwissenschaften, Universität Bremen

Überblick

Im Rahmen des EU-finanzierten Marie Sklodowska-Curie Innovative Training Network (ITN) *PRIDE* (Drivers of Pontocaspian Biodiversity Rise and Demise) werden vergangene Umweltveränderungen in der pontokaspischen Region (Einzugsgebiete des Schwarzen Meeres mit dem Asowschen Meer, des Kaspischen Meeres und des Aralsees sowie Bereiche des angrenzenden West- und Zentralasien) und deren Einfluss auf die regionale Biodiversität untersucht (http://www.pontocaspian.eu). Ein Schwerpunkt liegt dabei auf der Untersuchung vergangener Klimate und Seespiegelschwankungen des Kaspischen Meeres während der jüngeren Erdgeschichte, dem Spätquartär. Klimasimulationen sollen helfen, die physikalischen Prozesse, die zu Seespiegelschwankungen in der Vergangenheit führten und in der Zukunft führen werden, besser zu verstehen. Als Teil des *PRIDE*-Projektes führen wir Klimasimulationen für eine Reihe von Zeitscheiben durch, für welche große Seespiegeländerungen in geologischen Studien rekonstruiert wurden.

Heute ist das Kaspische Meer das größte endorheische Gewässer der Erde mit einem Wasservolumen von 78.000 km^3 und einer Oberfläche von rund 380.000 km^2 bei einem Seespiegel von ca. −27 m gegenüber dem globalen Meeresspiegel. Im Laufe des Spätquartärs schwankte der Seespiegel jedoch mit einer Amplitude von 120-150 m. Der letzte extreme Niedrigstand mit einem Seespiegel von rund −50 bis −70 m war verbunden mit der sog. Mangyshlak-Regression und lässt sich für das frühe Holozän (ca. 11.500 Jahre bis 8.500 Jahre vor heute) rekonstruieren. Auf die Mangyshlak-Regression folgte die Novokaspische Transgression mit beträchtlichem Seespiegelanstieg.

Ein extremer Hochstand mit einem Wasserspiegel von bis zu +50 m resultierte aus der “Early Khvalynian Transgression”, deren Datierung allerdings stark umstritten ist. So existieren Datierungen für diese Transgression sowohl für das Letzte Glaziale Maximum (ca. 19.000-23.000 Jahre vor heute) als auch für die nachfolgende Deglaziation und das vorhergehende Marine Isotopenstadium 3 (ca. 30.000-35.000 Jahre vor heute). Andere Rekonstruktionen deuten auf regressive Bedingungen (sog. „Elton Regression“) im Letzten Glazialen Maximum hin.

Von besonderer Bedeutung mit Blick auf ein besseres Verständnis zukünftiger hydroklimatischer Veränderungen im kaspischen Einzugsgebiet sind Rekonstruktionen vergangener warmer Klimate wie das Letzte Interglazial (Marines Isotopenstadium 5e). Lange Zeit wurde dem Letzten Interglazial (ca. 120.000-130.000 Jahre vor heute) die „Late Khazarian Transgression“ zugeordnet. Aufgrund erheblicher Datierungsunsicherheiten wurde

dies in jüngeren Arbeiten jedoch in Frage gestellt und dem Letzten Interglazial eine mögliche Regression zugeordnet.

Als ursächlich für die enormen Seespiegelschwankungen gelten neben geologischen Prozessen (z.B. Sedimentation, tektonische und seismische Aktivität, Küsten-geomorphologie) hauptsächlich hydroklimatische Veränderungen während des Spätquartärs und deren Einfluss auf die Wasserbilanz im Einzugsgebiet des Kaspischen Meeres, obgleich die Beziehung zwischen paläoklimatischen Schwankungen und dem kaspischen Wasserspiegel noch kaum verstanden ist. Unsere Klimasimulationen für das frühe Holozän, das Letzte Glaziale Maximum und die anschließende Deglaziation (Heinrich-Stadial 1, 15.000-18.000 Jahre vor heute), das Marine Isotopenstadium 3 sowie das Letzte Interglazial sollen helfen, die rekonstruierten Seespiegelschwankungen mit paläoklimatischen Bedingungen in Beziehung zu setzen und die damit verbundenen hydroklimatischen Prozesse besser zu verstehen. Zur Simulation der paläoklimatischen Zeitscheiben verwenden wir das Community Earth System Model (CESM Version 1.2.2). Das Klimamodell wird mit entsprechenden Randbedingungen angetrieben. Diese umfassen Erdorbitalparameter, Treibhausgaskonzentrationen, Eisschildkonfigurationen und daraus resultierende globale Meeresspiegeländerungen.

Ergebnisse

Transgressive (d.h. Seespiegelanstieg) oder regressive (d.h. Seespiegelabsenkung) Bedingungen können in erster Näherung aus der atmosphärischen Wasserbilanz (Gesamtniederschlag minus Evapotranspiration) im Einzugsgebiet des Kaspischen Meeres abgeleitet werden. Unsere Paläozeitscheibenexperimente zeigen transgressive Bedingungen (d.h. positive Wasserbilanz) sowohl für das Marine Isotopenstadium 3 (35.000 Jahre vor heute) als auch für die Spätphase des Heinrich-Stadials 1 während der Deglaziation (15.000 Jahre vor heute). Ebenso werden transgressive Bedingungen für das Letzte Interglazial (127.000 Jahre vor heute) simuliert, was entsprechende Rekonstruktionen der „LateKhazarian Transgression“ untermauert. Auch für das frühe Holozän (9.000 Jahre vor heute) werden transgressive Bedingungen im Klimamodell simuliert, was darauf schließen lässt, dass die Novokaspische Transgression vermutlich bereits zu diesem Zeitpunkt einsetzte. Regressive Bedingungen wurden für das Letzte Glaziale Maximum simuliert und untermauern entsprechende Datierungen zur „Elton Regression“.

Abbildung 1 zeigt exemplarisch die klimatischen Bedingungen für das Letzte Interglazial. Erhöhte Niederschläge über dem Großteil des kaspischen Einzugsgebietes (außer im nördlichen Wolga-Becken) sind ausschlaggebend für eine positive Wasserbilanz und somit transgressive Bedingungen. Dieses Niederschlagsbild ist Teil eines großräumigen Musters mit erhöhten Niederschlägen im Mittelmeerraum, Zentralasien und den asiatischen Monsungebieten, während Zentral- und Nordeuropa trockener ist als heute. Gleichzeitig zeigt das Letzte Interglazial ein relativ warmes Klima über Europa und dem kaspischen Einzugsgebiet. Trotz der im Vergleich zum vorindustriellen Kontrollklima erhöhten Temperaturen eignet sich das Letzte Interglazial nicht als Analogie zur globalen Erwärmung des 21. Jahrhunderts in Bezug auf die Wasserbilanz des Kaspischen Meeres. Im Gegensatz zur positiven Bilanz und einer damit einhergehenden Transgression im Letzten Interglazial zeigen die mit dem Modell gerechneten Projektionen für das 21. Jahrhundert eine negative Wasserbilanz (Abb. 2) und eine einhergehende Absenkung des kaspischen Seespiegels aufgrund erhöhter Verdunstung im wärmer werdenden Klima. Im extremen Fall des RCP8.5-Szenarios beträgt die Zunahme der Verdunstungsrate über dem Kaspischen Meer 15-20% im Laufe des 21. Jahrhunderts. Hieraus lässt sich eine Abnahme des Seespiegels von bis zu 18 m am Ende des 21. Jahrhunderts abschätzen (Nandini et al., eingereicht). Ein solch

drastisches Absinken des Seespiegels würde nicht nur zu einem verheerenden Verlust wichtiger Habitate im Kaspischen Meer führen, sondern auch die Küsteninfrastruktur massiv beeinträchtigen mit erheblichen Konsequenzen für die Ökonomie der Anrainerstaaten.

Die starken Seespiegelschwankungen im Kaspischen Meer sind verbunden mit beträchtlichen Änderungen der Ausdehnung der Seeoberfläche. Welchen Einfluss diese Änderungen ihrerseits auf das regionale und überregionale Klima haben, war bislang kaum untersucht. In zusätzlichen Modellexperimenten, in denen wir die Ausdehnung des Kaspischen Meeres systematisch verändert haben, konnten wir Rückkoppelungsmechanismen zwischen Seespielschwankungen und atmosphärischer Dynamik untersuchen. Dabei hat sich gezeigt, dass die Ausdehnung des Kaspischen Meeres nicht nur für die eigene Wasserbilanz von großer Bedeutung ist, sondern auch Winde und Niederschläge in weit entfernten Regionen wie dem Nordpazifik signifikant beeinflusst.

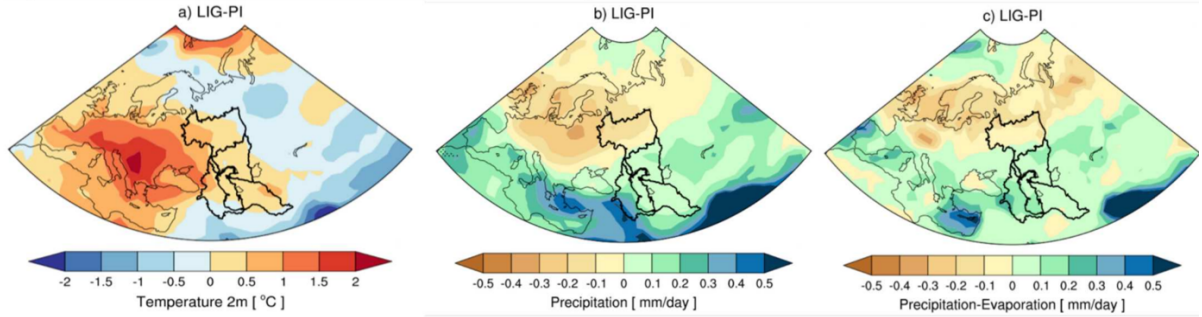

Abb. 1: Klimaänderungen des Letzten Interglazials (127.000 Jahre vor heute) relativ zum vorindustriellen Klima simuliert mit CESM1.2.2. Gezeigt sind Jahresmittel für (a) 2-m-Temperatur, (b) Niederschlag und (c) Niederschlag minus Verdunstungsrate. Dicke Konturen zeigen das Kaspische Meer und sein Einzugsgebiet (unterteilt in die Einzugsgebiete verschiedener Flüsse).

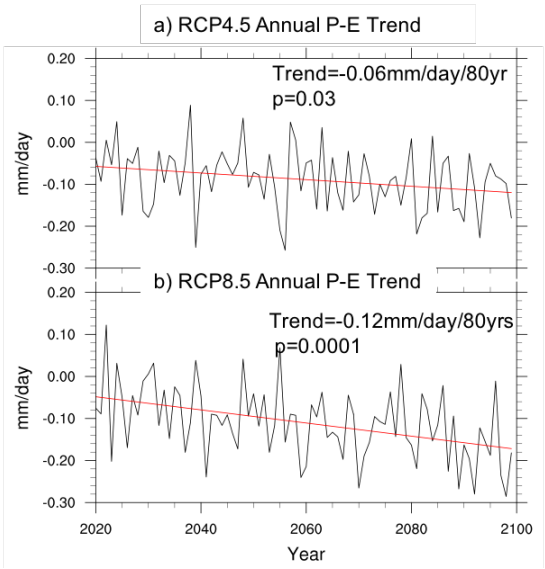

Abb. 2: Zeitreihen der jährlichen Wasserbilanz des Kaspischen Meeres (d.h. Niederschlag minus Verdunstungsrate gemittelt über das gesamte Einzugsgebiet) bis zum Jahr 2100 im (a) RCP4.5-Szenario (mittleres Emissionsszenario) und (b) RCP8.5-Szenario (Hochemissionsszenario) simuliert mit CESM1.2.2. Beide Szenarien ergeben negative Trends in der Wasserbilanz, die zu einem Absinken des Seespiegels um mehrere Meter führen.

Publikationen/Manuskripte

1 Nandini, S. D., M. Prange, K. Arpe, U. Merkel, M. Schulz, *Past and future impact of North Atlantic winter teleconnections with the Caspian Sea catchment area*, eingereichtbei*International Journal of Climatology*.
2 Nandini, S. D., S. A. Koriche, M. Prange, J. Singarayer, K. Arpe, H. Cloke, M. Schulz, P. Bakker, S. A. G. Leroy, *Impacts of the Caspian Sea surface area on atmospheric water budget and circulation patterns*, in Vorbereitung.
3 Nandini, S. D., M. Prange, P. Bakker, K. Arpe, M. Schulz, S. A. G. Leroy, *Late Quaternary hydroclimate variations in the Caspian Sea catchment area: A model study*, in Vorbereitung.

6.22 hbk00069: Zooplankton and ocean biogeochemistry - Role of zooplankton dynamics for ocean biogeochemistry

HLRN-Projektkennung:	hbk00069
Laufzeit:	II/2018 – IV/2018
Projektleiter:	Prof. Dieter Wolf Gladrow[1,2]
Projektbearbeiter.	J. Hauck, O. Karakus, V. Schourup-Kristensen, O. Gurses
Institut / Einrichtung:	Alfred Wegener Institute, Helmholtz Centre for Polar and Marine Research University of Bremen

In Short

1. Discrepancy between models and observations of the ocean carbon sink, possibly related to ecosystem processes
2. Second zooplankton (Antarctic krill) class implemented into ecosystem model REcoM2 improves ecosystem structure
3. Sensitivity of the ocean carbon sink will have to be tested in longer simulation

Introduction Carbon dioxide (CO_2) emissions from fossil fuels and land-use change amounted to 11.2 PgC yr^{-1} in 2016 and force anthropogenic climate change. Ocean and land sinks provide an extremely valuable service to humankind by each drawing down about 25 % of anthropogenic CO_2 emissions, thereby slowing the rate of anthropogenic climate change. On time-scales longer than a century the ocean will be the main repository for anthropogenic CO_2 emissions and the Southern Ocean is the main conduit by which this CO_2 enters the ocean.

Organic matter formed through photosynthesis by phytoplankton in the surface mixed layer is transported to depth by sinking of particles formed through aggregation and grazing processes, by vertical migration of zooplankton and by advection of dissolved organic matter. Sinking particles consist mostly of faecal pellets and macroscopic aggregates and are remineralized by bacterial degradation. The sinking rates and thus depth of remineralization determine the time-scale for which carbon is removed from the surface ocean where gas-exchange with the atmosphere occurs.

However, zooplankton not only control the amount of sinking particles by their faecal pellet production, but also exert a strong control on the maximum possible biomass of phytoplankton, and release dissolved carbon during sloppy feeding, excretion and respiration. Furthermore, zooplankton grazing on particles ("gate-keeping") also leads to the destruction of phytodetrital aggregates and faecal pellets.

In the Marine Ecosystem Model Intercomparison Project (MAREMIP) we revealed large discrepancies among models on global and regional future changes in primary and export production [1]. Climate-induced changes in particle formation and destruction have equally large effects on the projected amount of carbon exported to the deep ocean as changes in primary production [1]. Yet, the models disagree on

1. the relative importance of various particle formation (aggregation versus zooplankton grazing) and destruction processes,
2. the relative importance of phytoplankton groups (nanophytoplankton, diatoms) for particle formation, and even on
3. the direction of export change [1].

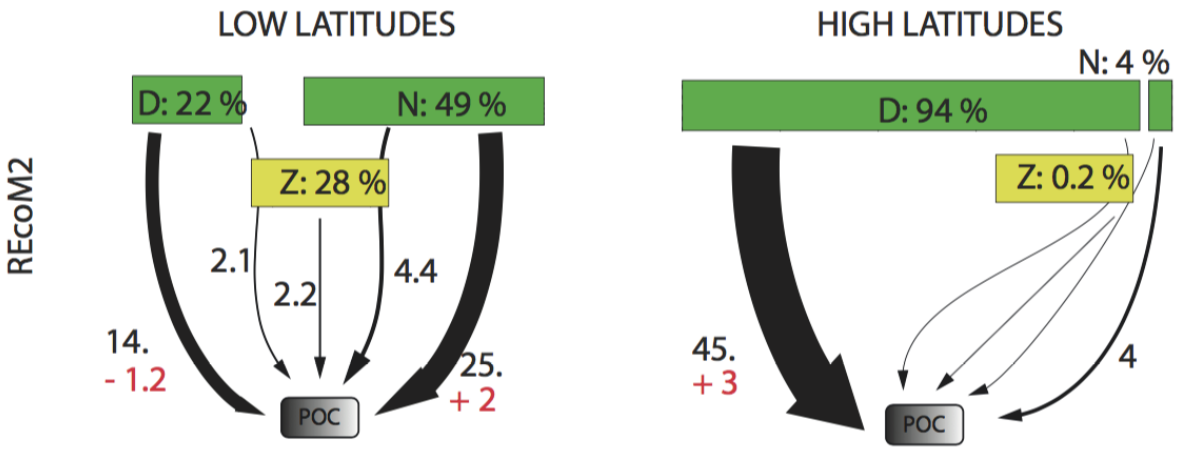

Figure 1: Diagrammatic depiction of the ecosystem structure and the particle formation mechanisms in the low latitudes (< ±30° N/S, on the left) and in the high latitudes (>60° S, on the right) for in the ecosystem model REcoM2. Shown are the 2012-2031 average (black numbers) and the changes between the 2012-2031 period and the 2081-2100 period (red numbers). The green boxes show diatom (marked with D) and nano-phytoplankton (N) biomass, the yellow boxes (Z) zooplankton biomass, all given in percent of total biomass. The arrows within the panels denote from left to right: diatom aggregation, grazing on diatoms, zooplankton mortality, grazing on nanophytoplankton and nano-phytoplankton aggregation. The fluxes are given in percent of total net primary production (NPP). Figure taken from [1].

This comes as no surprise, as physiological responses of phytoplankton to climate change and processes of particle formation/destruction are either not represented or oversimplified in models, despite their importance for atmospheric CO_2 concentration.

One discrepancy in REcoM2 is that with the chosen parameter values, zooplankton grazing in the tropics (nanophytoplankton is the main primary producer) is reasonably well represented, but there is too little grazing on diatoms (the main primary producers in high latitudes, Fig 1).

Results

Within this project, we have implemented a second zooplankton class into the ecosystem model REcoM2 [2, 3] coupled to the ocean circulation model FESOM (previously only in MITgcm-REcoM, see Fig 2). The second zooplankton was chosen to be parameterized as Antarctic krill (macrozooplankton) that has a preference to graze on diatoms. The choice for Antarctic krill was made to specifically enhance zooplankton grazing in the Southern Ocean where largest model discrepancies exist. The parameterization included definition and testing of a temperature function for krill and a rather sophisticated description of krill respiration which takes into account a higher respiration during feeding and a reduced respiration during winter. These parameterizations were tested and adjusted based on initial results.

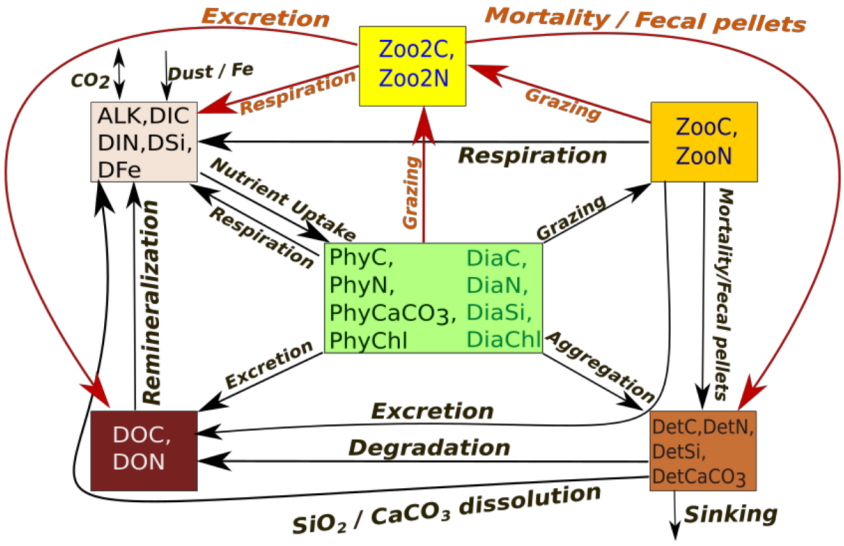

Figure 2: Flow chart of the ecosystem model REcoM2 [2, 3], now with a second zooplankton class.}

As expected, such a structure and parameterization lead to stronger zooplankton grazing also in high latitudes. The parameters were varied around values found in the literature, so that the second zooplankton class could build up biomass in the model. It now particularly appears south of the area where the first zooplankton group dominates (Figure 3). The northern limit of the occurrence is defined by the temperature function.

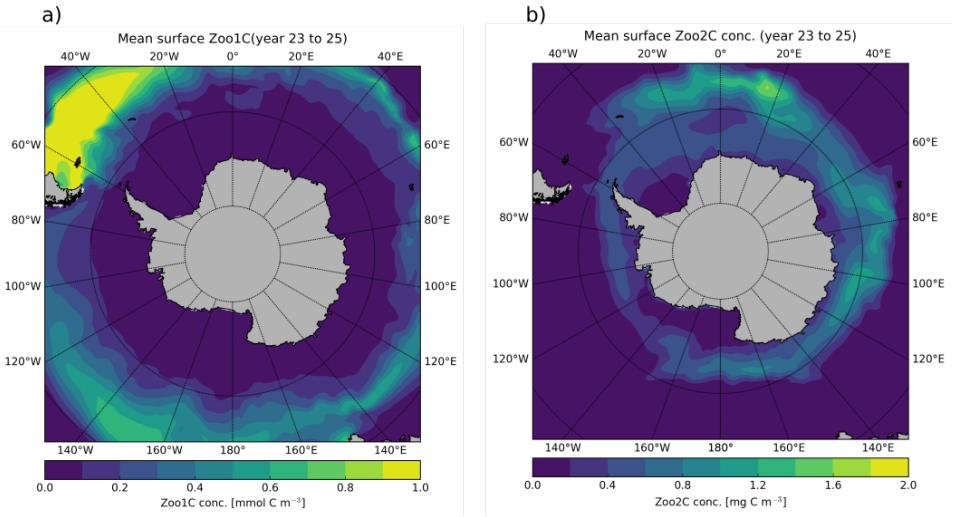

Figure 3: Zooplankton biomass, (a) first zooplankton group (mesozooplankton), (b) second zooplankton group: Antarctic krill

Further comparison with observations of krill density suggest that the area of krill distribution is roughly reproduced. However, the spatial variability and peak numbers could not be reproduced in the model yet (Figure 4). This can be partly explained by processes that are not taken into account (active movement, diel vertical migration of zooplankton), and by generally underestimated variability in large-scale models as compared to patchy observations. However, we are currently also re-confirming the nutrient and chlorophyll distribution and testing the sensitivity of the second zooplankton class to various biogeochemical parameters (e.g. iron input) that could have an influence on the krill distribution.

The implementation of krill led to a reorganization of the ecosystem, which leads to a larger share of total biomass now being in the zooplankton compartments (Figure 5). The implementation of krill also led to an increase in the biomass of the first zooplankton group, notably by 42 %.

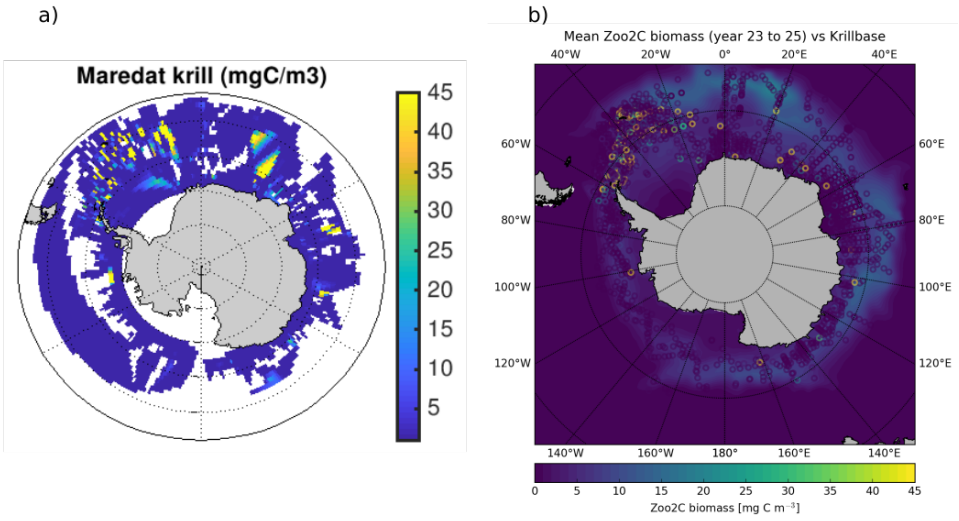

Figure 4: Krill biomass (mgC m^{-3}), (a) from observations (krillbase), (b) in the model

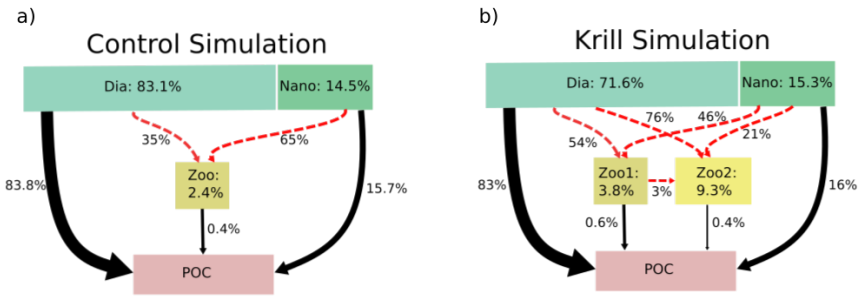

Figure 5: Diagrammatic representation of the ecosystem structure and the particle formation mechanisms in the Southern Ocean a) control simulation, b) krill simulation. The green boxes show diatom (Dia) and nanophytoplankton (Nano). Yellow boxes show the first zooplankton group (Zoo1) and the second zooplankton group (Zoo2). The numbers in the boxes are the percentage of the related compartment to all living compartments in the Southern Ocean. The pink box shows particulate organic carbon (POC). The black arrows show the contribution of each living compartment to the POC production (percentage of total POC production). The red arrows show the grazing of the zooplankton groups on diatom and nanophytoplankton groups (percentage of total grazing on all groups).

The implementation of krill has an influence on the ocean biogeochemistry (not shown). In particular it leads to a higher rate of recycling in the upper ocean, and hence it reduces the model's negative bias in nutrient concentrations by 2.6 % for dissolved inorganic nitrogen and by 10.6 % for dissolved silicic acid and dissolved iron. The response of primary production to the implementation of the second zooplankton group differed regionally with an increase in the Atlantic and a decrease in the Pacific sector of the Southern Ocean. Diatom productivity was generally reduced due to the additional grazing by krill and nanophytoplankton productivity increased on a low background level. The seasonal cycle of chlorophyll showed no significant change. Export production in the Southern Ocean decreased from ca. 2.8 PgC/yr by 0.1 to 2.7 PgC/yr.

Outlook

The main goal of simulating a more realistic ecosystem has been reached, while the regional distribution of krill will be further evaluated and tuned. These were the first experiments with FESOM-REcoM by the PI and her group, and the experiments have pointed us to the necessity of some additional sensitivity tests. Longer runs will be necessary to evaluate the impact of the implementation of krill on sea-air CO_2flux, that were not funded here.

Publications

O. Karakus: Estimating the effect of krill on the Southern Ocean ecosystem functioning *Master thesis, Institute of Marine Sciences of Middle East Technical University, Turkey and Alfred-Wegener-Institut, Helmholtz-Zentrum für Polar- und Meeresforschung*, (October 2018). Journal submission in preparation

WWW

https://www.awi.de/en/science/biosciences/marine-biogeoscience/main-research-focus/mathematical-modelling.html

More Information

[1] C. Laufkötter, M. Vogt, N. Gruber, O. Aumont, L. Bopp, S. C. Doney, J. P. Dunne, J. Hauck, J. G. John, I. D. Lima, R. Seferian, and C. Völker: Projected decreases in future marine export production: the role of the carbon flux through the upper ocean ecosystem, *Biogeosciences*. **13(13)**, 4023-4047 (2016). doi:0.5194/bg-13- 4023-2016

[2] J. Hauck, J., C. Völker, T. Wang, M. Hoppema, M. Losch, and D. A. Wolf-Gladrow: Seasonally different carbon flux changes in the Southern Ocean in response to the southern annular mode, *Global Biogeochemical Cycles*. **27(4)**, 12361245 (2013). doi: 0.1002/2013GB004600

[3] V. Schourup-Kristensen, D. Sidorenko, D. A. Wolf-Gladrow, and C. Völker: A skill assessment of the biogeochemical model REcoM2 coupled to the Finite Element Sea Ice Ocean Model (FESOM 1.3), *Geoscientific Model Development*. **7(6)**, 27692802 (2014). doi: 10.5194/gmd-7-2769-2014

Funding

Helmholtz Young Investigator Group Marine Carbon and Ecosystem feedbacks in Earth System (MarESyS)

6.23 hbp0029: Carrier dynamics and optical properties of transition metal dichalcogenides

HLRN-Projektkennung:	hbp0029
Laufzeit:	IV/2015 – IV/2019
Projektleiter:	Dr. rer. nat. Michael Lorke, Prof. Dr. Frank Jahnke
Projektbearbeiter:	Dr. rer. nat. Alexander Steinhoff, Dr. rer. nat. Matthias Florian, M. Sc. Daniel Erben
Institut / Einrichtung:	Institut für Theoretische Physik, Universität Bremen

Introduction

Monolayers of transition metal dichalcogenides (TMDCs) are today one of the busiest research areas of semiconductor physics. From a fundamental viewpoint, among the most intriguing features of TMDCs are the large binding energies and exceptional spectral fine structures of many-particle complexes. Fascinating prospects arise from the possibility to manipulate Coulomb interaction in atomically thin materials via their dielectric environment. Thereby, the optical properties of TMDCs dominated by strong excitonic effects may be tailored by integrating these materials into appropriate heterostructures. The aim of this project is to investigate carrier dynamics and optical properties of TMDCs in heterostructures using state-of-the-art many-body methods to gauge the potential of devices for light emission and shed light on fundamental Coulomb interaction effects.

Results

Biexciton fine structure in monolayer TMDC semiconductors

Due to strong Coulomb interaction, the optical properties of atomically thin TMDC semiconductors are shaped by the emergence of correlated many-body complexes such as bound electron-hole pairs called excitons. Biexcitons, which are four-particle complexes, in these materials are less understood and it has been established only recently that they are spectrally located between exciton and trion.

In publication [1], we have shown that biexcitons in monolayer TMDCs exhibit a distinct and rich fine structure on the order of meV due to efficient electron-hole exchange interaction. Ultrafast pump-probe experiments on monolayer WSe_2 performed by our experimental partners in Texas and Berlin (Li group and Woggon group) reveal decisive biexciton signatures and a fine structure in excellent agreement with our microscopic theory, see Fig. 1. We predict the emergence of three bright biexciton states with binding energies of about 3, 12 and 20 meV. To this end, we have solved a generalized four-particle Schrödinger equation based on material-realistic band structures and screened Coulomb matrix elements obtained from first-principle calculations.

Exchange interaction between electrons caused by their indistinguishability is at the heart of quantum mechanics and chemical bonding. Electrons and holes in a semiconductor on the other hand are approximately distinguishable, which generally results in weak electron-hole exchange effects. For example, in semiconductor quantum dots, the exciton fine structure due to electron-hole exchange is on the order of micro-eV, while in quantum wells no such effects have been observed. Our results show that atomically thin TMDC semiconductors are

well-suited to study the fine structure of correlated Coulomb complexes experimentally as these materials combine large binding energies and relatively strong electron-hole exchange interaction. Biexcitons reveal a distinct fine structure that can be traced back to electron-hole exchange, along with local-field corrections to biexciton binding energies.

We further demonstrate that profound insight into the relevant interaction processes can be gained by condensing the full microscopic theory into a simple configuration model for biexcitons. From the observation that the simple model captures the structure of the full spectrum we conclude that the latter is essentially determined by the spin-selection rules of electron-hole exchange, while precise numbers can be obtained from microscopic calculations.

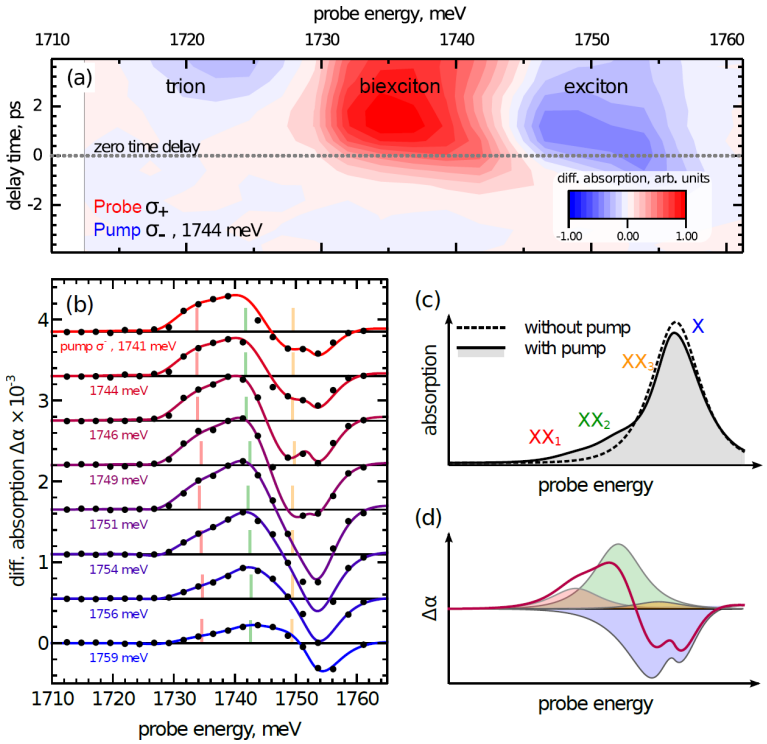

Fig. 1: Differential absorption of monolayer WSe_2 on sapphire from theory and experiment. **(a)** Time-resolved differential absorption data from cross-polarized pump-probe spectroscopy with a pump energy of 1744 meV. **(b)** The corresponding differential absorption spectra at zero time delay (filled black circles) for pump-pulse energies ranging from 1759 meV (bottom) to 1741 meV (top) are compared to fits based on the predictions of our theoretical model (solid lines). The vertical bars denote the spectral positions of the three optically bright biexciton states. **(c)** Fit function for absorption spectra without and with pump at 1746 meV. The pump-induced emergence of asymmetry of the exciton line (X) as well as two prominent biexciton resonances (XX_1, XX_2) are visible. The third biexciton (XX_3) has a much smaller oscillator strength. **(d)** Differential absorption from the fitting curves in (c). Asymmetric lineshape, bleaching and shift of the exciton lead to the remarkable signature in the differential absorption that is also observed in experiment. The shaded areas show the contributions of biexcitons and exciton to the differential signal.

Optical gain in monolayer TMDC semiconductors

Nanolasers receive much attention due to their promise of energy-efficient light generation and integrability in optoelectronic devices. Resonators, such as microdisc or photonic-crystal cavities, confine light to a volume of its cubic wavelength. Within this mode volume the light-matter interaction is strongly increased, such that the emission into the laser mode is favored over loss channels, giving rise to the high efficiency that is sought after in nanolasers.

Gain materials from atomically thin semiconductors have moved into the focus of investigations for their potential in laser applications. In contrast to gain media that are commonly used in nanolasers, such as semiconductor quantum wells and quantum dots, the band structure and the electronic states of TMDC monolayers are highly susceptible to modifications of the dielectric environment. Moreover, these materials can be positioned deterministically into the evanescent field of photonic-crystal or microdisc cavities. Combined

advancements in the understanding of material properties and fabrication techniques hold enticing possibilities for integrated photonics applications and light sources.

In publication [2], we provide results from microscopic optical gain calculations of highly excited TMDC monolayers and specify requirements to achieve lasing with four commonly used TMDC semiconductors. Our approach includes band-structure renormalizations due to excited carriers that trigger a direct-to-indirect band-gap transition. As a consequence, we predict a rollover for the gain that limits the excitation regime where laser operation is possible. A parametrization of the peak gain is provided that is used in combination with a rate-equation theory to discuss consequences for experimentally accessible laser characteristics. Fig. 2 shows numerical results for the optical gain in monolayers of four commonly studied TMDC semiconductors on top of a SiO_2 crystal. The gain rollover at elevated carrier densities can be observed as a general behavior, while the onset and maximum value of optical gain depends on the specific valley properties of the different materials.

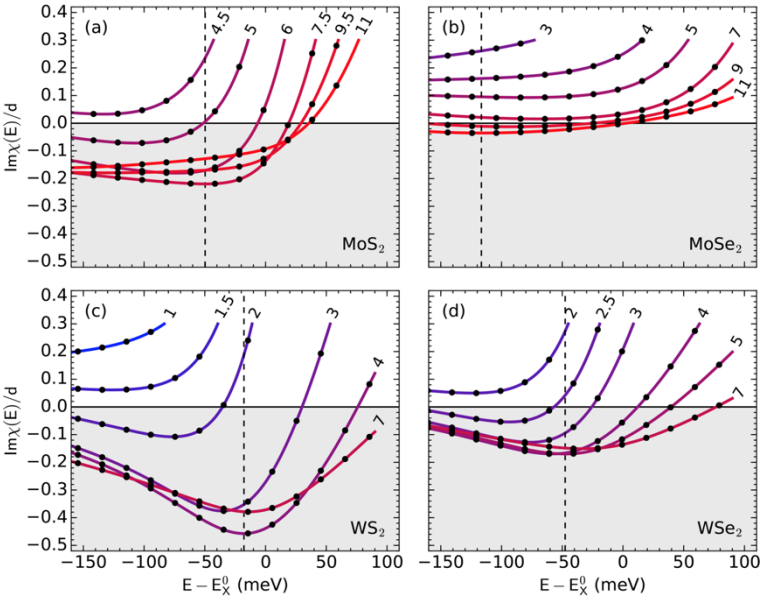

Fig. 2: Imaginary part of the dimensionless optical susceptibility for **(a)** monolayer MoS_2, **(b)** $MoSe_2$, **(c)** WS_2, and **(d)** WSe_2 on a SiO_2 substrate at T = 300 K and increasing excitation density N given in 10^{13} / cm^2. While a positive value implies absorption, optical gain is characterized by a negative imaginary part of the susceptibility (shaded region). The energy axis is chosen relative to the energy of the lowest bright exciton at zero excitation density. Vertical lines (dotted) indicate the energies at which maximum gain is achieved for each material.

Outlook

Ongoing work is concerned with the nonequilibrium dynamics of excitons in TMDC heterostructures at high excitation density and the corresponding exciton-exciton interaction effects. Exction formation and decay as well as charge transfer between different TMDC layers will be investigated using a many-body theory based on material-realistic input data.

Publications

1) A. Steinhoff, M. Florian, A. Singh, K. Tran, M. Kolarczik, S. Helmrich, A. Achtstein, U. Woggon, N. Owschimikow, F. Jahnke, X. Li, Biexciton fine structure in monolayer transition metal dichalcogenides*, Nature Physics* **14***, 1199 (2018)*

2) F. Lohof, A. Steinhoff, M. Florian, M. Lorke, D. Erben, F. Jahnke, C. Gies, Prospects and Limitations of Transition Metal Dichalcogenide Laser Gain Materials*, Nano Letters* **19**, 210 *(2019)*

6.24 hbp00038: Elektronische und Optische Eigenschaften von Halbleiter-Quantenpunkten

HLRN-Projektkennung:	hbp00038
Laufzeit:	II/2018 – III/2018
Projektleiter:	Dr. Michael Lorke
Projektbearbeiter.	Dr. Christian Carmesin, Dr. Stephan Michael, Dr. Matthias Florian
Institut / Einrichtung:	Institute for Theoretical Physics, University of Bremen

Motivation

Eine der Herausforderungen der Quanteninformationstechnologie ist die Realisierung deterministischer Einzelphotonenquellen mit hoher Wiederholungsrate und einstellbarer Emissionsenergie. Selbstorganisierte Quantenpunkte (QDs) sind vielversprechende Kandidaten aufgrund des Vorteils der Integrierbarkeit in elektrische Bauteile. Zu den aktuellen Herausforderungen gehört die systematische Erweiterung der Emissionsenergien in die verlustarmen Telekom-Bänder bei 1.3 µm und 1.5 µm. Unser Ziel ist es, InAs/(In)GaAs/GaAs QDs (s. Abb. 1) zu charakterisieren und dominante Beiträge zum Zusammenhang zwischen Morphologie und optischen Eigenschaften zu identifizieren.

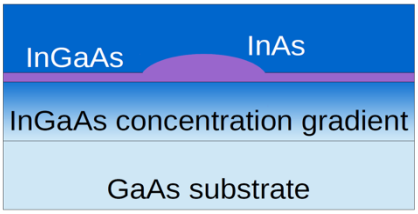

Abb. 1: Schema der verschiedenen Schichten beim Wachstum neuartiger InAs/(In)GaAs/GaAs QDs für die Emission im Telekom-Bereich. Auf ein GaAs Substrat (hellblau) wird InGaAs mit zunehmender In Konzentration gewachsen (hellblau nach dunkelblau) bis effektiv die Gitterkonstante von InP erreicht wurde. Darauf wird der QD (violett) mit einer hohen In Konzentration gewachsen.

Die theoretischen Untersuchungen im Rahmen dieses Projektes wurden in enger Kooperation mit der Arbeitsgruppe von Prof. Dr. Michler aus Stuttgart (Probenherstellung, optische Charakterisierung) sowie der Arbeitsgruppe von Prof. Dr. Andreas Rosenauer aus Bremen (Transmissions-Elektronen-Mikroskopie (TEM) Charakterisierung der Proben) durchgeführt, um die elektronischen und optischen Eigenschaften von InAlGaAs-Quantenpunkten systematisch zu analysieren.

Methoden und Ergebnisse

Für elektronische Zustandsberechnungen von Halbleiter-QDs, werden häufig sowohl Kontinuumsmodelle als auch atomistisches TB verwendet. Da die experimentellen Untersuchungen eine TEM Charakterisierung eines einzelnen QDs mit atomarer Auflösung beinhalten, haben wir uns für einen atomistischer TB-Ansatz zur Modellierung entschieden.
Die hierfür verwendete Geometrie ist in Abb. 2 zusammengefasst.

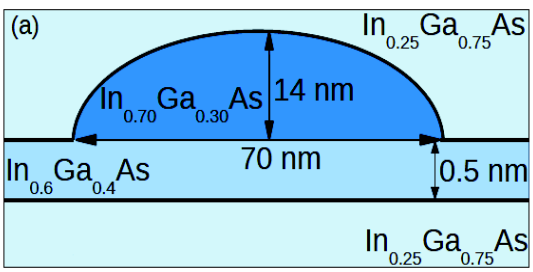

Abb. 2: Geometrie entsprechend der experimentellen Charakterisierung. Der linsen-förmige QD (dunkelblau) befindet sich auf einer wenige Atome dünnen Benetzungsschicht (helleres blau). Diese hat eine Höhe von 0.5 nm und einen reduzierten In Gehalt gegenüber dem QD. Das QD-Benetzungsschichtsystem ist in ein Barrierenmaterial mit einer noch kleineren In-Konzentration (hellblau) eingebettet.

Für die in Abb. 2 dargestellte Struktur wurde zunächst das Verspannungsfeld anhand der Valence-Force-Field-Methode berechnet (s. Abb. 3).

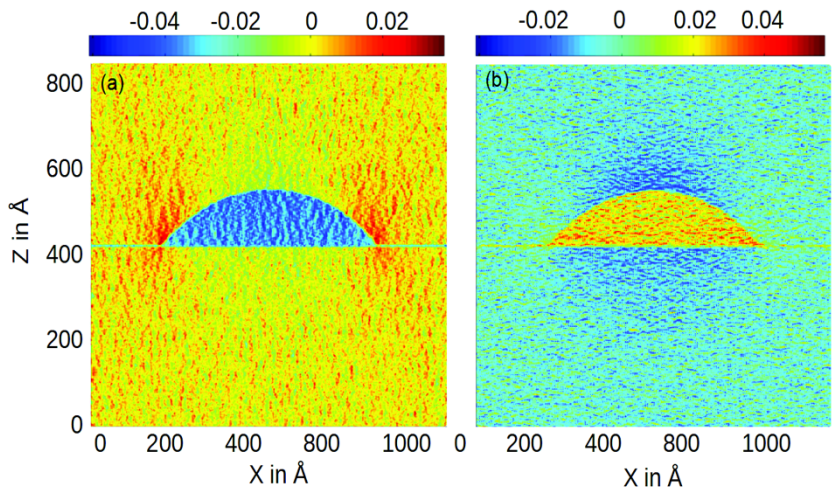

Abb. 3: (a) und (b) Berechnete Verspannungskomponenten e_{xx} and e_{zz} entlang eines Querschnitts durch das Zentrum des QDs. Innerhalb des QDs erkennt man eine Kompression in laterale Richtung (a) und eine tensile Verspannung in Wachstumsrichtung (b). Das umgekehrte Verhalten ist jeweils am Rand des QDs zu erkennen und breitet sich in das Barrierematerial aus.

Dabei werden sowohl die Bindungslängen als auch die Bindungswinkel verändert und neue Atompositionen berechnet. Diese neuen Gleichgewichtspositionen fließen über eine verallgemeinerte Harrison-Regel in das Tight-Binding-Modell als Modifikation der Kopplungsmatrixelemente ein. Das Tight-Binding-Modell bildet auf einem atomaren Gitter die experimentell bestimmte Geometrie des QDs ab, wobei der Einbau von In-Atomen durch konkrete zufällige Realisierungen gemäß dem aus TEM-Untersuchungen bestimmten Konzentrationsprofil berücksichtigt wird. Dabei wird an jedem atomaren Gitterplatz ein Satz lokalisierter orbitaler Basisfunktionen mit je zwei Spinrichtungen sowie Spin-Orbit-Kopplung berücksichtigt. Die Diagonalisierung des Tight-Binding-Hamiltonians liefert die Eigenenergien und Eigenzustände der gebundenen Elektronen- und Loch-Zustände im QD. Die Energiedifferenz zwischen dem tiefsten gebundenen Elektron und Loch liefert die Einteilchen (Quasiteilchen) Bandlücke.

Ausgehend von der in Abb.2 dargestellten Struktur haben wir die Einflüsse von Größen- und In-Konzentrationsschwankungen auf die Emissionsenergie untersucht. Für die Analyse von Größenfluktuationen haben wir in verschiedenen Rechnungen einzelner QDs die Größe variiert, indem jeweils ein konstantes Verhältnis von Durchmesser zu Höhe für jeden QD beibehalten wurde. Für eine Analyse der Konzentrationsfluktuationen haben wir in verschiedenen Berechnungen für einzelne QDs die In-Konzentration innerhalb des QDs variiert, wobei die Größe unverändert blieb. Die Ergebnisse zu dieser Untersuchung sind in Abb 4. dargestellt.

Man erkennt anhand von Abb. 4, dass Konzentrationsfluktuationen einen erheblich stärkeren Einfluss auf die Übergangsenergien haben als die Größenfluktuationen. Der Grund für den vergleichsweise geringen Einfluss der Größenfluktuationen ist, dass es sich um einen relativ großen QD handelt. Für solch vergleichsweise große QD ist nicht zu erwarten, dass Größenfluktuationen von +-10% einen erheblichen Einfluss auf die Emissionsenergie haben. Dies kann intuitiv mit dem einfachen Potenzialtopf-Modell veranschaulicht werden, bei dem der Einfluss der Emissionsenergie mit mit dem Radius r abnimmt. Legt man dieses vereinfachte Modell zugrunde, so entspricht die Situation eines relativ großen QDs der Asymptote der $1/r^2$ Abhängigkeit des Potentialtopf-Modells.

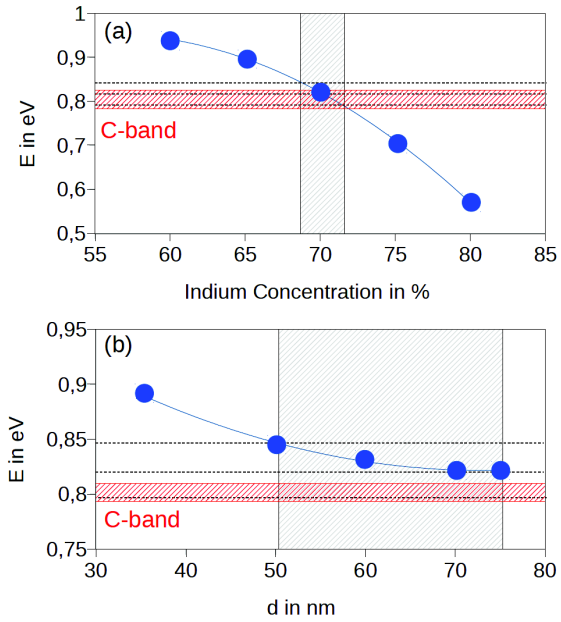

Abb. 4: Variation der Einteilchen Bandlücke E für verschiedene In Konzentration innerhalb des QDs (a) und für verschiedene QD Durchmesser mit konstantem Verhältnis von Durchmesser zu Höhe (b). Die dunkel schraffierten Bereiche markieren Variationen der In Konzentration innerhalb des QDs und Änderungen des QD Durchmessers um die Referenzgeometrie aus Abb. 2 gemäß der experimentell beobachteten inhomogenen Verbreiterung. Das entsprechende Energieintervall wird durch die obere und untere horizontale Linie markiert. Die horizontale Linie dazwischen markiert die Einteilchen Emissionsenergie der Referenzgeometrie von Abb. 2. Diese Einteilchen Energien werden in Wirklichkeit um die Exziton Bindungsenergie (Ex = 10 meV) abgesenkt, was die berechneten Einteilchen Energien in das rot markierte Telekomband schiebt.

Für das Emissionsspektrum des vorliegenden Quantenpunktensembles, das aus selbstorganisiert gewachsenen Quantenpunkten mit unterschiedlichen Größen und In-Konzentrationen besteht, bedeuten die Ergebnisse, dass Änderungen der Emissionsenergie durch starke Größenfluktuationen und bereits geringe Konzentrationsfluktuationen hervorgerufen werden können. Da für die Quanteninformationstechnologie eine scharfe Emission im Telekom Band eine wichtige Eigenschaft darstellt, ist es von Interesse die Einflüsse auf die Emissionsenergie der Quantenpunkte zu untersuchen und zu verstehen.

Alternatives Materialsystem: Atomar dünne Übergangsmetalldichalkogenide

In einem weiteren Projekt haben wir Einzelphotonenemission aus atomar dünnen Übergangsmetalldichalkogenid (TMD) Nanostrukturen untersucht. Der dafür notwendige Ladungsträgereinschluss wurde bisher mit Defekten und Verspannung in Verbindung gebracht, wobei offene Fragen zum mikroskopischen Ursprung bleiben. Anhand unserer durchgeführten Simulationen konnten wir zeigen, dass die Biegesteifigkeit dieser Materialien zu lokalem Knittern solcher zweidimensionaler Lagen führt. Das resultierende Verspannungsfeld führt aufgrund der starken Abhängigkeit der elektronischen Bandlücke zu einem Ladungsträgereinschluss. Dieser hängt zusätzlich von Änderungen der dielektrischen Umgebung ab. Wir zeigen, dass das Zusammenspiel von lokalem Knittern, Verspannung und dielektrischer Umgebung die elektronischen und optischen Eigenschaften in TMD Nanostrukturen bestimmt. Dies demonstrieren wir am am Beispiel von quantenpunktartigen MoS2 Nanoblasen. Diese bilden sich, wenn TMD Monolagen auf Substrate oder andere zweidimensionalen Materialien gebracht werden.

Für unsere Untersuchung modellieren wir eine TMD Nanoblase mit atomarer Auflösung in einer Superzellrechnung. Basierend auf Valence-Force Simulationen erhalten wir neue Gleichgewichtspositionen der einzelnen Atome in der deformierten Lage. Die betrachtete Geometrie ist in Abb. 1 (a) dargestellt. In unserer Analyse betrachten wir Nanoblasen mit unterschiedlichem Durchmesser zu Radius Verhältnis h/r sowie Blasen unterschiedlicher Größe. Der Lokalisierungsgrad der Wellenfunktion ist durch das Verhältnis h/r bestimmt, wie in Abb. 1 (b) gezeigt. Im Gegensatz dazu ändert die Größe der Nanoblasen das qualitative Verhalten nicht. Für h/r = 0,1 sind die Einteilchenzustände delokalisiert entlang des Randes der der Blase, während für ein zunehmendes Verhältnis von h/r =0,15 Maxima mit der C3v Symmetrie des unterliegenden Kristallgitters auftreten. Der Trend von stärkerer Lokalisierung

mit zunehmendem Verhältnis von h/r bestätigt sich für h/r =0,175. In diesem Fall sind die Aufenthaltswahrscheinlichkeiten auf drei Positionen am Rand der Blase beschränkt.

Abbildung 1 (c) zeigt die Emissionsspektren zu den drei verschiedenen Situationen in 1 (b). Für h/r=0,1 ist die Oszillatorstärke sehr schwach aufgrund der viel größeren radialen Ausdehnung der Wahrscheinlichkeitsdichten der Elektronen gegenüber den Löchern, was kleine Übergangsdipolmatrixelemente zur Folge hat. Für ein zunehmendes Verhältnis von h/r entsteht eine größere Verspannung, die zu einem tieferen Ladungsträgereinschluss, einer

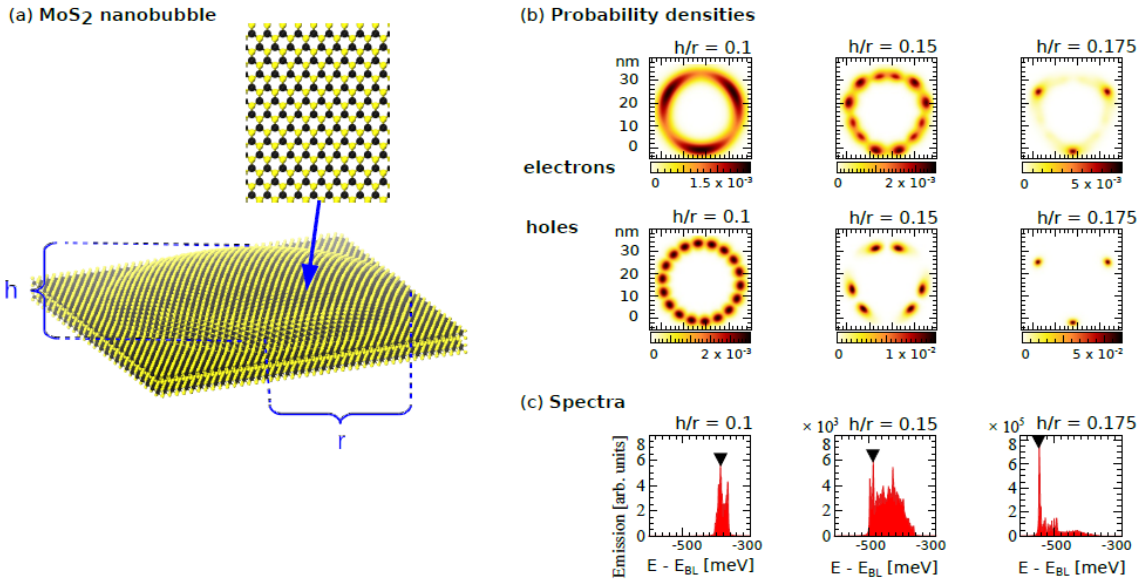

Abb. 5: (a) MoS2-Nanoblasen mit Radius r und Höhe h. (b) Aufsicht der Wahrscheinlichkeitsdichten für Elektronen und Löcher, die für den stärksten optischen Übergang verantwortlich sind, der jeweils in (c) markiert ist. Die Ergebnisse sind für einen Blasenradius von r = 18nm und verschiedene Verhältnisse von h/r gezeigt. (c) Emissionsspektren, berechnet aus Fermis goldener Regel, basierend auf den tight-binding Zuständen in (b).

stärkeren Lokalisierung und einer Rotverschiebung der optischen Spektren führt. In unserer Analyse der starken Lokalisierung quantifizieren wir die Beiträge der Verspannung sowie der dielektrischen Umgebung zum Einschlusspotential. Infolge der Nanoblasengeoemtrie , wie in Abb. 2 (c) gezeigt, entspricht die dielektrische Situation außerhalb der Blase einer Bilage, wogegen in der Mitte der Blase für große Abstände zwischen der oberen und unteren Schicht die Situation einer Monolage ähnelt. Dieser Effekt nimmt mit zunehmender Höhe hmax der Blase zu, wie in Abb. 2 (c) dargestellt. Die resultierenden Änderungen der lokalen Bandlücke sind in Abb. 2 (d) dargestellt. Effektiv führen diese zu einem repulsiven Potenzial in der Mitte der Blase.

Die verspannungsinduzierten Änderungen der Bandlücke für drei verschiedene Verhältnisse von h/r sind in Abb. 2 (a) dargestellt. Durch den Vergleich mit den Wahrscheinlichkeitsdichten in Abb. 1 (b) können wir folgern, dass die Verspannung für die zunehmende Lokalisierung verantwortlich ist, da der dielektrische Einfluss rotationssymmetrisch ist (s. Abb. 2 (d)). Für Verhältnisse von h/r =0,15 und 0,175 werden Bereiche großer Verspannung ('Pockets') identifiziert. Um dies zu erklären wird die in Abb. 2 (b) dargestellte Normal-Normal-Korrelationsfunktion bestimmt. Diese beschreibt den mittleren Winkel zwischen Normalenvektoren benachbarter Elementarzellen (schematisch dargestellt in Abb. 2 (c)). Diese Winkel zeigen ein lokales Knittern der Oberfläche für Verhältnisse von h/r = 0,15 und 0,175. Ein Vergleich zwischen den Abb. 2 (a) und (b) zeigt,

dass sich die Verspannung nicht gleichmäßig verteilt und in den 'Pockets' am stärksten ist. Dieses Verhalten lässt sich auf das hohe Young-Modul von MoS2 zurückführen. Je höher das Modul, desto besser widersteht ein Material Kompression/Dehnung. Speziell für ein hohes Modul neigt das Material dazu, seine Gesamtlängenänderung zu minimieren. Dies ist insbesondere durch die Bildung von lokalem Knittern möglich. Die starke Änderung der Bandlücke, induziert durch Verspannung und dielektrische Umgebung, ändert auch die Oszillatorstärke der optischen Übergänge in Abb. 1 (c). Der Hauptgrund für diese Änderung ist in Abb. 2 (e) dargestellt. Bei gleichbleibendem Bandcharakter der Elektronzustände d_z^2 ändert sich der Charakter der Lochzustände, was entweder schwache Oszillatoratärken (bei gleichem Charakter d_z^2) oder starke Übergänge (bei unterschiedlichem Charakter d_{xy}) zur Folge hat.

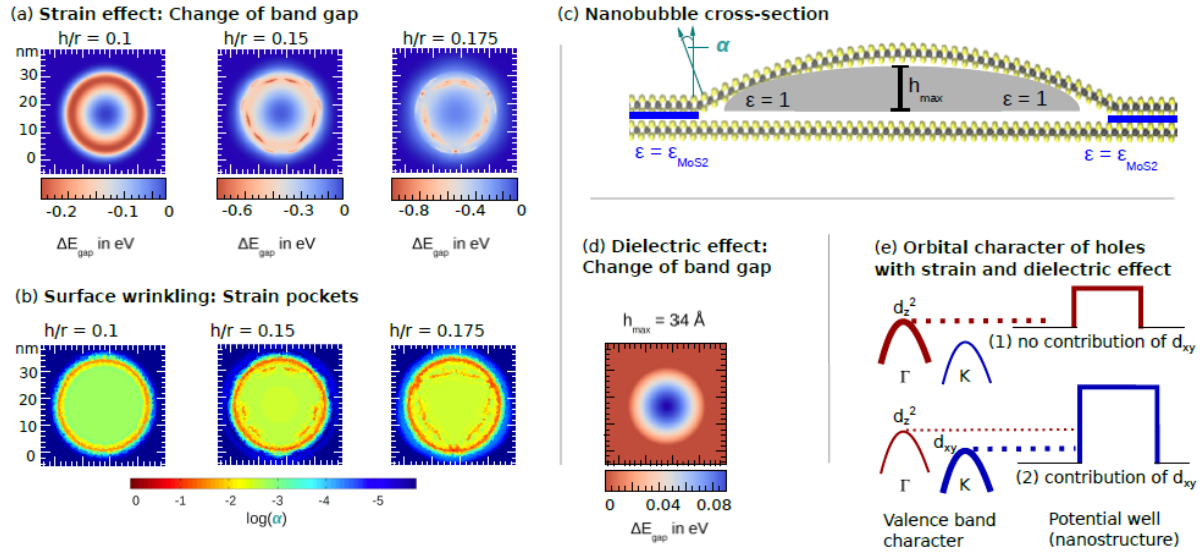

Abb. 6: (a) Verspannungsinduzierte Bandlückenänderung für verschiedene Verhältnisse von h/r. (b) Durchschnittlicher Winkel (im Bogenmaß) zwischen Normalenvektoren benachbarter Elementarzellen zeigen ein Knittern, das den räumlich lokalisierten 'Pockets' entspricht. (c) Querschnitt durch die Blase mit der Höhe hmax. Die geometrische Situation impliziert eine Änderung der dielektrischen und elektronischen Umgebung für die MoS2-Schicht, die die Nanoblase bildet. Die grünen Pfeile schließen einen Winkel zwischen Normalvektoren benachbarter Elementarzellen auf der diskretisierten Oberfläche ein. (d) Repulsives Potential innerhalb der Nanoblase mit Höhe hmax = 3,4nm als Ergebnis der modifizierten dielektrischen und elektronsichen Umgebung. (e) Schematische Darstellung des Orbitalcharakters lokalisierter Lochzustände. Für einen flachen Einschluss dominiert der d_z^2 Charakter, wogegen für einen tieferen Einschluss d_{xy} beimischt.

Ausblick

In einem Folgeprojekt ist geplant, die im Rahmen dieses Projektes entwickelten Methoden, Erkenntnisse und Untersuchungsabläufe auf alternative Halbleiter QD Materialsysteme für Einzelphotonenemission im Telekombereich anzuwenden. Im Bereich der TMDs ist geplant weitere Nanostrukturen zu untersuchen, um mit einem tieferen Verständnis der auftretenden Mechanismen und Effekte die Eigenschaften solcher Systeme zu optimieren und neue Möglichkeiten der Ladungsträgerlokalisierung für die Generation von Einzelphotonenquellen vorzuschlagen.

Publikationen

C. Carmesin, F. Olbrich, T. Mehrtens, M. Florian, S. Michael, S. Schreier, C. Nawrath, M. Paul, J. Höschele, B. Gerken, J. Kettler, S. L. Portalupi, M. Jetter, P. Michler, A. Rosenauer, and F. Jahnke, Phys. Rev. B **98**, 125407 (2018)
C. Carmesin, M. Lorke, M. Florian, D. Erben, A. Schulz, T. O. Wehling and F. Jahnke, arXiv:1902.05001 (2019)

6.25 hbp00041: Multi-messenger Signals from Compact Objects

HLRN-Projektkennung:	hbp00041
Laufzeit:	I/2018 – IV/2018
Projektleiter:	Prof. Dr. Claus Lämmerzahl[1]
Projektbearbeiter.	Prof. Dr. Stephan Rosswog[2], Mr. Emanuel Gafton[2], Mr. Davide Gizzi[2]
Institut / Einrichtung:	1: ZARM, University of Bremen, Am Fallturm, 28359 Bremen, Germany 2: Department of Astronomy and Oskar Klein Centre, Stockholm University, Sweden

Background

On August 17, 2017, the long-awaited era of "Multi-Messenger Astrophysics", where a gravitational wave event is observed simultaneously via complementary channels, has spectacularly begun: a neutron star merger gravitational wave signal flooded the LIGO detectors for several 10s of seconds and over the following weeks the aftermath of the event was observed electromagnetically from gamma-rays over optical to radio wave lengths. The gravitational wave signal revealed the nature of the source while the electromagnetic signature allowed to localize the event and in addition also provided an independent measurement of the Hubble constant H_O [1]. This event is the first ever detected gravitational wave source caused by matter (as opposed to black holes which are just manifestations of space and time) and it has brought major leaps forward in several areas:

1. *Merging neutron stars do indeed cause short gamma-ray bursts (GRBs)*
   This connection had been suspected based on a number of *indirect* arguments since the 1980ies. Such a short GRB has been observed 1.7 s after the GW-signal.
2. *Constraining alternative theories of gravity*
   The delay between the gravitational wave peak and the gamma-rays showed that gravitational waves travel at the speed of light to within 1 part in 10^{15} and thus placed strong constraints on alternative theories of gravity [2].
3. *A new path to Cosmology*
   The first gravitational wave plus electromagnetic observation allowed for an alternative determination of the Hubble parameter [1] and has therefore established binary neutron star mergers as a powerful new distance indicator for probing the cosmological expansion history.
4. *Constraining nuclear matter by gravitational wave signals*
   The tidal deformation of the neutron stars as they approached each other left a subtle tidal imprint in the GW signal. This deviation from a point particle pattern allowed to constrain the properties of nuclear matter at high densities [3].
5. *Merging neutron stars are major sources of the heaviest elements ("r-process")*
   This had been shown in theoretical calculations by one of the PIs of this proposal and his collaborators, e.g. [17, 15, 5, 10, 13, 12] many of these calculations were actually performed on HLRN resources. We could show in particular [16] that the decay of the observed luminosity is in excellent agreement with the radioactive decays from r-process, see Fig. 1.

For all these reasons, this electromagnetic association of a binary neutron-star merger was celebrated by Science Magazine as "Breakthrough of the year 2017". Within the first 18 months since discovery, this transient has been the subject of over 300 papers, of which 16 published in Nature or Science.

Scientific Goals

The goal of the HLRN-project "Multi-messenger Signals from Compact Objects" (project number hbp00041) is to make predictions for the multi-messenger signatures of gravitational wave sources. These include high-frequency sources ($f_{GW} > 10\ Hz$) that are accessible by the currently operating (LIGO-VIrgo) and future ground-based detectors (e.g. the Einstein Telescope), but also by the future space-based observatory LISA. The most important sources for the first type of detector are binary systems of *merging* black holes and neutron stars. The second type of detectors will be sensitive to a much lower frequency range 10^{-4} < f_{GW} < 0.1 Hz) and will therefore see different sources, such as *orbiting* binaries of two white dwarfs or massive black holes or potentially also massive black holes disrupting stars.

Our current focus is on the understanding of the multi-messenger signals of two neutron stars and on tidal disruption events (TDE) where a star passing too close to a massive black hole is ripped apart by the hole's tidal forces.

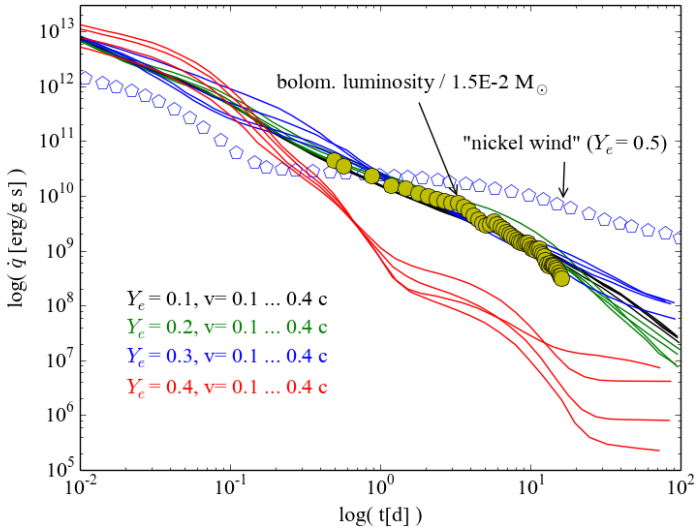

Figure 1: Interpretation of the first ever observed neutron star merger. Apart from gravitational waves, this event was also observed electromagnetically. The total emitted electromagnetic emission ("bolometr. luminosity" in the figure) is consistent with having been produced by the decay for freshly synthesized heavy elements (blue, black and green curves). Figure from Rosswog et al. (2018).

Recent Results

We have been heavily involved in the interpretation of the first detected neutron star merger event [7, 9, 4, 11, 16, 8]. In the late 1990ies we had performed the first ever neutron star merger plus nucleosynthesis calculations [14, 5, 15], and could show that such mergers eject enough material to be the major cosmic production site and that the ejecta are indeed made of heavy, rapid neutron capture ("r-process") elements, at that time an "exotic idea". The first detected neutron star merger now proved exactly this idea: the decay of its electromagnetic emission, the yellow filled circles in Fig. 1 are in excellent agreement with our predictions for r-process material (black, blue and green lines), but not with non-r-process material (e.g. red lines and blue pentagon). This solves a problem that has puzzled astrophysicists for six decades!

We have further performed the first systematic study of how the black hole spin impacts on the tidal disruption of a star [6]. Fig. 2 shows the disruption of a solar-type star by a massive black hole 10^6 solar masses). The disrupted stellar matter for the case of non-spinning ("Schwarzschild") black holes is shown in the first line, spinning ("Kerr") black holes both for prograde spins are shown in the second line and retrograde spins in the third line.

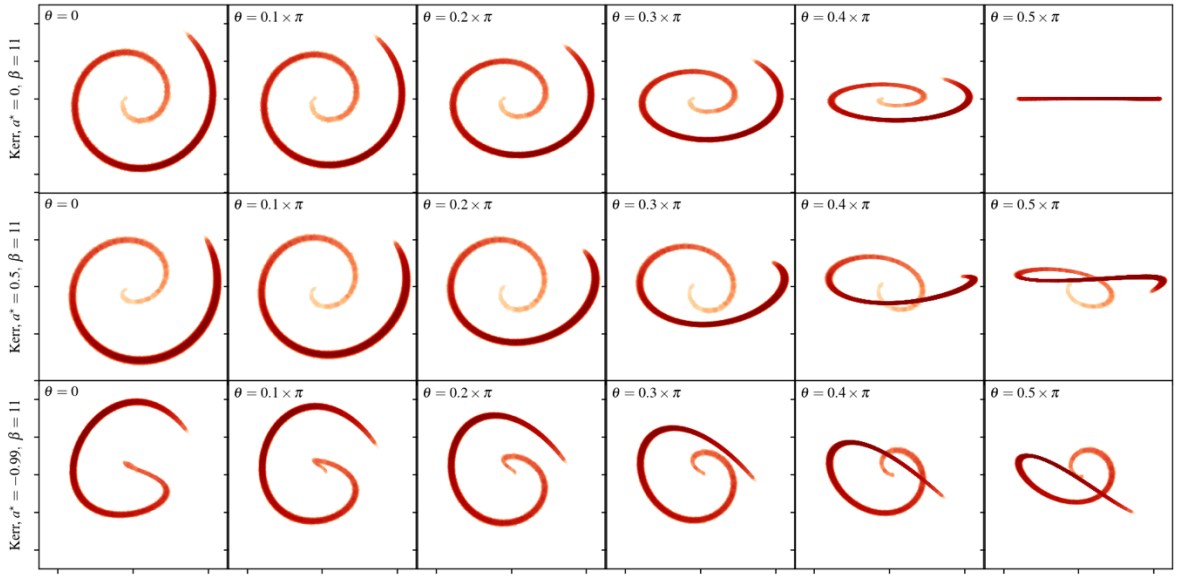

Figure 2: Tidal disruption of a Sun-like star by a supermassive rotating, "Kerr" black hole. The dimensionless spin parameter of the Kerr black hole is denoted as a^* on the y-axis, the strength by the parameter β (marginal disruption occurs at β ≈ 1, very strong encounters β > 1). Figure from Gafton and Rosswog (2019).

Outlook

We are currently enriching our models with more physics to be prepared for the interpretation of the next wave of incoming gravitational wave plus additional messengers detections. At the time of writing this report, the next observation run of the LIGO-Virgo detectors is one month in the future and we are eagerly awaiting what new results will be brought to light.

Publications and Dissemination

a) Publications resulting from HLRN simulations

- *Tidal disruptions of stars by rotating black holes: effects of spin and impact parameter,*
  E. Gafton and S. Rosswog, to be submitted to MNRAS in March 2019
- *Spitzer Mid-Infrared Detections of Neutron Star Merger GW170817 Suggests Synthesis of the Heaviest Elements*
  M. Kasliwal et al., MNRAS in press, arXiv:1812.08708 (2019)
- *Impact of ejecta morphology and composition on the electromagnetic signatures of neutron star mergers*
  R. Wollaeger et al., MNRAS 478, 3298 (2018)
- *The first direct double neutron star merger detection: Implications for cosmic nucleosynthesis*
  S. Rosswog et al., A \& A 615, 132 (2018)

b) Presentation of HLRN Results at conferences and colloquia

- *Neutron star mergers as heavy element production site*
  Plenary Talk, Marcel Grossmann Meeting, Rome, Italy, July 02-06, 2018
- *R-process in Neutron star mergers*
  Invited talk, Nuclei in the Cosmos, L'Aquila, Italy, June 29, 2018
- *Heavy elements and electromagnetic transients from neutron star mergers*
  Royal Society Meeting, London, Mai 11, 2018
- *Neutron star binary - simulations*
  10th Sackler Conference in Theoretical Astrophysics, Harvard, May 07-09, 2018
- *Neutron Star mergers and the beginning of multi-messenger astrophysics*
  ``Neutron stars in Lisbon'', Lisbon, Portugal, April 12, 2018
- *Neutron Star mergers and the beginning of multi-messenger astrophysics*
  European Week of Astronomy, Liverpool, UK, April 06, 2018
- *Neutron star mergers as factories for cosmic nucleosynthesis*
  Albert Einstein Institute, Potsdam, March 28, 2018
- *Multi-messenger astrophysics with merging neutron stars*
  Russbach Winter School on Nuclear Astrophysics, Russbach, Austria, March 23, 2018
- *Neutron star mergers and the begin of multi-messenger astrophysics*
  plenary talk, German Physical Society (DPG), Materie und Kosmos, Würzburg, Germany, March 19, 2018
- *Neutron star mergers and the begin of multi-messenger astrophysics*
  plenary talk, German Physical Society (DPG), Physik der Hadronen und Kerne, Bochum, Germany, March 01, 2018
- *Multi-messenger signals from gravitational wave sources*
  Physics Colloquium, Louisiana State University, USA, Feb 22, 2018
- The beginning of the multi-messenger astrophysics era
  Physics Colloquium, Florida State University, Tallahassee, USA, Jan 25, 2018
- *Multi-messenger signals from gravitational wave sources*
  Physics Colloquium, Georgia Tech, Atlanta, USA, Jan 23, 2018
- *Multi-messenger signals from gravitational wave sources*
  Deciphering the Violent Universe, Playa del Carmen, December 11-15, 2017

References

[1] B. P. Abbott, R. Abbott, T. D. Abbott, F. Acernese, K. Ackley, C. Adams, T. Adams, P. Addesso, R. X. Adhikari, V. B. Adya, et al., A gravitational-wave standard siren measurement of the Hubble constant, Nature,551 (2017) 85-88.

[2] B. P. Abbott, R. Abbott, T. D. Abbott, F. Acernese, K. Ackley, C. Adams, T. Adams, P. Addesso, R. X. Adhikari, V. B. Adya, et al., Gravitational Waves and Gamma-Rays from a Binary Neutron Star Merger: GW170817 and GRB 170817A, ApJL 848 (2017) L13.

[3] B. P. Abbott, R. Abbott, T. D. Abbott, F. Acernese, K. Ackley, C. Adams, T. Adams, P. Addesso, R. X. Adhikari, V. B. Adya, et al., GW170817: Observation of Gravitational Waves from a Binary Neutron Star Inspiral, Physical Review Letters 119 (16) (2017) 161101.

[4] P. A. Evans, S. B. Cenko, J. A. Kennea, S. W. K. Emery, N. P. M. Kuin, O. Korobkin, R. T. Wollaeger, C. L. Fryer, K. K. Madsen, F. A. Harrison, Y. Xu, E. Nakar, K. Hotokezaka, A. Lien, S. Campana, S. R. Oates, E. Troja, A. A. Breeveld, F. E. Marshall, S. D. Barthelmy, A. P. Beardmore, D. N. Burrows, G. Cusumano, A. D'Ai, P. D'Avanzo, V. D'Elia, M. de Pasquale, W. P. Even, C. J. Fontes, K. Forster, J. Garcia, P. Giommi, B. Grefenstette, C. Gronwall, D. H. Hartmann, M. Heida, A. L. Hungerford, M. M. Kasliwal, H. A. Krimm, A. J. Levan, D. Malesani, A. Melandri, H. Miyasaka, J. A. Nousek, P. T.

O'Brien, J. P. Osborne, C. Pagani, K. L. Page, D. M. Palmer, M. Perri, S. Pike, J. L. Racusin, S. Rosswog, M. H. Siegel, T. Sakamoto, B. Sbarufatti, G. Tagliaferri, N. R. Tanvir, A. Tohuvavohu, Swift and NuSTAR observations of GW170817: Detection of a blue kilonova, Science 358 (2017) 1565{1570.

[5] C. Freiburghaus, S. Rosswog, F.-K. Thielemann, R-process in neutron star mergers, ApJ 525 (1999) L121.

[6] E. Gafton, S. Rosswog, Tidal disruptions by rotating black holes: effects of spin and impact parameter, to be submitted to MNRAS.

[7] C. Gall, J. Hjorth, S. Rosswog, N. R. Tanvir, A. J. Levan, Lanthanides or Dust in Kilonovae: Lessons Learned from GW170817, ApJL 849 (2017) L19.

[8] M. M. Kasliwal, D. Kasen, R. M. Lau, D. A. Perley, S. Rosswog, E. O. Ofek, K. Hotokezaka, R.-R. Chary, J. Sollerman, A. Goobar, D. L. Kaplan, Spitzer Mid-Infrared Detections of Neutron Star Merger GW170817 Suggests Synthesis of the Heaviest Elements, MNRAS.

[9] M. M. Kasliwal, E. Nakar, L. P. Singer, D. L. Kaplan, et al., Illuminating gravitational waves: A concordant picture of photons from a neutron star merger, Science 358 (2017) 1559-1565.

[10] O. Korobkin, S. Rosswog, A. Arcones, C. Winteler, On the astrophysical robustness of the neutron star merger r-process, MNRAS 426 (2012) 1940-1949.

[11] J. D. Lyman, G. P. Lamb, A. J. Levan, I. Mandel, N. R. Tanvir, S. Kobayashi, B. Gompertz, J. Hjorth, A. S. Fruchter, T. Kangas, D. Steeghs, I. A. Steele, Z. Cano, C. Copperwheat, P. A. Evans, J. P. U. Fynbo, C. Gall, M. Im, L. Izzo, P. Jakobsson, B. Milvang-Jensen, P. O'Brien, J. P. Osborne, E. Palazzi, D. A. Perley, E. Pian, S. Rosswog, A. Rowlinson, S. Schulze, E. R. Stanway, P. Sutton, C. C. Thöne, A. de Ugarte Postigo, D. J. Watson, K. Wiersema, R. A. M. J. Wijers, The optical afterglow of the short gamma-ray burst associated with GW170817, Nature Astronomy 2 (2018) 751-754.

[12] A. Perego, S. Rosswog, R. M. Cabezón, O. Korobkin, R. Käppeli, A. Arcones, M. Liebendörfer, Neutrino-driven winds from neutron star merger remnants, MNRAS 443 (2014) 3134-3156.

[13] S. Rosswog, O. Korobkin, A. Arcones, F.-K. Thielemann, T. Piran, The long-term evolution of neutron star merger remnants - I. The impact of r-process nucleosynthesis, MNRAS 439 (2014) 744-756.

[14] S. Rosswog, M. Liebendörfer, F.-K. Thielemann, M. Davies, W. Benz, T. Piran, Mass ejection in neutron star mergers, in: Proceedings of the 2nd Oak Ridge Symposium on Atomic and Nuclear Astrophysics, 1998.

[15] S. Rosswog, M. Liebendörfer, F.-K. Thielemann, M. Davies, W. Benz, T. Piran, Mass ejection in neutron star mergers, A & A 341 (1999) 499-526.

[16] S. Rosswog, J. Sollerman, U. Feindt, A. Goobar, O. Korobkin, R. Wollaeger, C. Fremling, M. M. Kasliwal, The first direct double neutron star merger detection: Implications for cosmic nucleosynthesis, A&A 615 (2018) A132.

[17] S. Rosswog, F. K. Thielemann, M. B. Davies, W. Benz, T. Piran, Coalescing Neutron Stars: a Solution to the R-Process Problem?, in: W. Hillebrandt, E. Muller (eds.), Nuclear Astrophysics, 1998, p. 103.

6.26 hbp00045: Non-local manipulation of correlation effects in 2D Transition Metal Dichalcogenides

HLRN Project ID:	hbp00045
Run time:	II/2017 – I/2019
Project Leader:	Prof. Dr. T. Wehling
Project Scientists:	C. Steinke, J. Berges, N. Witt, Dr. E. Kamil
Affiliation:	Institut für Theoretische Physik and Bremen Center for Computational Materials Science, Universität Bremen

Overview

Recent theoretical [1] and experimental works [2] have introduced the idea of a novel type of heterojunctions within two-dimensional (2D) materials based on the idea of manipulation of the Coulomb interaction through laterally structured substrates as depicted in Fig. 1. These so called Coulomb engineered heterostructures show spatial property changes, like different band gaps, within an otherwise homogeneous monolayer.

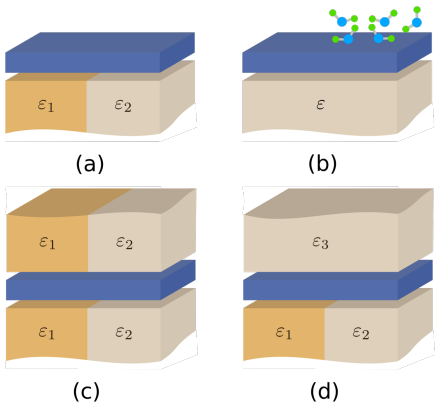

Fig. 1*:* Sketches of a monolayer (blue) in different laterally structured environments.

To predict suitable 2D materials for practical applications, a profound theoretical insight into the processes is necessary. By means of material realistic models based on ab-initio calculations we studied semiconducting transition metal dichalcogenides (TMDCs) placed in different dielectric environments. From this we want to identify optimal candidates for Coulomb engineering in this material class. We found significant band gap reductions with increasing external screening for all investigated materials. Furthermore, we studied the internal limits of the length-scale of possible band gap transitions showing that possible interface regions can be on the order of a few unit cells.

As all real materials contain structural defects which change the material's physical and chemical properties, a profound understanding of their influence is necessary. With this knowledge the application of defect engineering becomes accessible to specifically control and modify the properties of a material. In 2D materials, especially TMDCs, recent research on defect engineering [3] demonstrates that defects can alter e.g. electronical structures, magnetic behaviour or optical properties, but also that many parts of this field are still not fully understood and need further investigations.

In this regard, we study point defects in TMDCs like substitutional atoms or surface adatoms. Using ab-initio calculations we derive a multi-scale approach to describe the defect induced potential with material realistic models. Moreover, using those models we investigate the change of the defects properties in different dielectric environments to characterize the applicability of defects in the context of Coulomb engineering. We find significant change in ionization energies and spatial extension of bound impurity states depending on external screening.

Besides the work on the semiconducting TMDCs, another part of this project is dedicated to the metallic representatives of this class of materials. Here, we focus on the description of many-body instabilities, particularly the formation of periodic lattice distortions, that are driven by interaction processes involving the low-energy electrons. Again, our approach is based on minimal, yet material-realistic lattice models whose parameters are obtained from ab-initio calculations, not only for the electronic but also for the lattice degrees of freedom. The latter constitute the computationally most expensive step of our scheme, where we greatly benefit from the facilities provided by HLRN. In this report, we outline the results of two subprojects, one on the electronic and crystal structure of a monolayer of 1T-$NbSe_2$ in the so-called Star-of-David-reconstructed phase, the other on the renormalization of phonon dispersions within the model framework.

Results

Material realistic approach to Coulomb engineering

Substrates can significantly change the band gap of a material due to external screening of the Coulomb interaction. To find suitable materials for the creation of heterostructures, we have to investigate how strongly the band gap in different materials can be manipulated. Therefore we studied semiconducting TMDCs MX_2 with $M \in \{Mo, W\}$ and $X \in \{S, Se\}$ on different homogeneous substrates. We performed G_0W_0 ab-initio calculations implemented in VASP [4] of the freestanding monolayer and incorporated the dielectric environment through a GΔW like approach [5]. The substrate screening is taken into account via the WFCE [6] method for which we derived the needed Coulomb interaction terms of freestanding monolayers by means of RPA calculations from VASP calculations.

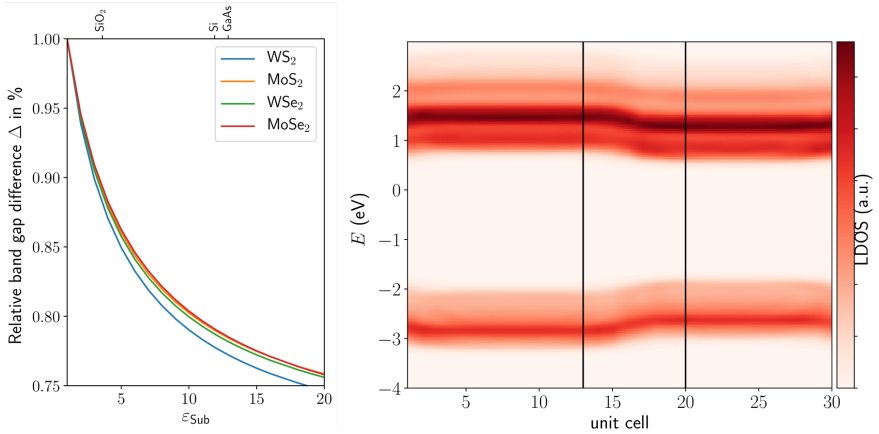

Fig. 2: a) Relative band gap reduction for different TMDCs for various substrates with the dielectric constant ε_{Sub}. b) Local density of states of WS_2 on a laterally structured substrate with $\varepsilon = 1$ in the left region and $\varepsilon = 10$ in the right region.

The resulting relative band gap reductions with the band gap of a freestanding monolayer being “1” is shown in Fig. 2a). We find significant band gap reductions with increasing screening for all TMDCs. All materials show roughly the same reduction. For example a SiO_2 substrate will reduce the band gap to ~ 87 % of the native band gap independent of the 2D material showing that all semiconducting TMDCs are equally applicable for Coulomb engineering.

Additionally we investigated Coulomb engineered heterostructures. The local density of states of WS_2 placed on a spatially structured substrate with $\varepsilon = 1$ in the left region and $\varepsilon = 10$ in the right region is shown in Fig. 2b). The valence and conduction band edges are shown as darker red areas. The band gap region is light red. We found a clear spatial band gap

modulation of a Type I heterojunction with a length-scale of the interface of around 7 unit cells (marked with black lines). Thus the interface region due to intrinsic limits is rather small making extrinsic limitations as the structured substrates more important for the application of Coulomb engineered heterostructures.

Manipulation of Defect Potentials in 2D materials

Structural defects in solids can manifest in many different constellations and dimensionalities. As we are interested in electronical properties of TMDCs and their manipulation, we first considered a substitutional atom which is a zero dimensional point defect for 2D materials. The model system we investigated was a MoS_2 monolayer with a rhenium atom substituting a molybdenum atom. We used DFT calculations to extract the defect potentials by evaluating the orbital projected density of states. These potentials were fitted with a strictly 2D Keldysh potential model [7]. To describe external screening, the model potential was modified to include the dielectric properties of the surrounding environment. The application of the effective mass approximation in a 2D Schrödinger equation was used to calculate bound impurity states and ionization energies for different dielectric substrates.

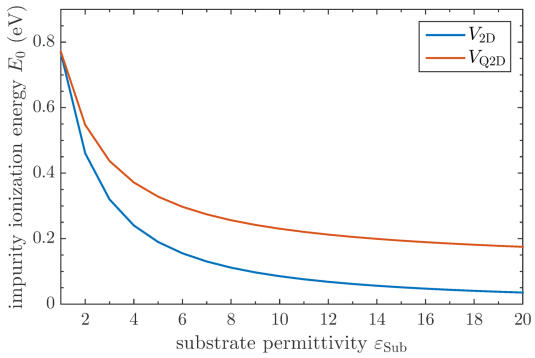

Fig. 3: Ionization energy of the rhenium impurity depending on the dielectric environment.

Moreover, a more material realistic "quasi 2D" (Q2D) model for the defect potential with a finite slab height was employed by using the already acquired model's parameters. The same calculations for the impurity levels were performed and the results for the ionization energies depending on the substrate permittivity are illustrated for both applied models in Fig. 3. We find that by introducing external screening the ionization energies of the impurity and thus the needed activation energy for a conducting state can be reduced significantly by ~ 75 %.

Further investigations regarding representability of the researched impurity and applicability to other point defects and materials is still needed. Therefore, calculations on Alkali adatoms are performed and still need evaluation. First results, however, show promising similarities which gives rise to the assumption that this multi-scale approach can be employed on other material systems and possibly material classes as well.

Electronic structure of monolayer 1T-$NbSe_2$

In 2016, a single layer of 1T-$NbSe_2$ has been experimentally found to be an insulator [8], despite the fact that band theory predicts a metal. Using *ab initio* calculations we reveal the nature of this insulating state. Structural relaxation of a $\sqrt{13} \times \sqrt{13}$ supercell leads to a Star-of-David reconstruction with an energy gain of 60 meV per primitive unit cell. The band structure of this phase exhibits a half-filled flat band which is associated with orbitals that are delocalized over several atoms in each star. By including many-body corrections through a combined GW, hybrid-functional, and DMFT treatment, we find the flat band to split into narrow Hubbard bands.

Phonon-renormalization scheme

Despite the success of density-functional perturbation theory (DFPT), the ab-initio calculation of lattice vibrations remains computationally expensive. Hence, whenever we want to

investigate phonon-related properties for a wide range of parameters, we benefit from first downfolding the many-body problem to a low-energy model, which allows us not only to reproduce the fully ab-initio results but also to go beyond and analyze the effect of the variation of selected parameters. In order to derive our models we use *constrained* density-functional perturbation theory (cDFPT) [9] and apply the open-source programs QUANTUM ESPRESSO, Wannier90 and EPW.

Outlook

During our studies concerning Coulomb engineering in semiconductors we modeled the substrate with *static* dielectric functions. For some substrates this can be a good approximation. However, in general dielectric functions are frequency dependent. For future research we have to find more material realistic models for the studied substrates. Additionally, we want to investigate not only the class of semiconducting TMDCs for its applicability but also other 2D materials as for example 2D hexagonal boron nitride. Concerning the employment of defects in the context of Coulomb engineering the developed multi-scale approach seems feasible, so that in future research more complex defects or defect clusters like e.g. adatom chains could be considered.

Publications

1. P. Klement, C. Steinke, S. Chatterjee, T. Wehling, M. Eickhoff, *2D Mater.***5**, 045025 (2018)
2. E. Kamil, J. Berges, G. Schönhoff, M. Rösner, M. Schüler, G. Sangiovanni, T. Wehling, *J. Phys. Condens. Matter***30**, 325601 (2018)

Presentations

1. C. Steinke, M. Rösner, D. Ryndyk, T. Wehling, Material Realistic Description of Coulomb-engineered Two-dimensional Materials, APS March Meeting, Los Angeles, March 8, 2018 and DPG Frühjahrstagung, Berlin, March 16, 2018
2. G. Schönhoff, M. Rösner, E. Kamil, J. Berges, T. Wehling, Realistic Description of Competing Interactions in Metallic TMDCs, APS March Meeting, Los Angeles, March 8, 2018 and DPG Frühjahrstagung, Berlin, March 15, 2018
3. E. Kamil, J. Berges, G. Schönhoff, M. Schüler, T. Wehling, Theory of Mott physics in 1T-NbSe2: An LDA+DMFT study, APS March Meeting, Los Angeles, March 8, 2018 and DPG Frühjahrstagung, Berlin, March 15, 2018

Posters

1. C. Steinke, M. Rösner, D. Ryndyk, T. Wehling, Material Realistic Description of Coulomb-engineered Two-dimensional Materials, Flatlands beyond Graphene, Leipzig, September 6, 2018
2. C. Steinke, N. Witt, M. Rösner, T. Wehling, Material Realistic Description of Coulomb Engineering and Defect Potentials in Two-dimensional Materials, CECAM: Correlated electron physics beyond the Hubbard model, Bremen, February 7, 2019

References

[1] M. Rösner et al., Nano Lett. 16, 2322 (2016)
[2] A. Raja et al., Nat. Comm. 8, 15251 (2017)
[3] Z. Lin et al., 2D Mat. 3, 022002 (2016)
[4] G. Kresse and J. Hafner, J. Phys. Condens. Matter 6, 8245 (1994)
[5] M. Rohlfing, Phys. Rev. B 82, 205127 (2010)
[6] M. Rösner et al. Phys. Rev. B. 92, 085102 (2015)
[7] L. V. Keldysh, JETP Lett. 29, 658 (19798)
[8] Y. Nakata et al., NPG Asia Materials 8, e321 (2016)
[9] Y. Nomura et al., Phys. Rev. B 92, 245108 (2015)

6.27 hbp00046: Modelling strongly correlated electrons in presence of nonlocal interactions

HLRN Project ID:	hbp00046
Run time:	IV/2017 – III/2019
Project Leader:	Prof. Dr. Tim O. Wehling
Project Scientists:	Edin Kapetanović, Malte Schüler
Affiliation:	Institut für Theoretische Physik, Universität Bremen

Overview

The competition of local and non-local Coulomb interactions plays an important role in the electronic structure of strongly correlated materials: Non-local interactions can effectively screen local interactions and weaken Mott Hubbard type electron correlations. They can furthermore push the electronic system into symmetry broken phases with e.g. charge order. While local and non-local Coulomb interactions naturally occur in any real material, low-energy models which describe correlated electron systems (e.g. the Hubbard model) quite often neglect non-local interactions completely.

In this project, we currently focus specifically on a Hubbard model extended by the nonlocal exchange interaction which tends to push the system towards a ferromagnetic state. While said interactions are often neglected due to their typically small magnitude, we find that exchange interactions which are much weaker than the hopping are sufficient to change the properties of the system. This makes the widely used Hubbard approximation quite questionable.

In order to study the influence of nonlocal exchange interactions, we introduce an effective Hubbard model with a renormalized on-site interaction and an effective magnetic field which accounts for possible ferromagnetic order.

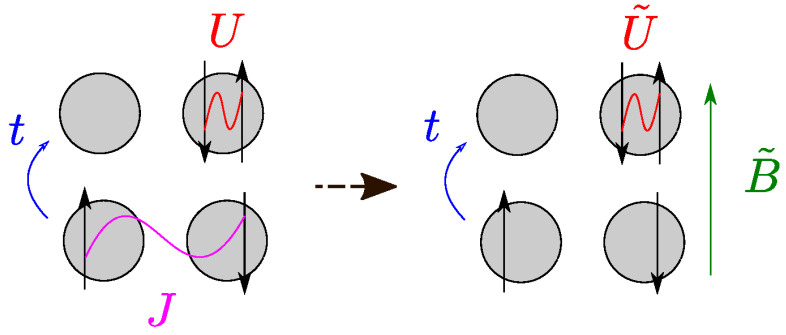

Figure 1: Original model (left) and the effective model (right) which is used as an approximation.

The parameters of the effective model (i.e. the local interaction the the effective, magnetic field) are chosen such that we minimize a free energy functional through the density operator. This involves solving the effective model, which we do with the Determinantal Quantum Monte Carlo (DQMC) method.

Results

We have performed DQMC calculations for a Hubbard model with an external magnetic field at half filling where the sign problem is absent. The geometries are chosen to be square lattices (with periodic boundary conditions) since Hubbard models on such lattices have been extensively studied, especially in the context of superconductivity. From different lattice sizes (i.e. 4x4, 6x6, 8x8, 10x10, 12x12), we extrapolated the relevant data for the $N \to \infty$ - case. When performing the calculation for each datapoint in the *U* - *B*-plane with one CPU, the parallelization becomes trivial. The temperature in the simulations was set to $\beta t = 10$, which corresponds to a regime where correlation effects are expected to be visible.

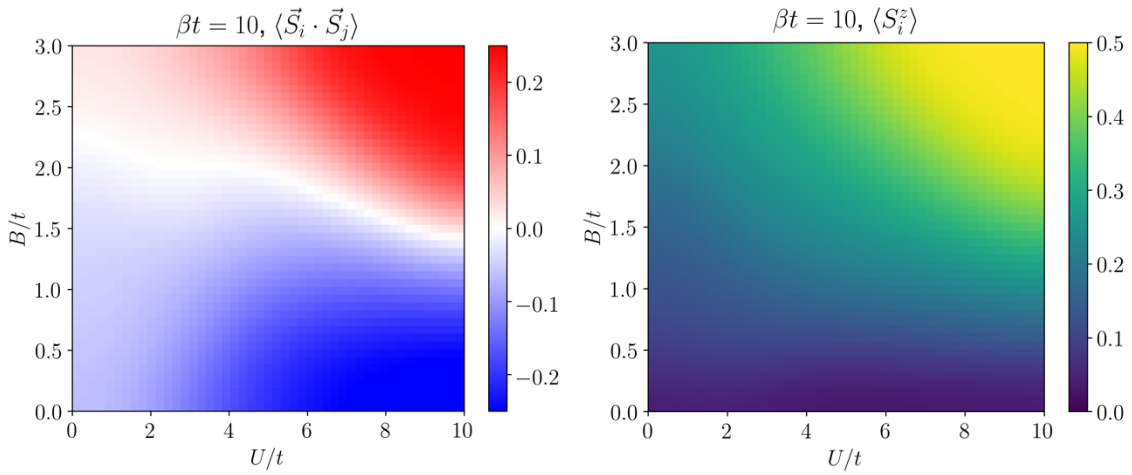

Figure 2: (left): Total Spin-Spin-Correlation function between next neighbors in the effective model, depending on *U* and *B*. (right): Magnetization per lattice site. A gaussian filter has been used to minimize the Monte Carlo noise.

We first discuss the properties of the effective model since it has not been studied well in itself. Figure 2 shows the average Spin-Spin-Correlation between electrons on neighboring lattice sites and the net magnetization. The sign of the Spin-Spin-Correlation hints at possible antiferromagetic and ferromagnetic ordering in the system. At half filling, depending on U and B the effective model can describe a metallic phase, a Mott insulating phase with strong antiferromagnetic correlations and a ferromagnetic phase.

Figure 3 shows the Spin-Spin correlation and the magnetization of the original model, which have been obtained by performing the mapping. In the strong *U*-limit, we see strong antiferromagnetic correlations for $J = 0$. Introducing a sufficiently strong ferromagnetic exchange, i.e. $J \sim 4t^2/U$ (which is expected from analytical solutions), the systems undergoes a continuous transition into the ferromagnetic state. However, for intermediate U/t the system displays jumps in the observables (i.e. first order transitions). The most dominant one is the transition to the fully ferromagnetic state, which can be seen in Figure 3. Taking an explicit look at the renormalized on-site interaction $\widetilde{U}$ and the magnetic field $\tilde{B}$ reveals that, for intermediate original U, a small nonlocal exchange $J \sim t$ between next neighbors is sufficient to effectively double the local interaction, which has a strong impact on all relevant quantities of the system. Thus, we conclude that the nonlocal exchange interaction, which is often dropped due to its small magnitude, should not be neglected.

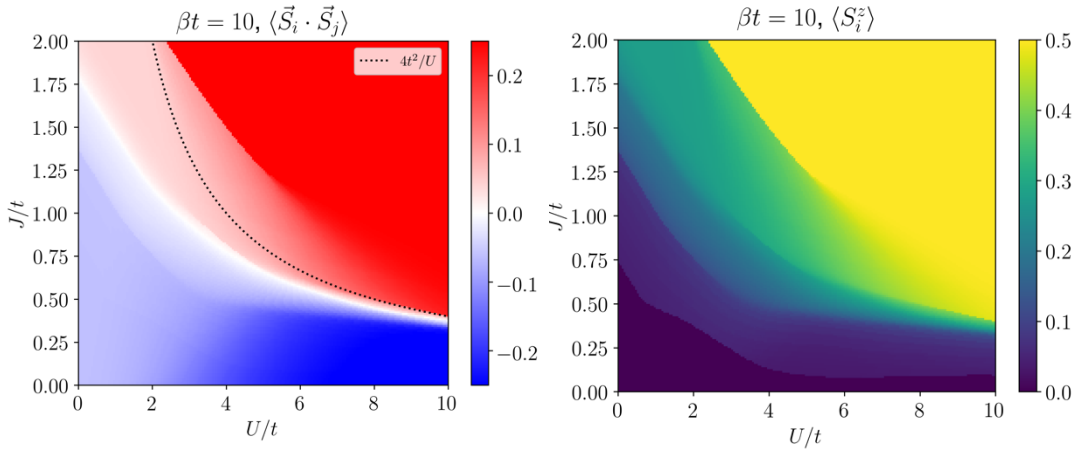

Figure 3: (left): Total Spin-Spin-Correlation function between next neighbors of the original model, depending on *U* and *J*. (right): Magnetization per lattice site.

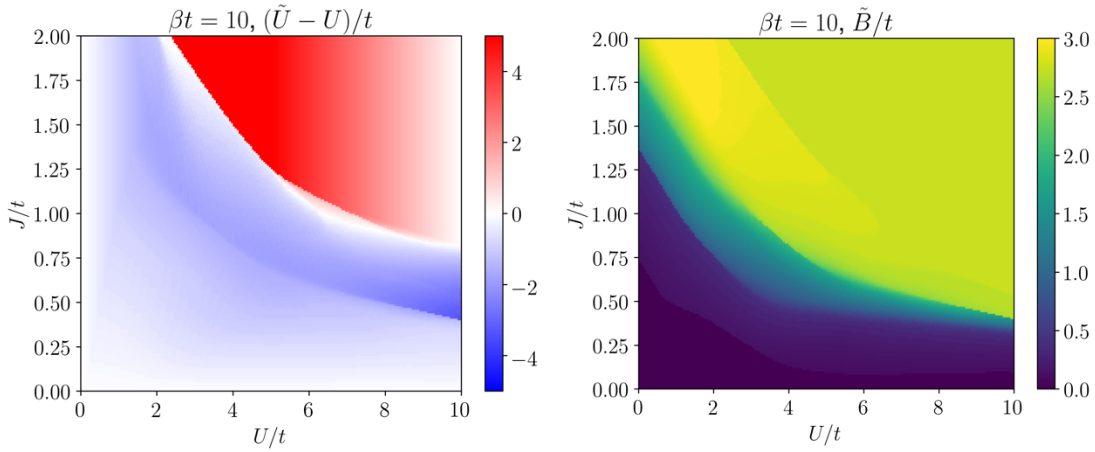

Figure 4: Effective Parameters $\tilde{U}$ and $\tilde{B}$, depending on the original on-site interaction *U* and nonlocal exchange *J*.

Outlook

While we intend to summarize all the mentioned results in a paper, the same calculations can in principle be repeated for different temperatures. Aside from the mapping, the raw Monte Carlo data itself can be used to determine exactly how a Hubbard model responds to magnetic fields and how well linear response theory is applicable.

Presentations & Posters

Poster: CECAM-Workshop "Correlated Electron Physics beyond the Hubbard Model", Feb 4th-8th 2019, Bremen